Title
Rejuvenation of Ni-base Superalloys GTD444 and René N5

Author
Rettberg, Luke

Publication Date
2016

UNIVERSITY of CALIFORNIA
Santa Barbara

Rejuvenation of Ni-base Superalloys GTD444 and René N5

A Dissertation submitted in partial satisfaction of the
requirements for the degree

Doctor of Philosophy
in
Materials

by

Luke Henry Rettberg

Committee in charge:

Professor Tresa M. Pollock, Chair
Professor Ted D. Bennett
Professor Carlos G. Levi
Professor G. Robert Odette

June 2016

The dissertation of Luke Henry Rettberg is approved.

Professor Ted D. Bennett

Professor Carlos G. Levi

Professor G. Robert Odette

Professor Tresa M. Pollock, Committee Chair

May 2016

Rejuvenation of Ni-base Superalloys GTD444 and René N5

by

Luke Henry Rettberg

Acknowledgements

As I approach the end of my academic studies, there are a number of people that have influenced and helped me along the way that I would like to thank. My interest in high temperature materials began during my senior design project at Purdue University, under the guidance of Prof. Kevin Trumble.

For my graduate studies at the University of Michigan and the University of California, Santa Barbara, I was very fortunate to be advised by Prof. J. Wayne Jones and Prof. Tresa Pollock, respectively. I'm also grateful for the opportunity to attend several conferences around the world to present my own work and to participate in professional societies. And last, but most certainly not least, I'd like to thank my girlfriend Kaylan, Dad, Mom, and brother, Seth, for their love and support over the years.

Funding for this work was primarily provided by GE Power along with the GTD444(CG) and René N5(SX) material. Additional support by the U.S. Air Force Research Laboratory (AFRL) through Research Initiatives for Materials State Sensing (RIMSS) Contract FA8650-15-C-5208, through Universal Technology Corporation is also acknowledged. Support of the microscopy equipment used in the study is provided by the MRSEC program of the National Science Foundation under award No. DMR 1121053.

Curriculum Vitæ

Luke Henry Rettberg

Education

June 2016	Ph.D. in Materials, University of California, Santa Barbara, CA, USA
April 2011	M.S. in Materials Science and Engineering, University of Michigan, Ann Arbor, MI, USA
May 2009	B.S. in Materials Engineering, Purdue University, West Lafayette, IN, USA

Publications

5. L.H. Rettberg, B.R. Goodlet, and T.M. Pollock, "Detecting Recrystallization in a Single Crystal Ni-Base Alloy using Resonant Ultrasound Spectroscopy," NDT&E *Int.*, (2016). [**doi**]

4. L.H. Rettberg, B. Laux, M.Y. He, D. Hovis, A.H. Heuer, and T.M. Pollock, "Growth Stresses in Thermally Grown Oxides on Nickel-Base Alloy Single Crystals," *Metall. Mater. Trans. A*, **47**, (2016), 1132-1142. [**doi**]

3. L.H. Rettberg and T. M. Pollock, “Localized Recrystallization During Creep in Nickel-based Superalloys GTD444 and René N5,” *Acta. Mater.*, **73**, (2014), 287-297. [**doi**]

2. L.H. Rettberg, M. Tsunekane, and T.M. Pollock, “Rejuvenation of Nickel-Based Superalloys GTD444(DS) and René N5(SX),” in Superalloys 2012 (eds E.S. Huron, R.C. Reed, M.C. Hardy, M.J. Mills, R.E. Montero, P.D. Portella and J. Telesman), (2012), 341-349. [**doi**]

1. L.H. Rettberg, J.B. Jordan, M.F. Horstemeyer, and J.W. Jones, “Low-Cycle Fatigue Behavior of Die-Cast Mg Alloys AZ91 and AM60,” *Metall. Mater. Trans. A*, **43**, (2012), 2260-2274. [**doi**]

Abstract

Rejuvenation of Ni-base Superalloys GTD444 and René N5

by

Luke Henry Rettberg

During service, superalloy turbine components degrade over time by creep and fatigue deformation mechanisms due to a complex combination of stresses at high temperatures. Service degradation is commonly addressed by replacing the component with a new one. The high cost of the original Ni-base superalloy components and, consequently, replacement components has encouraged the development of rejuvenation (restoration) procedures to extend useful service life. Repair procedures used in literature consist of hot isostatic pressing (HIP) and/or solution + aging rejuvenation heat treatments near or above the γ' solvus temperature. In the limited studies that have performed fatigue testing, rejuvenation has never been successful in recovering fatigue properties in low-cycle, high-cycle, or dwell-fatigue.

In order to elucidate the processes that prevent successful rejuvenation, repeated rejuvenation cycles have been performed. A rejuvenation cycle includes a rejuvenation heat treatment and/or small scale material removal, followed by creep or fatigue testing. Multiple rejuvenation testing is defined in this context as the application of repeated rejuvenation

cycles until specimen failure.

As a result of multiple rejuvenation testing, the total creep rupture life of René N5(SX) tested at 982 °C and 206 MPa was extended by a factor of 2.8 over the baseline rupture life. To produce this increase in rupture life, creep strain thresholds of both 2% and 3% were used along with solutioning at 28 °C below the γ' solvus temperature for 2 h and aging at 1079 °C for 4 h. These rejuvenation conditions resulted in the maximum observed increase in total creep rupture life. Rejuvenation of compressive hold-time fatigue damage was also successful with the use of small scale material removal. While rejuvenation of René N5(SX) was considered successful, full recovery of the creep performance was not attainable even with a solution heat treatment at the γ' solvus. Similar results are expected for GTD444(CG) although rejuvenation heat treatments were only performed below the γ' solvus temperature.

Transverse grain boundaries limited life during multiple rejuvenation creep testing of both GTD444(CG) and René N5(SX). Due to the tortuosity of the grain boundaries in GTD444(CG), some boundaries are initially oriented transverse to the growth direction. The enhanced plasticity near these grain boundaries may be the primary reason why the initially single crystal René N5(SX) specimens were more amenable to rejuvenation than GTD444(CG). For both alloys, recrystallization during the rejuvenation heat treatment was responsible for early failure during the subsequent creep test.

Using rejuvenation in a production environment on these alloys represents a significant challenge. There will be a difference in microstructure between lab and industrial-scale components and a difference between service and mechanical testing conditions, requiring detailed characterization and identification of the life-limiting form of damage. Ultimately, the use of rejuvenation on industrial-scale components will depend on a number of factors for each specific case.

Contents

List of Figures

List of Tables

Chapter 1

Introduction: The Development and Repair of Ni-base Superalloys

1.1 Application: The Gas Turbine Engine

Ni-base superalloys are used in gas turbine engines that consist of three major sections: a compressor, combustion chamber, and turbine. Being a heat engine, gas turbines convert thermal energy to mechanical energy, which is then used to perform useful work. The first major application of a gas turbine engine with an axial flow compressor was to power aircraft near the end of World War II and, currently, gas turbine engines with the same basic framework are being used to power not only aircraft, but also tanks, ships, trains, and for the generation of electricity [1]. Various gas turbine engine designs are shown in Figure 1.1.

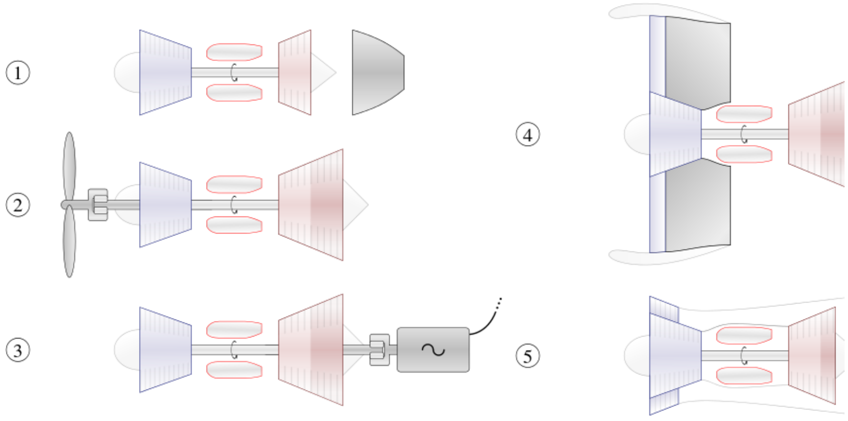

Figure 1.1: Several common gas turbine engine configurations used for jet propulsion and power generation, specifically (1) turbojet, (2) turboprop, (3) turboshaft, (4) high-bypass turbofan, and (5) low-bypass turbofan. Adapted from “Gas turbine applications (numbered)” by O. Cleynen.

The thermal efficiency, η_{th}, of gas turbine engines can be described to a first approximation by the Carnot cycle [2, 3]. The most practical way to increase the thermal efficiency of the engine is to increase the useful work, which, assuming the exhaust gas is a perfect gas, can be accomplished by increasing the turbine entry temperature (TET). For example, a 30 °C increase in the TET for a high-bypass turbofan used for jet propulsion, or a 10 °C increase for a combined-cycle turboshaft system used for electrical generation, results in a 1% increase in efficiency [4]. An increase in efficiency of only 1% reduces fuels costs over a 15 year period by $30 billion and $60 billion for global aviation and gas-fired power generation sectors, respectively [5]. However, the TET is ultimately limited by the high-temperature capability of the materials selected for the various components in the turbine section of the engine.

Various material systems are used in a gas turbine engine, with the most advanced being located along the hot gas path. Figure 1.2 shows a schematic of a Rolls Royce Trent 800 engine indicating the type of materials used in different locations along the gas path.

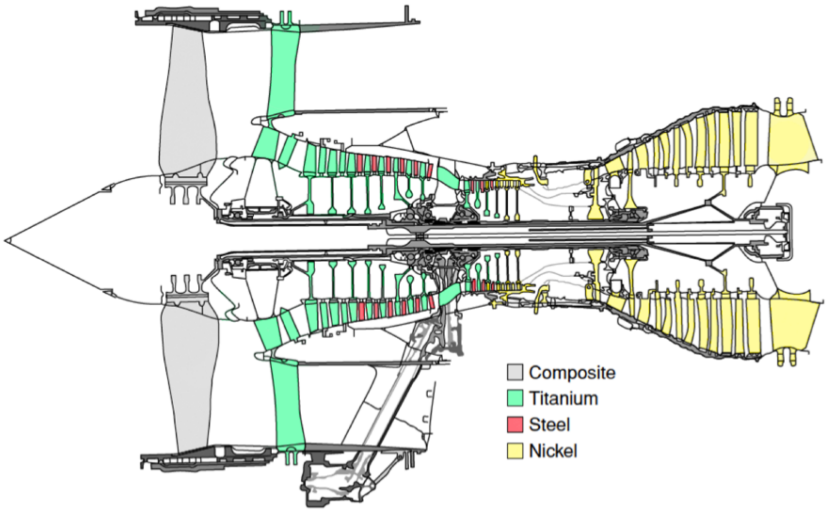

Figure 1.2: Schematic cross-section of a Rolls-Royce Trent 800 engine with the typical materials used along the gas path in a gas turbine engine indicated with color shading. Adapted from Rolls-Royce (©Rolls-Royce). Ni-base superalloy material is indicated in yellow.

Selection of materials for gas turbine engine components requires consideration of a large suite of properties, namely: high temperature strength, oxidation/corrosion resistance, ductility, fatigue resistance, and toughness. Depending on the function of the engine, for example power generation versus aircraft propulsion, additional properties may be more strongly weighted in the material selection process; density, for example, is much more important for aircraft, compared to power generation. Ni-base superalloys, employed in the blades and vanes of the turbine after the combustion section, are exposed to the highest temperatures and mechanical loads of any rotating component in the engine.

1.2 Ni-base Superalloys: An Overview

The current state of the art Ni-base superalloys are a result of over 60 years of engineering and scientific research. Critical advancements have been made in processing and microstructural control to produce the alloys used today in gas turbine engines. The development of investment casting and directional solidification will be discussed in this section along with the microstructural constituents of Ni-base superalloys.

1.2.1 Processing

Turbine blades extract energy from the hot combustion gases, providing useful work to drive the compressor, high-bypass fan, and/or electrical generator. Considered a critical component in the successful operation of a gas turbine engine, turbine blades are conservatively designed with significant factors of safety. Superalloy turbine blades are manufactured via investment casting processes. Starting with a wax mold of the desired turbine blade geometry, a ceramic slurry is applied around the wax and allowed to harden [6]. The wax is then removed and the ceramic slurry sintered during a subsequent heat treatment process, creating a hollow cavity where molten metal can be poured.

After pouring, cooling the molten metal in an uncontrolled manner creates polycrystalline (PC) material; to improve creep properties the cooling rate is often decreased, increasing the grain size. A critical advancement in the processing of Ni-base superalloys was the development of high thermal gradient directional solidification processes that created columnar grained (CG) turbine blades. Additionally, with the use of a grain selector/seed crystal, single crystal (SX) turbine blades were produced in the early 1970s by VerSnyder and co-workers at Pratt & Whitney. A schematic of the casting process and examples of turbine blades with the various grain structures are shown in Figure 1.3.

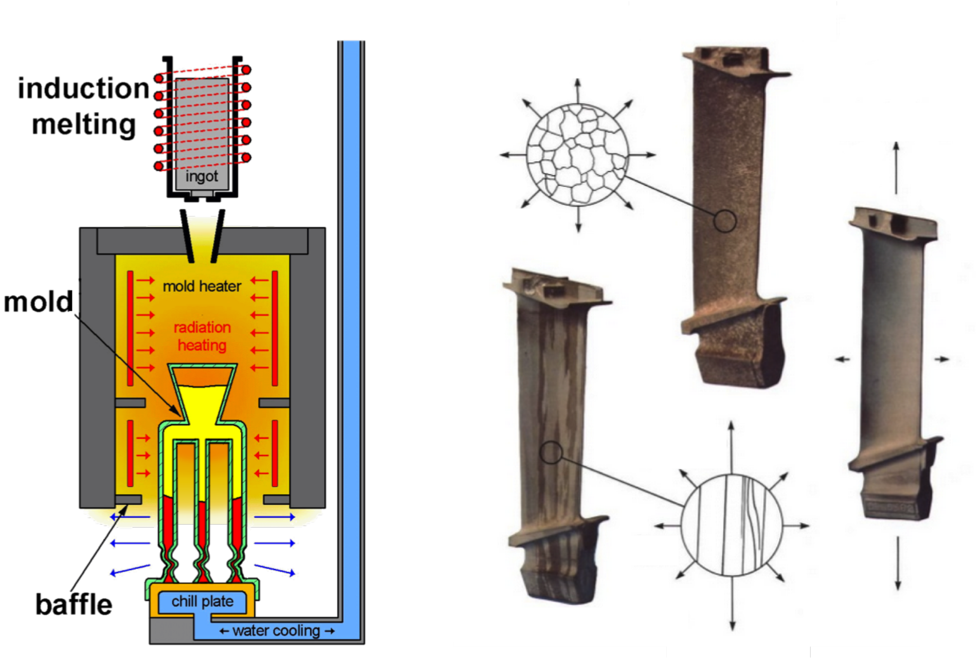

(a)

(b)

Figure 1.3: a) Schematic illustrating the Bridgman casting process used for directional solidification of Ni-base superalloys and b) images of a polycrystalline, columnar grained, and single crystal turbine blade. Adapted from original work by Elliott [7] and Rolls-Royce (©Rolls-Royce) [8].

By removing all high angle grain boundaries, single crystal superalloys have the most favorable creep properties and, without the requirement for grain boundary strengtheners, microsegregation and eutectic content can be significantly reduced during heat treatments without causing incipient melting, thereby improving fatigue life [2, 9].

1.2.2 Microstructure and Alloy Chemistry

Superalloy compositions are based on the Ni-Al binary with up to 40 wt% of five to ten other elements. Examining the Ni-Al phase diagram, as the Al content increases in the face-centered cubic, nickel-rich γ phase, a two phase γ + γ' field is reached, as shown in Figure 1.4. The γ' phase has a nominal composition of Ni_3Al, is an ordered intermetallic with the $L1_2$ crystal structure, and is often coherent with the γ matrix phase. Minor alloying elements tend to form carbides or borides with cubic crystal structures that precipitate in the liquid melt during solidification and, consequently, are typically located at high angle boundaries and interdendritic regions of the microstructure [10]. Carbon forms thermodynamically stable compounds with a variety of metallic atoms (M) present in Ni-base superalloys, such as Ta, Ti, Nb, W, and Mo, to form primary MC carbides with blocky, script, and globular morphologies (Figure 1.5).

Superalloys derive their strength primarily from the γ' precipitate phase; this is especially true at high fractions of their melting point [14]. Precipitation of the γ' phase occurs heterogeneously from the supersaturated solid solution of γ as it is cooled below the γ' solvus temperature by the nucleation and growth mechanisms. The kinetics of the precipitation process are highly influenced by the cooling rate through the γ' solvus temperature.

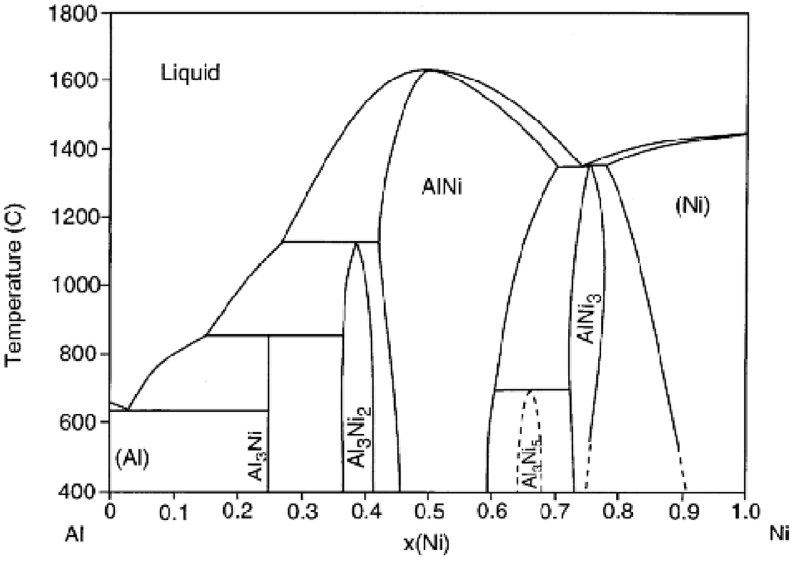

Figure 1.4: Binary phase diagram of the Al-Ni system, from Kattner, *et al.* and Okamoto, *et al.*[11, 12].

The classification of a new generation is due to major chemistry modifications, including the increase in refractory metal content among SX Ni-base superalloys, and refinement of grain boundary strengtheners Hf, C, and B due to the advent of directional solidification. Table 1.1 provides compositions for PC, CG, and the first three generations of SX Ni-base superalloys with the major composition differences being the addition of Re, a potent solid solution strengthener, along with increased amounts of other refractory elements, and γ' formers Ta and Al [2, 10]. To date there are a total of six generations, however, due to the high cost of Re and other refractory elements, only first and second generation superalloys have been used in service [18].

The morphology of the γ' precipitates in Ni-base superalloys has been observed to vary significantly depending on the elastic strain energy caused by the lattice mismatch between

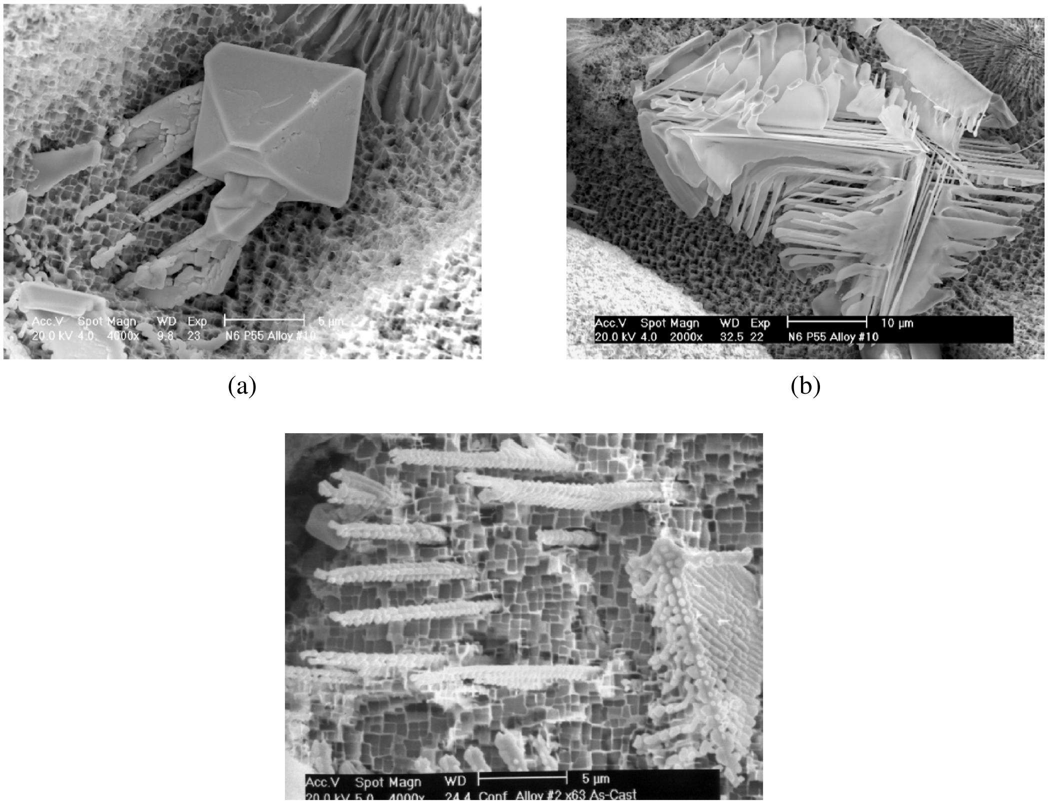

(a)

(b)

(c)

Figure 1.5: SEM micrographs from an overetched Ni-base superalloy showing the three primary morphologies of MC carbides; a) blocky, b) script, c) and nodular. From Tin, *et al.* [13].

the γ and γ' phases [14]. The misfit between the lattice parameters of the two phases, δ, is defined in Equation 1.1 and for Ni-base superalloys is typically near -0.3% [10, 20–22].

$$\delta = \frac{a_{\gamma'} - a_{\gamma}}{\frac{1}{2}\left(a_{\gamma'} + a_{\gamma}\right)} \tag{1.1}$$

Both morphology and volume fraction are primarily functions of alloy chemistry, while precipitate size is controlled by heat treatment. Inherent to the dendritic solidification process, segregation of alloying elements occurs to either the interdendritic or dendrite core regions in the as-cast microstructure. Subsequent heat treatments are used to optimize the

Table 1.1: Composition, in weight percent, of various turbine blade alloys with the balance being Ni [2, 10, 15–17].

Alloys	Cr	Co	Mo	W	Ta	Re	Nb	Al	Ti	Hf	C	B
Conventionally Cast Alloys												
Mar-M-246	8.3	10.0	0.7	10.0	3.0	-	-	5.5	1.0	1.50	0.14	0.02
René 80	14.0	9.5	4.0	4.0	-	-	-	3.0	5.0	-	0.17	0.02
IN-713LC	12.0	-	4.5	-	-	-	2.0	5.9	0.6	-	0.05	0.01
Columnar Grained Alloys												
IN792	12.6	9.0	1.9	4.3	4.3	-	-	3.4	4.0	1.00	0.09	0.02
GTD111	14.0	9.5	1.5	3.8	2.8	-	-	3.0	4.9	-	0.10	0.01
GTD444	9.7	8	1.5	6	4.7	-	0.5	4.2	3.5	0.15	0.08	0.005
First-Generation Single Crystal Alloys												
PWA1480	10.0	5.0	-	4.0	12.0	-	-	5.0	1.5	-	-	-
René N4	9.8	7.5	1.5	6.0	4.8	-	0.5	4.2	3.5	0.15	0.05	0.004
CMSX-3	8.0	5.0	0.6	8.0	6.0	-	-	5.6	1.0	0.10	-	-
Second-Generation Single Crystal Alloys												
PWA 1484	5.0	10.0	2.0	6.0	9.0	3.0	-	5.6	-	0.10	-	-
René N5	7.0	7.5	1.5	5.0	6.5	3.0	-	6.2	-	0.15	0.05	0.004
CMSX-4	6.5	9.0	0.6	6.0	6.5	3.0	-	5.6	1.0	0.10	-	-
Third-Generation Single Crystal Alloys												
René N6	4.2	12.5	1.4	6.0	7.2	5.4	-	5.8	-	0.15	0.05	0.004
CMSX-10	2.0	3.0	0.4	5.0	8.0	6.0	0.1	5.7	0.2	0.3	-	-

γ' precipitate size and to homogenize the chemical segregation. Example micrographs of two superalloys with similar compositions in the as-cast and heat treated condition are shown in Figure 1.6.

1.3 Mechanical Properties and Deformation Mechanisms

The motivation for advances in processing and microstructure come from the necessity to improve mechanical properties in order to increase the TET and improve efficiency. Of particular importance is the resistance to creep, or time-dependent elevated temperature

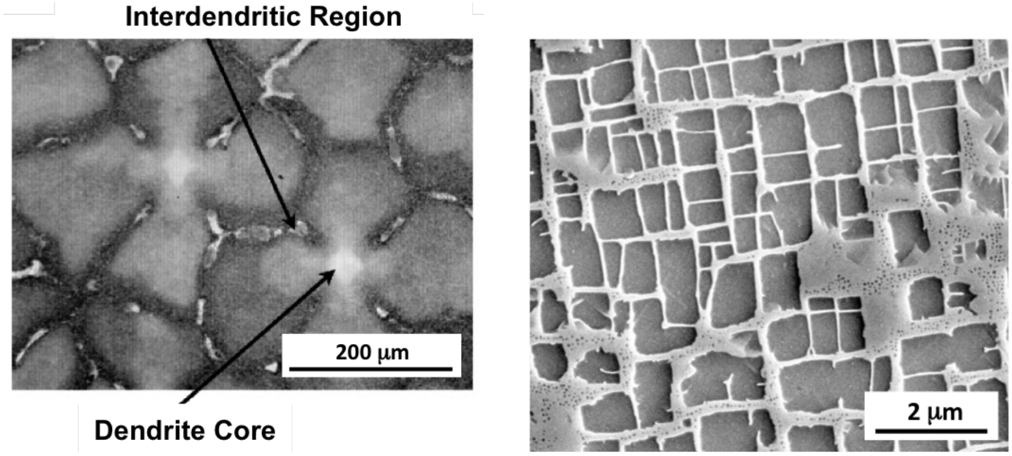

(a) (b)

Figure 1.6: Micrographs collected using a scanning electron microscope of a) an experimental single crystal alloy in the as-cast condition and b) a commonly used single crystal General Electric (GE) alloy René N5 after homogenization, solution, and aging heat treatments. From Pollock, *et al.* [19].

deformation, of Ni-base superalloys, due to the tight tolerance between turbine blades and the surrounding engine housing. Microstructural evolution and damage mechanisms during creep testing at high temperature and low stresses will be discussed. Besides creep, fatigue damage mechanisms during low-cycle, high-cycle, and thermomechanical fatigue loading in Ni-base superalloys will also be summarized. The discussion will be limited to high temperature deformation mechanisms, specifically at temperatures near 982 °C.

1.3.1 Creep

In pure or single phase simple materials, creep is well described by three distinct regimes: primary, secondary, and tertiary. However, complex engineering alloys, such as Ni-base superalloys, typically do not exhibit an extended secondary or steady state regime with a balance between hardening and recovery processes (constant creep rate); instead, the creep rate continuously increases from a minimum rate established after a small primary creep strain [23]. Thus, a majority of creep life is spent in the tertiary creep regime, as seen in Figure 1.7. The mechanisms that result in the continuous acceleration of the creep rate in this class of materials are not well understood.

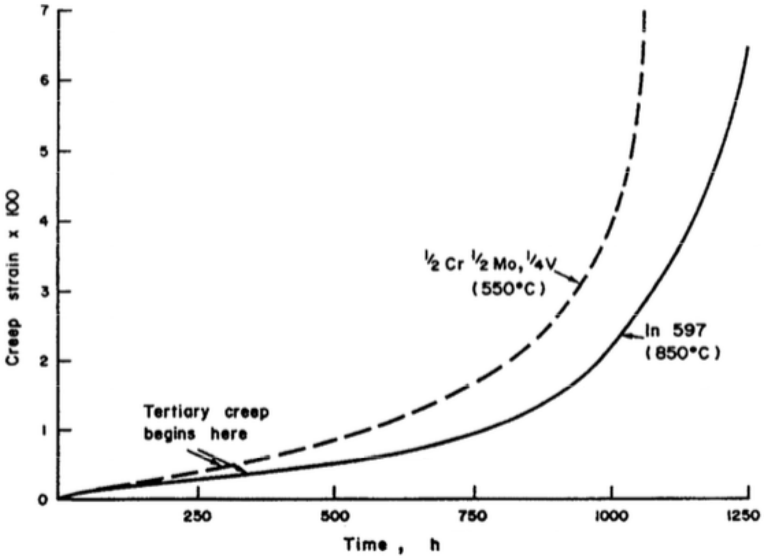

Figure 1.7: Experimental creep curves from two advanced engineering alloys: a low alloy ferritic steel and the Ni-base superalloy IN 597, illustrating that a majority of creep life is spent in the tertiary creep regime. From Dyson, *et al.* [23].

Once the load is applied at temperature, during high temperature (982 °C) and low stress (172-206 MPa) creep, there is an initial incubation period in which dislocations percolate through the γ matrix phase [24–26]. This process is impeded by the presence of the γ' precipitates, forcing the dislocations to cross-slip and bow through the narrow matrix channels. Dislocation glide occurs preferentially along the horizontal matrix channels perpendicular to the applied tensile load due to an estimated 2.4 times higher resolved shear stress on $\langle 110 \rangle \{111\}$ slip systems in the horizontal channels [24, 27, 28]. This is a result of the superposition of the applied load and the misfit stresses between the γ matrix and γ' precipitates, as shown in Figure 1.9. Once dislocations have permeated the material to a point at which macroscopic strains can be measured, primary creep begins. During primary creep, dislocations continue to move through the γ channels and accumulate on γ/γ' interfaces, gradually relaxing the misfit and consequently the misfit stresses, leading to a decrease in the strain rate over time. The evolution of the dislocation structure in the first generation Ni-base superalloy CMSX-3 during primary creep at 850 °C and 552 MPa is shown in Figure 1.8. In this temperature and stress regime, the γ' precipitates are not

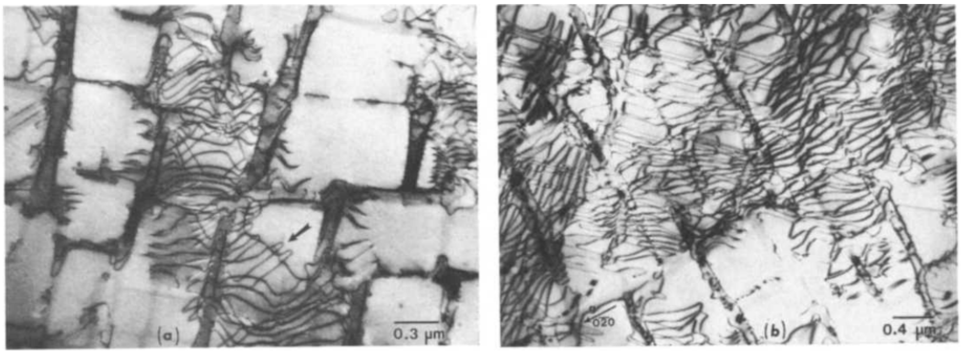

Figure 1.8: Transmission electron microscopy (TEM) micrographs of CMSX-3 crept at 850 °C and 552 MPa. Early in primary creep (left), dislocations begin to fill the horizontal γ matrix channels; toward the end of primary creep (right), dislocations have filled most horizontal and vertical matrix channels through a process of bowing. Taken from Pollock, *et al.* [24].

sheared until after a minimum creep rate has been reached.

Directional coarsening (rafting) of the precipitates also occurs during creep at high temperatures (>900 °C). Rafting is influenced by the misfit stresses, a result of the lattice mismatch between the γ matrix and γ/γ' precipitates. Rafting occurs by the coalescence of the γ' precipitates along the less stressed matrix channels, which, for negative misfit alloys experiencing a tensile stress, are the vertical channels; the rafting process is illustrated in Figure 1.10 [29–32]. At the end of the primary creep regime, a minimum creep rate is reached, and after several hours the strain rate begins to increase with time, signifying the beginning of the tertiary creep regime. It has been observed that the strain rate becomes roughly proportional to the accumulated strain in the tertiary creep regime. This behavior has been rationalized by assuming that the mobile dislocation density increases as a function of the macroscopic strain and a constant describing the dislocation multiplication rate [23, 33, 34]. The increase in mobile dislocation density results in a larger number of jogged segments, increasing the climb velocity and consequently the creep rate [35].

Later in the tertiary creep regime, local stresses are high enough for dislocations to shear the γ' precipitates [2, 24]. Shearing has also been observed immediately after the primary creep regime in some cases, and is likely a contributing factor to the acceleration of the creep rate in the tertiary regime [36]. Unfortunately since the shearing process occurs by the glide of anti-phase-boundary-coupled a/2$\langle 110 \rangle$ dislocation pairs that enter on one side of the precipitate and exit on the opposite side there is no physical trace of the number of shearing events.

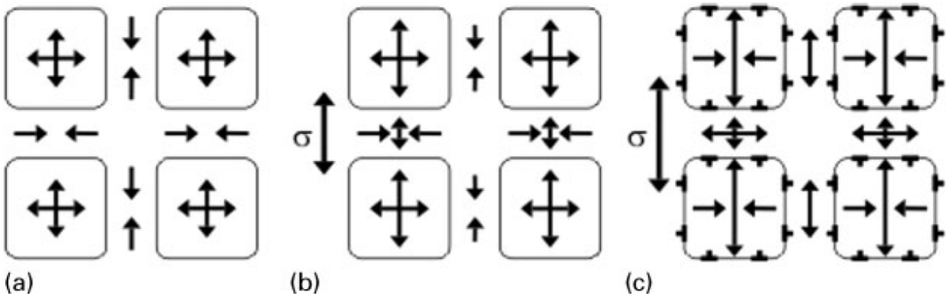

Figure 1.9: Schematic showing the misfit stresses in both the γ' precipitates and γ matrix channels for a negative misfit superalloy a) in the unloaded state, b) with a small elastic tensile load, and c) with a large load causing plastic deformation. Taken from Mughrabi, *et al.* [22].

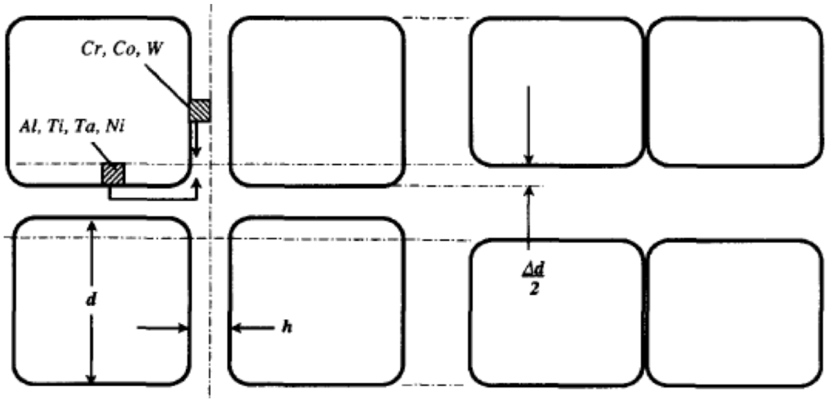

Figure 1.10: Illustration of rafting (directional coarsening), which is a diffusional process requiring plastic deformation, where γ' forming elements diffuse from the horizontal γ matrix channels to the vertical matrix channels. From Pollock, *et al.* [37].

In the tertiary creep regime, damage develops in the form of cavities nucleating and growing from solidification porosity and carbides [38]. The carbides are non-deformable particles, creating local stress concentrations in the surrounding material that can be relieved by local plastic deformation, decohesion of the matrix/particle interface, or by particle cracking [39]. In polycrystalline alloys it is well known that cavities preferentially grow on grain boundaries transverse to the loading axis, limiting creep ductility. However, in CG and SX, very little damage is observed early in the tertiary creep regime due to the elimination of transverse boundaries (Figure 1.11) [23, 40]. As creep progresses, nearby cavities coalesce and rupture occurs when cavities reach a critical fraction of the load-bearing cross-sectional area [41, 42]. The large strains associated with tertiary creep are not expected globally in turbine components while in service, but do occur locally at defects due to stress concentrations.

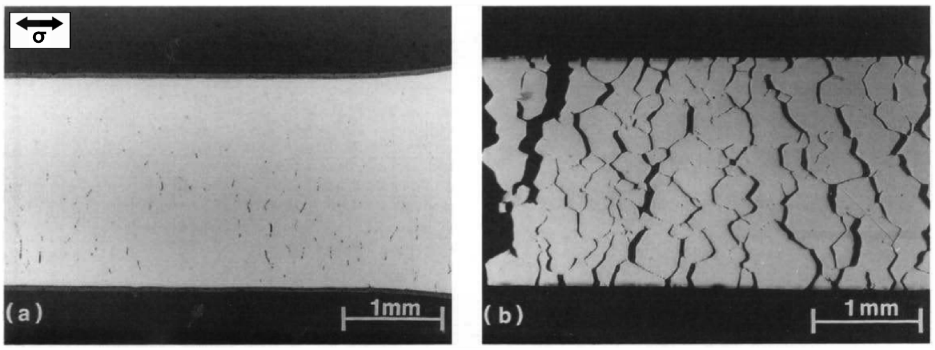

Figure 1.11: Optical micrograph showing cracks and creep cavities after a creep test well into the tertiary creep regime for a) single crystal and b) polycrystalline superalloys [43].

1.3.2 Fatigue

Fatigue is another potentially life limiting deformation mechanism. Low-cycle fatigue, high-cycle fatigue, and thermomechanical fatigue (TMF) of turbine blades occurs during service due to changing centrifugal loads during start-up and shut down, turbulent air flow causing natural resonance, and thermal cycling, respectively. The crystallographic orientation of single crystal Ni-base superalloys plays an important role in the fatigue performance of Ni-base superalloys [44, 45]. Single crystals tested along the [001] direction have the best fatigue performance while [111] oriented crystals have the worst, see Figure 1.12. This is a result of elastic anisotropy, with the ⟨100⟩ directions having the lowest elastic modulus, minimizing accumulated inelastic strain per cycle in a strain controlled fatigue test.

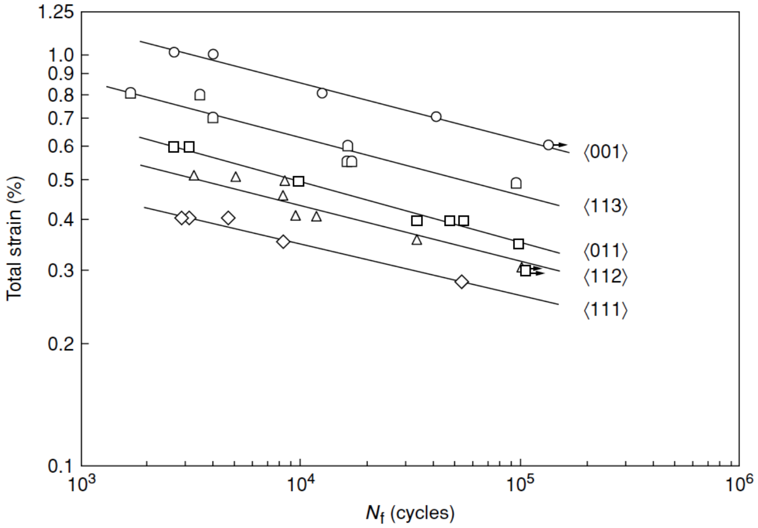

Figure 1.12: Strain versus the number of cycles to failure for single crystal Ni-base superalloy fatigue specimens oriented along different crystallographic directions, illustrating the influence of orientation on fatigue performance. Tests were performed at 982 °C. Modified by Reed from original work by Dalel, *et al.* [2, 45].

During low-cycle fatigue testing near 982 °C at total strains high enough to cause appreciable plastic deformation on each cycle fatigue, crack initiation occurs at stress concentrators, such as solidification porosity and carbides. Persistent slip bands (PSB) are observed at lower temperatures in single crystal Ni-base superalloys, however, at higher temperatures (above 850 °C), PSBs have not been observed [46, 47]. Unless the applied loads during testing are high enough to allow shearing of γ' precipitates, slip is limited to the γ matrix on the most favorably oriented $\{111\}$ slip planes, and bypass of γ' precipitates occurs by combined glide and climb [45, 48]. Coarsening of γ' precipitates occurs during testing at a faster rate than unloaded aging and rafting is not observed [44]. Dislocation networks form within the first few cycles to relieve the misfit between the γ and γ' phases leading to a change in γ' morphology from cuboidal in the original as aged microstructure to spherical [44].

High-cycle fatigue occurs as a result of engine vibrations and resonance, with failure typically occurring after 10^5 cycles. The fatigue testing conditions, namely mean load and frequency, have been shown to have a significant impact on the fatigue life [49]. Wright, *et al.*, showed that the high-cycle fatigue life of superalloy specimens tested at elevated temperature (above 850 °C) and a high mean stress (R-ratio greater than 0.5) was time dependent and controlled by creep rupture life (Figure 1.13a) [49]. Due to this time dependence, higher testing frequencies improved fatigue life, as shown in Figure 1.13b with fatigue life defined as the number of cycles to failure. Tests performed at zero mean stress (R = -1) displayed no dependence on testing frequency, with crack initiation occurring at defects in the microstructure (carbides, porosity, and eutectics) [2, 49].

While low-cycle and high-cycle fatigue control life under certain service conditions,

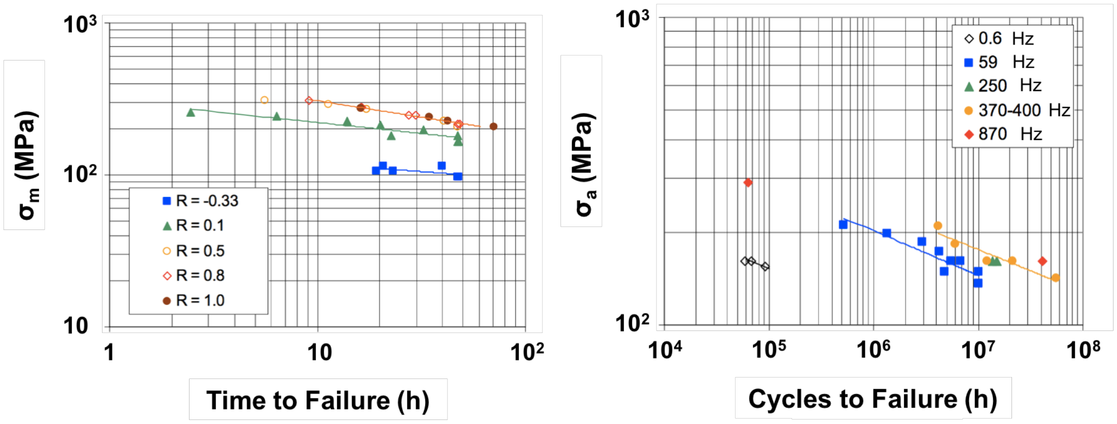

(a) (b)

Figure 1.13: Plots of a) mean stress versus time to failure and b) alternating stress versus number of cycles to failure. Higher mean stresses (R-ratio greater than 0.5) fall on the same line as a creep test (R = 1) and, thus, are controlled by creep rupture life. Fatigue testing at higher frequencies increases the number of cycles to failure, further illustrating the importance of creep deformation. Stress controlled fatigue tests were performed on platinum aluminide coated PWA1484 single crystals at 1038 °C. Taken from original work by Wright, *et al.* [49].

thermomechanical fatigue (TMF) limits life. For example, in peaking turboshaft units used for electrical generation because of a large number of start-up and shut-down cycles TMF limits life. Failure may occur in only several thousand cycles due to a combination of creep deformation and a high maximum tensile stress. During a land-based gas turbine engine startup, or take-off and landing for an aviation gas turbine engine, large thermal gradients develop between the surface and the interior near cooling holes in turbine blades, as shown in Figure 1.14a. Compressive stresses develop on the surface of the blade due to the constraint provided by the cool interior [2]. During a hold period, creep relaxes the compressive stresses and leads to the development of tensile stresses at the surface upon unloading due to the shape constraint provided by interior blade material, leading to crack formation after numerous cycles; the stress response during strain-controlled fatigue testing is shown schematically in Figure 1.14b [2, 50, 51].

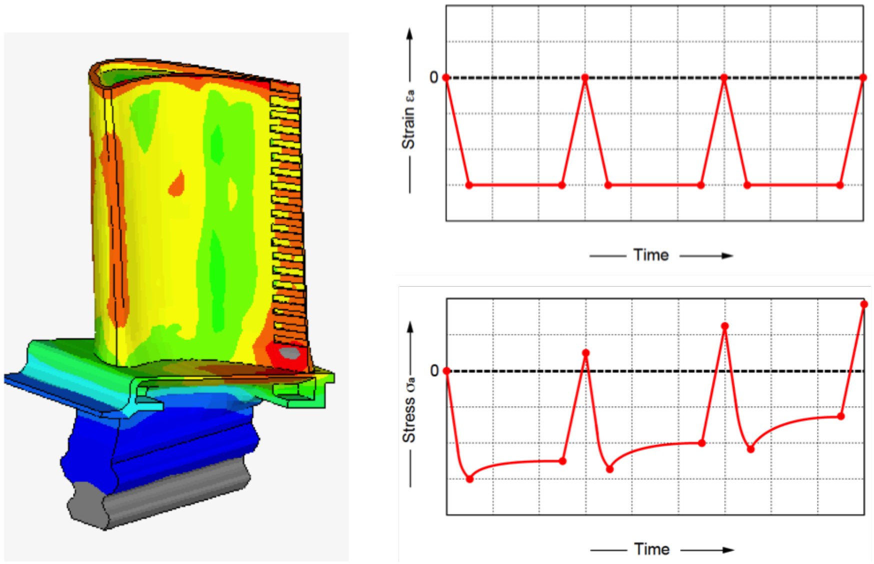

(a) (b)

Figure 1.14: a) Modeled turbine blade temperature distribution during engine operation mapped on a color scale from red to blue, with blue being the lowest temperatures; image courtesy of R. Darolia (MURI 2003 Annual Meeting). b) A schematic of a sustained peak low-cycle fatigue testing waveform showing the creep relaxation that occurs during a compressive hold in strain control; modified by Laux from original work by Evans, *et al.* [51].

During TMF, oxidation of the open crack faces occurs, creating a growth strain that induces a compressive growth stress within the α-Al_2O_3 thermally grown oxide (TGO). The growth strain arises from oxidation on the transverse grain boundaries of the TGO [52, 53]. The local in-plane compressive stress on the surface of the blades causes transverse out-of-plane extension of the substrate (Poisson effect) into the TGO-lined crack [51]. Cracks extend by the effective growth of the TGO and are accommodated by substrate creep (Figure 1.15). This process becomes more complicated in multilayer systems, where the oxidation kinetics and growth strains will vary with the crack location [54].

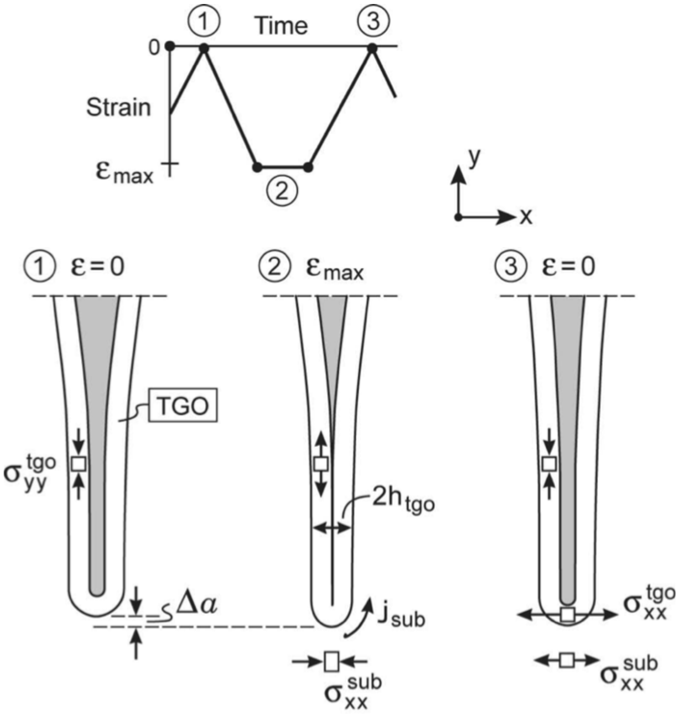

Figure 1.15: A proposed crack growth model during sustained peak low-cycle fatigue, which begins with (1) oxidation when the crack is open at a strain level of zero, corresponding to a tensile stress arising from creep relaxation. (2) during compressive loading the oxide elongates by pushing into the superalloy at the crack tip. Crack extension occurs by elongation of thermally grown oxide (TGO) and deformation of material beneath the TGO. (3) This process is then repeated each subsequent cycle. Taken from Evans, *et al.* [51].

TMF of single crystal superalloys involves cycling of both the temperature and strain in-phase or out-of-phase and may include hold periods, resulting in complex mechanical behavior. Sustained peak low-cycle fatigue (SPLCF) simplifies the process by holding the temperature constant while using a triangular waveform in compression with a hold period at maximum strain (Figure 1.14b). The hold period decreases the fatigue life substantially compared to testing without a hold period by increasing the crack growth rate by approximately 10 times due to creep deformation [50, 55]. Coatings also influence the fatigue behavior, with cracks being contained within the bond coat and interdiffusion zone (IDZ) for up to 80% of the total SPLCF life [50, 54, 56–58]. The SPLCF failure process has been observed to consist of four successive stages: "(i) crack formation and extension through the bond coat, (ii) interdiffusion zone (IDZ), (iii) superalloy substrate, and (iv) long crack growth" [54].

The most obvious form of damage during fatigue is the formation and growth of surface cracks perpendicular to the stress axis that, after a certain distance, deflect to a plane oriented at roughly a 45° angle to the stress axis [50]. Rafting is also observed to occur in the superalloy substrate during high temperature (> 900 °C) fatigue testing. For specimens coated with a bond coat, the oxidation of the crack surface leads to a local depletion of Al, which will transform from the commonly used β-NiAl coating into the more creep resistant γ' phase [50]. However, once the crack enters the superalloy substrate, Al depletion will transform the γ/γ' structure into the less creep resistant single phase γ microstructure. Subgrains have also been observed at the crack tips due to a high stress concentration. Modeling of SPLCF crack growth into a bare superalloy substrate indicates that by creating a soft layer surrounding a fatigue crack, with strength an order of magnitude lower than the bulk material, the crack growth rate increases by a factor of 2-3x [54]. As the number of

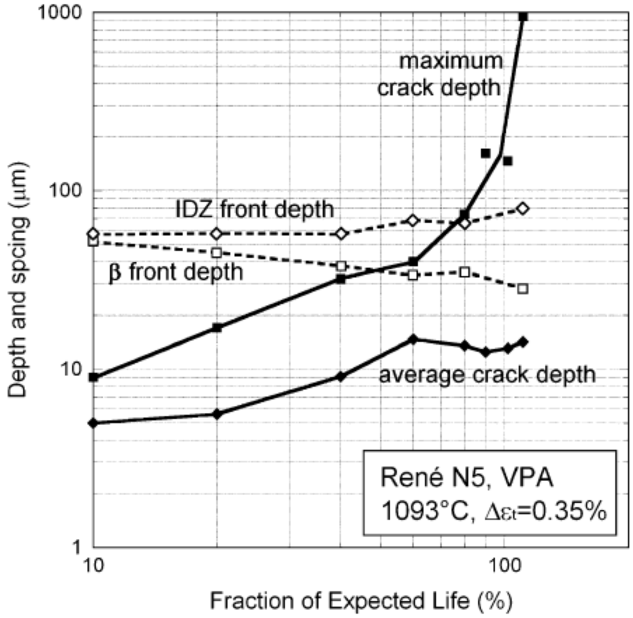

Figure 1.16: Plot of average and maximum SPLCF crack depth as a function of fraction of expected life, from Suzuki, *et al.* [50]. As expected, crack depth increases until failure, which is typically caused by a single dominant crack.

fatigue cycles increases, the average crack spacing decreases and the average crack length increases until failure, with most cracks observed after failure being contained within the coating, as seen in Figure 1.16 [50]. Suggested strategies to improve the SPLCF resistance involve (i) improving the creep resistance of the substrate (especially in compression) to delay the development of a tensile stress and for coated specimens (ii) to improve the creep resistance of the bond coat and IDZ to levels approaching the superalloy substrate because 80% of SPLCF life is spent propagating the cracks through these layers [50, 54]. Also, (iii) to decrease the growth strain in the oxide, though strategies for this approach have yet to be fully developed [54, 59].

1.4 Superalloy Component Repair

While there has been a constant increase over the past several decades in TET to improve gas turbine efficiency to save on fuel costs and lower greenhouse emissions, the repair of engine components to extend service life is another promising avenue to reduce gas turbine engine operating costs. The fundamental issues limiting the repair of the superalloy material are addressed in this thesis.

During service, superalloy turbine components degrade over time by creep and fatigue deformation mechanisms due to a complex combination of stresses at high temperatures. The degradation of turbine components is typically inhomogeneous due to the spatial variation in temperature, see Figure 1.14a, and stress. Service degradation is commonly addressed by replacing the component with a new one. The high cost of the original Ni-base superalloy components and, consequently, replacement components has encouraged the development of rejuvenation (restoration) procedures to repair turbine blades and extend useful service life. This is especially important for land-based gas turbine engines, where a single turbine blade (up to 40 lbs) can cost tens of thousand dollars, due to investment casting, coatings, composition, size and weight. Assuming a base load, gas fuel, and dry conditions, the inspection interval for the hot-gas path of a land-based gas turbine engine is 24,000 h, or 2.74 yrs [60]. Based on a variety of inspection criteria, including foreign object damage, oxidation, corrosion, cracking, deflection/distortion, and clearance limits, components may be replaced as early as the first inspection interval. If instead a repair treatment can be used to extend the component's life to the second maintenance interval (48,000 h of total service), a cost savings exists as long as the repair treatment is at least 25% less expensive than a new component, corresponding to an economic recovery factor (ERF) of 0.75 (Equation 1.2 [61] and plotted in Figure 1.17).

$$ERF = \frac{P_r}{P_n} \times \frac{L_n}{L_r} \tag{1.2}$$

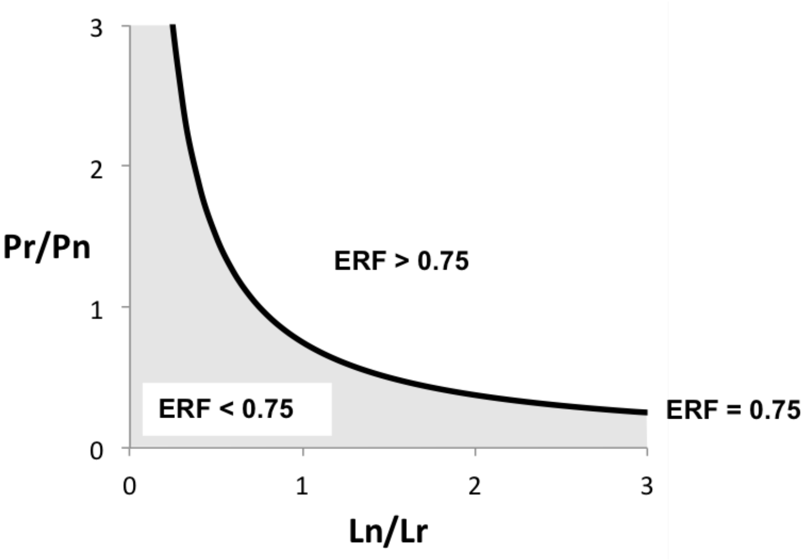

Figure 1.17: Plot of Equation 1.2 for an ERF = 0.75 to show the influence of the price and life of a repaired component. In general, an ERF < 0.75 is used as a criterion to determine if a component should be repaired rather than replaced.

Here, P_r and P_n are the price of a repaired and new component, respectively, and L_r and L_n are the life of a repaired and new component, respectively. The ERF is the generally accepted rule to determine if repair is economically viable.

The primary factors that influence service life are cyclic loading, firing temperature, fuel, and the use of steam/water cooling for land-based gas turbine engines [60]. How the engine is operated controls the maintenance inspection interval criteria. For example, General Electric (GE) uses a "starts and hours" criterion for heavy-duty land-based gas turbine engines, which depends on the number of engine starts or hours of operation, respectively [60]. For peaking units that are frequently powered on and off to meet sudden increases in power demand, fatigue limits life, so the number of starts criterion is used to determine the component inspection interval. Continuous duty engines, where oxidation, creep, corrosion, and wear limit life, an hours of operation criterion is used to determine the component inspection interval, as shown in Figure 1.18. Refurbishing or repair procedures fall into three broad categories: (i) nonstructural methods such as rejuvenation heat

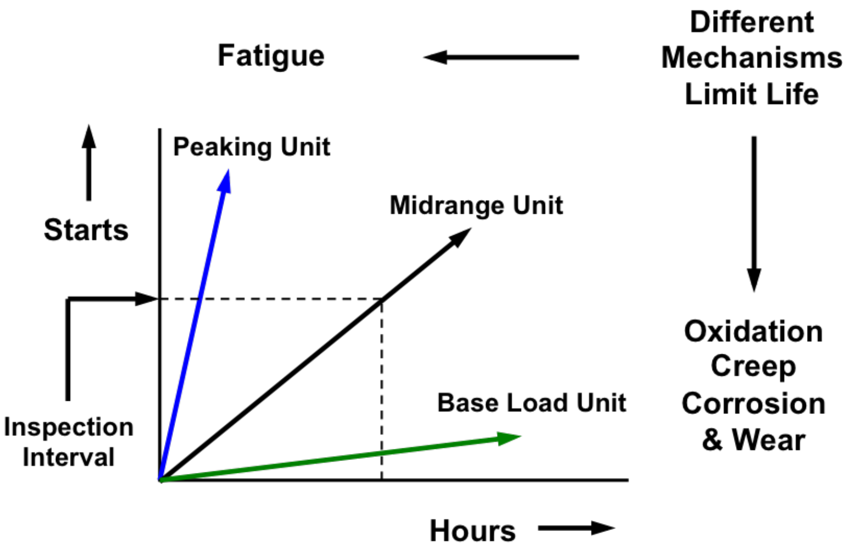

Figure 1.18: Schematic of the component life and inspection interval criteria used by GE for peaking through base load land-based gas turbine engines used for power generation. Adapted from original work by Hoeft and Gebhardt [60].

treatment, recoating, or hot-isostatic pressing (HIP), (ii) shaping by grinding or straightening, and (iii) structural methods such as welding, brazing, or component replacement [61]. This thesis will be focused on using low cost non-structural and shaping methods capable of being used in an industrial setting. In the next few sections, the processes of recovery and recrystallization as related to rejuvenation heat treatments will be discussed, important conclusions from rejuvenation literature will be made, and not yet addressed issues will be summarized.

1.4.1 Recovery of Plastic Deformation

Recovery and recrystallization are two of the primary mechanisms capable of removing stored energy due to deformation. Rejuvenation heat treatments of advanced CG and SX alloys rely on recovery to repair plastic deformation. The recovery process is driven by stored energy, primarily dislocations, in the deformed material. For commercially pure and lightly-alloyed metals (such as nickel), recovery involves the formation of dislocation cells that are microns in diameter, followed by additional rearrangement and annihilation of dislocations to create subgrains [62, 63]. During creep deformation, this process occurs dynamically leading to a steady-state creep regime as discussed previously in section 1.3.1 [64]. However, dislocations in Ni-base superalloys with a high volume fraction of γ' precipitates are unable to form dislocation cell structures during high temperature and low stress deformation. Instead, dislocations form three-dimensional nodal dislocation networks in the γ channels that are strongly influenced by the γ/γ' interfaces [24, 27]. Dislocations in the nodal networks relax the misfit between the γ and γ' phases and, consequently, are difficult to remove by annealing heat treatments below the γ' solvus temperature.

Recrystallization is typically defined as the formation and migration of high angle grain boundaries that consume deformed material [65]. Recrystallization is driven by the stored energy of deformation and, consequently, recrystallization and recovery are competing processes. However, recovery plays an important role in the nucleation of recrystallization because recrystallization nuclei are subgrains with a high misorientation to the surrounding deformed material [66–68]. Recrystallized grains in an originally CG or SX alloy introduce high-angle boundaries oriented perpendicular to the loading direction, decreasing creep rupture life as discussed in Section 1.3.1. A rejuvenation heat treatment must be capable of causing significant recovery while avoiding recrystallization, which poses a significant challenge due to the role of recovery processes in the nucleation of recrystallized grains.

1.4.2 Rejuvenation: Literature Review

A majority of the reasearch on repair has focused on nonstructural methods, beginning in the 1960s with investigations on the use of rejuvenation heat treatments to extend the creep life of the Nimonic alloy series. Due to the difficulty and expense of replicating service conditions, simple creep tests have generally been used to induce damage. A successful rejuvenation is typically defined by the following four parameters, as compared to a baseline uninterrupted test(s) to failure: the recovery of the rupture life, time to a certain percent creep strain, minimum creep rate, and creep curve behavior. Several papers published on Nimonic 80A indicate that the creep life was successfully extended by simply periodically annealing the crept samples at the creep temperature of 750 °C or at the aging temperature of 820 °C with no applied stress [69, 70]. The authors rationalized this behavior by assuming that, with the removal of the tensile load, the cavity surface tension was sufficient to cause sintering of creep cavities. However, indefinite creep life was not attainable due to extensive overaging of the microstructure. Nimonic 80A is polycrystalline with a γ' volume fraction of only 0.15 contained in a Ni-20 wt% Cr matrix.

Later rejuvenation studies involved polycrystalline alloys such as Nimonic 90, Nimonic 105, Nimonic 115, and Inconel alloys that contained a higher volume fraction of the γ' phase and more solid solution strengtheners [71–74]. Hart and Gayter found that successful rejuvenation depended on the creep conditions, namely the stress and temperature [73]. When voids grew as a result of stress-directed vacancy flow at high temperatures and low stresses (807 °C, 108 MPa), they could be sintered via heat treatment at the creep temperature, extending creep life. However, when cracks were initiated by grain boundary sliding during creep testing at lower temperatures and higher stresses (650 °C, 597 MPa), a rejuvenation heat treatment was unable to repair the damage and extend creep life. It became apparent from these early studies that the design of a successful rejuvenation heat treatment requires knowledge of the dominant tertiary creep mechanism in the alloy at the creep conditions of interest [75], unsuccessful rejuvenation being a direct result of incomplete recovery of the dominant tertiary creep mechanism.

In order to restore creep behavior, previous studies have generally used complex heat treatments involving solutioning and aging. If creep cavities or cracks were present, then hot isostatic pressing (HIP) was also required to extend creep life. However, a number of studies were conducted such that tests were interrupted prior to the formation of creep cavities or cracks to avoid using HIP. For example, successful repair procedures for Nimonic 105, Nimonic 115, and IN100, where microstructural evolution initiates tertiary creep, involved only the dissolution of the γ' precipitates during solutioning, reprecipitation during cooling, and aging to a γ' size similar to the initial microstructure [73, 74]. Additionally, Dennison, *et al.*, were able to extend the creep life of IN100 by three times when compared to an uninterrupted creep test to failure by applying a solution and aging rejuvenation heat treatment after every 1% strain, as shown in Figure 1.19 [74]. In general, the use of HIP proved to be of limited benefit in alloys where the development of cavities did not occur until late in the tertiary creep regime [76, 77].

The most comprehensive rejuvenation study to date was conducted by Ross, *et al.*, on IN100(PC) and DS Mar-M200+Hf [78]. The repair procedure consisted of a rejuvenating solution heat treatment at the γ' solvus temperature and either a single or two step age. Damage was induced by either creep, fatigue, or fatigue tests with a hold period at maximum tensile strain. The maximum recoverable creep strain for both IN100(PC) and Mar-M200+Hf(CG) was 1%, with creep test conditions of 899 °C/276 MPa and 982 °C/172 MPa for IN100(PC) and Mar-M200+Hf(CG), respectively. Multiple rejuvenation of Mar-M200+Hf(CG), interrupted at every 1% strain, was successful up to a total creep strain

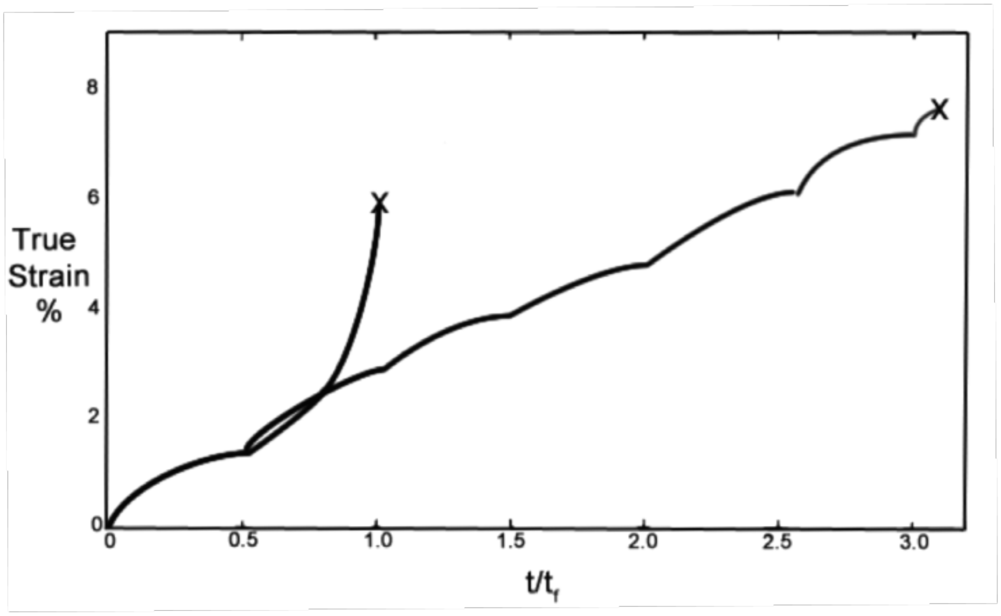

Figure 1.19: Creep curves measured during a multiple rejuvenation test of Ni-base superalloy IN100(PC). Creep tests were performed at 950 °C and 185 MPa with one specimen tested to failure and the other interrupted and rejuvenated every 42 hours, leading to a factor of three extension in rupture life. Figure taken from original work by Dennison, *et al.* [74].

of 3%, after which the minimum creep rate increased and the time to an additional 1% strain significantly decreased, as shown in Figure 1.20. Surface cracking, detected by visual and fluorescent penetrant inspections, was believed to be the cause of the loss of creep properties. Rejuvenation of specimens tested in fatigue or dwell fatigue showed no improvement, or in some cases a decrease in the total number of cycles to failure compared to a non-rejuvenation baseline test. The authors also attempted to use eddy current inspection to non-destructively evaluate the surface or subsurface strain damage at various levels of creep strain up to 3%. No difference between the untested and crept specimens was detected, suggesting that either no significant damage was present in specimens with up to

3% creep strain or that the eddy current inspection technique was not sensitive enough [78].

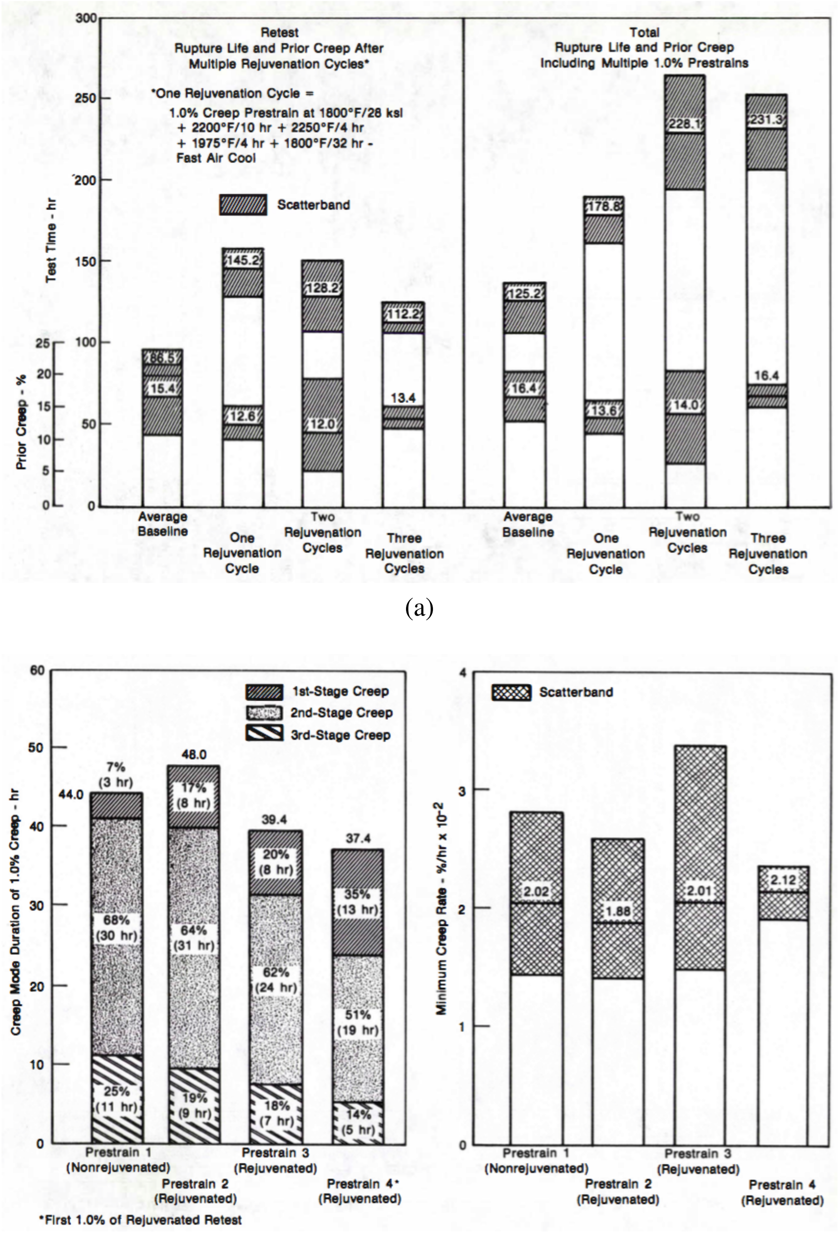

(a)

(b)

Figure 1.20: Multiple rejuvenation tests of a Mar-M200+Hf(CG) specimen interrupted at every 1% creep strain; from Ross, *et al.* [78]. a) Tracking the total creep rupture life indicated no difference in life between two and three rejuvenation cycles. b) The minimum creep rate remained fairly constant during four creep tests to the 1% creep strain threshold and a majority of creep time was spent in the primary and secondary creep regimes.

Repair procedures have also been applied to specimens machined from service-exposed turbine blades. Wortmann applied HIP repair procedures to creep and fatigue specimens machined from Nimonic 108(PC) blades that had been in service for half of their expected operating lives [79]. Creep tests were conducted at 890 °C/190 MPa, with tertiary creep expected to be initiated by creep cavity formation on grain boundaries oriented perpendicular to the loading axis. HIP was performed at 1065 °C (above the γ' solvus) at 140 MPa for 1 h followed by aging. Rejuvenated specimens exhibited a mean rupture life of approximately double the baseline, with fatigue life being unaffected.

Maccagno, *et al.*, reported similar results for IN713C(PC) turbine blades [80]. The most successful rejuvenation treatment consisted of a heat treatment and HIP, with creep life being restored to the undeformed baseline levels as long as topologically close packed phase were not present. The size and distribution of γ' precipitates were similar to those in the pre-crept blades due to the HIP above the γ' solvus temperature and subsequent aging.

Work conducted by Lvova, on GTD111(PC) turbine blades focused on drawing correlations between the microstructure and stress-rupture lives of specimens machined from the blades [81]. Stress-rupture tests were performed at 815 °C/480 MPa. Both blades examined had been operating in the same engine for 12,781 h, however “Blade 2” was rejuvenated after 24,000 h of service in another engine, while “Blade 1” had been put into the engine new. The repair procedure was considered proprietary, however, it is known that Blade 2 had been recoated and HIP was not performed. The stress-rupture life of specimens machined from the airfoil section of Blade 1 had double the life of Blade 2 specimens.

Based on metallographic examination, the reason for the discrepancy in stress-rupture lives was attributed to the decomposition of primary MC carbides. While both blades displayed similar carbide decomposition mechanisms, agglomeration of excessive secondary $M_{23}C_6$ carbides at the grain boundaries was more prevalent in the rejuvenated Blade 2, leading to easy crack formation and growth [81]. McCall also observed a significant change in carbide morphology after service and heat treatment, with the formation of a narrow film of MC and $M_{23}C_6$ carbides on grain boundaries in IN700(PC) and INX750(PC) turbine blades [82]. Conducting rejuvenation heat treatments at shorter service life intervals was suggested to minimize the primary MC carbide decomposition and subsequent $M_{23}C_6$ carbide grain boundary precipitation. Lamberigts, *et al.*, performed repair procedures on specimens machined from Mar-M-200+Hf(CG) turbine blades [83]. Service damage was simulated by performing stress-rupture tests. HIP at a temperature near the γ' solvus (1230 °C), followed by full solutioning and aging, was used to completely heal γ' rafting and incipient melting. The performance of rejuvenated specimens fell within the experimental scatter of pre-crept specimens.

1.4.3 Summary and Important Conclusions

Based on the published work on rejuvenation of Ni-base superalloys, the following observations are relevant:

- Repair procedures used in literature consist of HIP and/or solution + aging rejuvenation heat treatments near or above the γ' solvus temperature. The effect of the coating is rarely considered and recoating procedures are generally not used.

- The most commonly used criteria to determine the effectiveness of a rejuvenation procedure are the recovery of the baseline creep rupture life for tests performed to failure after rejuvenation or the time to a creep strain threshold for interrupted tests. A creep strain threshold is required to perform multiple rejuvenation tests and involve repeated cycles of creep testing to the threshold creep strain level followed by rejuvenation. In some cases the minimum creep rate and shape of the creep curve are also monitored.

- The maximum amount of creep deformation experimentally determined to be recoverable by heat treatment (solution + aging) varies between 1-3% strain.

- Creep testing has been employed to induce damage in nearly all rejuvenation studies, with only a few investigators employing fatigue testing.

- In the limited studies that have performed fatigue testing, rejuvenation has never been successful in recovering fatigue properties in either low-cycle, high-cycle, or dwell-fatigue. It should be noted that the reasons for failure are unknown and have been poorly investigated.

- The Ni-base superalloys investigated have been conventionally cast except in a few rare cases, which during service are exposed to less severe conditions (firing temperatures) compared to the modern alloys currently employed in turbine engines.

- HIP provides additional recovery compared to conventional heat treatment when cavities or cracks are present, as the addition of isostatic pressure causes them to sinter. In DS alloys in which creep cavitation is not observed until late in the tertiary creep regime, HIP provides limited benefit if specimens are rejuvenated after secondary or early tertiary creep. Some authors have shown success with using HIP on DS alloys after low creep strain, however, HIP in these scenarios also serves as a solution treatment if performed near the γ' solvus and this is the likely reason for the recovery of creep properties.

- In order to develop a successful repair procedure, the damage mechanisms that occur during tertiary creep must be characterized in detail, particularly in CG or SX alloys, where the tertiary creep regime often accounts for a large fraction of the total creep life.

- Some authors report that rejuvenation treatments can be applied indefinitely, however they fail to test this hypothesis by performing multiple rejuvenation heat treatments. Generally it has been concluded that creep rupture life cannot be extended indefinitely via rejuvenation due to accumulated physical damage that is not recovered.

- Recrystallization is generally not discussed in the rejuvenation literature. This may be a result of the use of PC Ni-base superalloys, where recrystallization would be expected to have less of an impact on the mechanical properties than in DS alloys. Also, advanced microscopy instruments including electron backscatter diffraction

(EBSD) had not been widely available.

1.4.4 Unanswered Questions & Challenges Limiting Successful Rejuvenation

Based on the available rejuvenation and repair literature along with the available work on the progression of creep and fatigue damage in both CG and SX Ni-base superalloys, a number of questions remain unanswered and motivate the investigations that will be presented in this thesis.

- Is rejuvenation possible in advanced DS alloys and, if so, at what total creep strain level is rejuvenation no longer viable? See Figure 1.21 for a schematic of a successful multiple rejuvenation test. The total creep strain in this schematic is comparable to the baseline uninterrupted creep test to rupture.
- Can rejuvenation treatments be developed to recover damage and, consequently, recover both the creep and fatigue properties?
- Can non-destructive evaluation (NDE) techniques be applied successfully to determine the presence of non-recoverable damage?
- For the case of CG and SX alloys, can recrystallization be avoided during rejuvenation heat treatments?
- How does the presence of a coating influence rejuvenation?

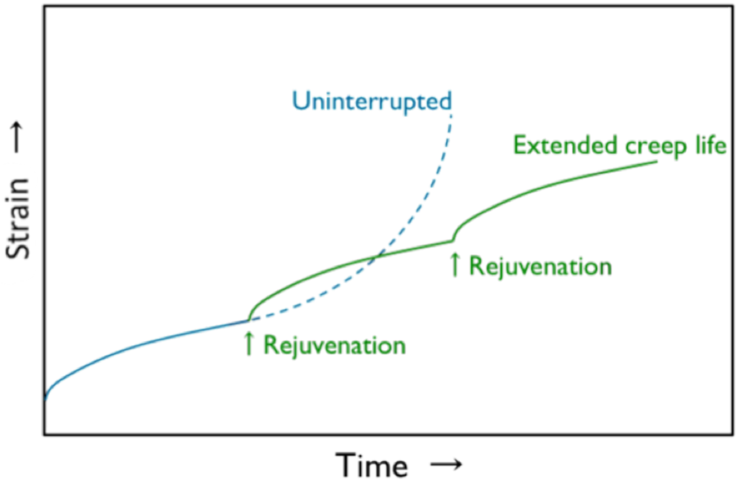

Figure 1.21: Schematic illustrating the expected result (green line) from a successful multiple rejuvenation creep test compared to an uninterrupted creep test (blue line). In this illustration, successful rejuvenation is defined by a longer total creep life when compared to an uninterrupted test.

Tertiary creep damage in GTD444(CG) and René N5(SX) is most likely a combination of several different mechanisms, which were discussed previously. It is hypothesized that the dominant tertiary creep damage mechanism is at least initially related to rafting, shearing of the γ', and an increase in the mobile dislocation density. This assumption provides guidance on the development of an appropriate repair procedure that will include only a solution + age rejuvenation heat treatment to recover the initial cuboidal γ' microstructure. By restoring the initial microstructure, the creep behavior is expected to be recovered and comparable to the virgin material. HIP is considered unnecessary due to the lack of cavitation at low strains in DS alloys. Fatigue damage is limited to rafting, localized plastic deformation, precipitate shearing, and surface cracking. Grinding/polishing away surface material to a sufficient depth to remove surface cracks will be used along with a solution +

age heat treatment to restore a cuboidal precipitate morphology.

The primary challenge limiting successful rejuvenation is finding a balance between complete recovery of the damage induced during service/mechanical testing and avoiding recrystallization during heat treatment of the DS components. A series of experiments performed on GTD444(CG) and René N5(SX) superalloy castings, outlined in the next chapter, have been performed to develop successful repair procedures to extend the life of advanced DS Ni-base superalloys.

Chapter 2

Materials and Methods

This chapter discusses the various experiments performed on Ni-base superalloy materials to explore the feasibility of recovering damage and extending service life by using rejuvenation treatments. The specifics of the mechanical testing, non-destructive evaluation, shot peening, and heat treatments performed are discussed in detail. Various microscopy analyses were also conducted to explore microstructural evolution and to elucidate the criteria required for successful rejuvenation.

The superalloy material, kindly provided by GE Power, consisted of GTD444(CG) and René N5(SX) 24 x 13 x 1.5 cm Bridgman cast plates that were solutioned and aged with standard commercial cycles prior to machining. Nominal compositions are shown in Table 1.1. Special care was taken to minimize surface residual stresses in the creep and fatigue specimens by machining with a low stress grinding processes. Specimen designs for both creep and fatigue testing are shown in Figure 2.1. The rationale for using creep and fatigue tests to induce damage is based on the reported service limiting deformation mechanisms, as discussed previously in Section 1.4. The major chemical differences between GTD444(CG) and René N5(SX) include: the absence of Ti and addition of Re in René N5(SX) along with lower levels of the grain boundary strengtheners carbon and boron.

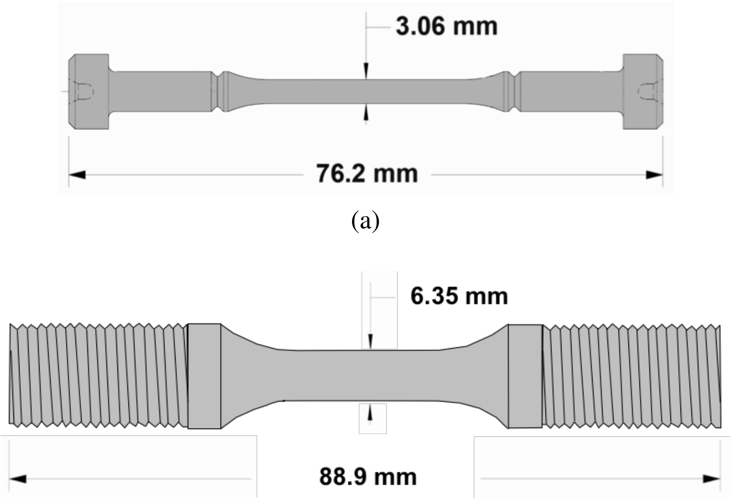

(a)

(b)

Figure 2.1: Schematic diagrams of a) the creep specimens and b) sustained peak low-cycle fatigue specimens tested in this thesis work.

2.1 Creep Testing

Creep tests were performed under constant load in air at two conditions, depending on the alloy: 982 °C/179 MPa for GTD444(CG) and 982 °C/206 MPa for René N5(SX) specimens. ATS creep frames, shown in Figure 2.2, were used to perform the creep tests according to ASTM E139-11. Initial creep specimens were tested to rupture and subsequent tests were interrupted at 2%, 5%, 10%, and 20% creep strain to examine the microstructural evolution and damage as a function of strain. All GTD444(CG) and René N5(SX) creep specimens tested were machined and consequently crept along the nominally [001] crystal direction within a 15° tolerance. Interrupted creep tests were allowed to cool under load to at least 649 °C before being unloaded and removed from the creep frame.

Figure 2.2: Image of the creep frames used to conduct creep tests on GTD444(CG) and René N5(SX) specimens.

2.2 Sustained Peak Low-Cycle Fatigue Testing

Strain controlled sustained peak low-cycle fatigue (SPLCF) testing was conducted on bare René N5(SX) . The specimens were tested along the [001] crystal direction within a 15° tolerance at a constant temperature of 982 °C in air with a strain range of 0.6% and $R = -\infty$ ($A = -1.0$). The testing waveform consisted of a 120 s compressive hold followed by a 3 s loading-unloading cycle, as shown in Figure 1.14b. The progression of fatigue damage was determined by examining specimens tested to 10%, 20%, 30%, 50%, and 75% of expected fatigue life based on one specimen tested to failure. The number of cycles to failure was defined by a 25% tensile load drop from the stabilized value. The initial SPLCF tests to failure and at various fractions of expected life were performed by Metcut® Research Inc. (Cincinnati, OH), however, due to the cost and time involved with using a third party mechanical test facility, SPLCF multiple rejuvenation testing of bare René N5(SX) specimens was conducted at the University of California, Santa Barbara using a modified MTS® (Eden Prairie, MN) hydraulic test frame, as shown in Figure 2.3.

An Ambrell® (Victorville, CA) induction heater system was used to heat fatigue specimens to the required testing temperature of 982 °C. The temperature was set and maintained by using a Eurotherm® (Worthing, United Kingdom) model 2404 controller to vary the induction heater power output and a Micro-Epsilon® (Raleigh, NC) two-color laser pyrometer to measure the specimen temperature. A two-color pyrometer, with basic components shown schematically in Figure 2.4a, measures emitted infrared radiation that increases in

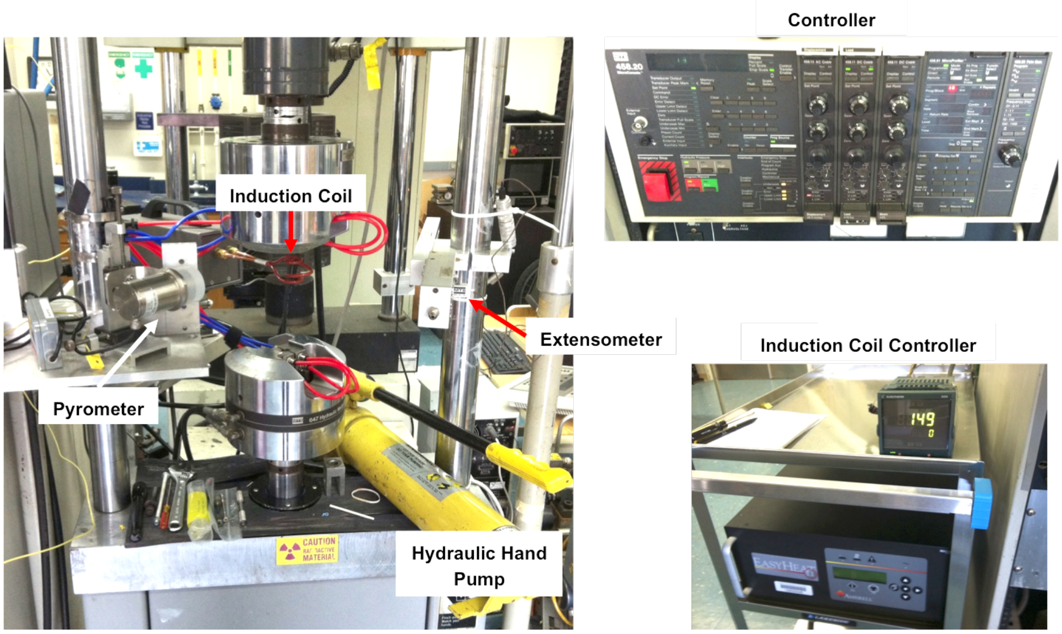

Figure 2.3: Images of the modified MTS® hydraulic test frame that was used to perform sustained peak low-cycle fatigue tests. Key components of the setup are highlighted and labeled.

intensity as the temperature of the specimen increases. The wavelength of infrared radiation varies from between 1 μm and 15 μm, see Figure 2.4b, and the baseline infrared or ”thermal radiation” intensity depends on the emissivity of the material.

A two-color sensor was employed to measure temperature from the ratio of the radiated energies in two separate wavelength bands (colors). This allows accurate measurements to be made without knowledge of the material emissivity, which is difficult to determine experimentally. However, the slope, or the quotient of the emissivities of both wavelength bands, was adjusted so the measured two-color pyrometer temperature matched the temperature determined by an R-type thermocouple in contact with the fatigue sample. The slope

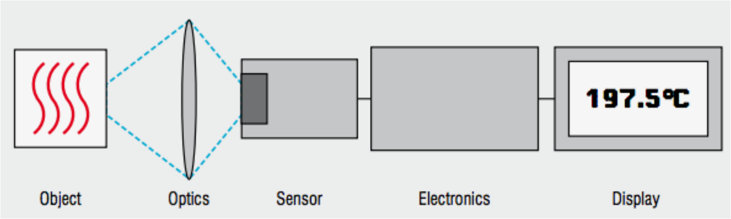

(a)

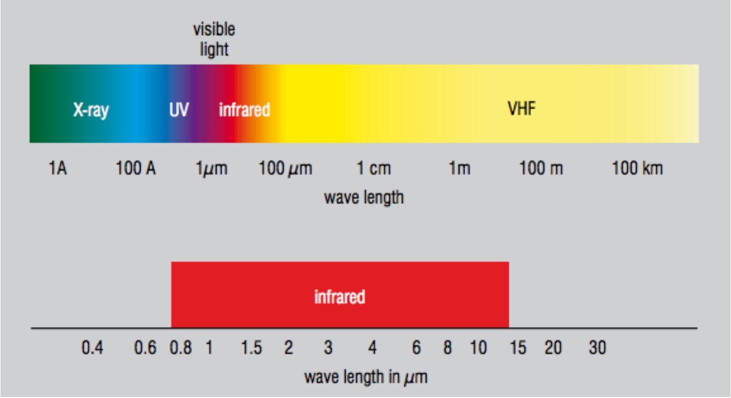

(b)

Figure 2.4: a) Diagram of the basic components contained in a pyrometry system and b) the electromagnetic spectrum with the wavelength range measured by infrared pyrometers indicated.

changed as oxidation occurred on the initially polished specimen requiring a hold time at temperature of four hours before the slope value stabilized. It is important to note that an R-type thermocouple could not be used to monitor temperature for the entire SPLCF test due to the thin wire gauge required to avoid interaction with the induction field. Typically, an R-type thermocouple would operate for roughly 12 hrs before failing.

2.3 Microstructural Analysis

The microstructure was examined for both alloys after creep and fatigue testing to determine the onset of recrystallization, extent of rafting, formation of cavities or voids, changes in carbide morphology, and precipitation of brittle intermetallic phases. The results were compared to the pre-crept microstructure. Metallographic preparation of pre-crept and crept specimens involved mounting sections parallel and transverse to the stress axis in Bakelite, followed by standard grinding and polishing with a final polish of 0.05 μm alumina. Sections were cut via electrical discharge machining (EDM) and specimens were ultrasonically cleaned after each polishing step in distilled water.

Two etchants were used to inspect the microstructure: 40% hydrochloric acid, 40% ethylene glycol and 20% nitric acid for macroetching of GTD444(CG); 33% distilled water, 33% acetic acid, 33% nitric acid and 1% hydrofluoric acid for microetching of GTD444(CG) and René N5(SX) . In some instances, a equal parts 0.05 μm colloidal silica and distilled water solution was used for a final vibratory polishing for 4 h in lieu of the 0.05 μm alumina polishing step. Due to the chemo-mechanical polishing effect of colloidal silica, additional etching was unnecessary to sufficiently reveal the γ/γ' microstructure. To fully remove the damage caused by grinding/polishing, colloidal silica was also used to prepare specimens for characterization by electron backscatter diffraction (EBSD), where the quality of the diffraction pattern significantly depends on the condition of the near-surface material, as shown in Figure 2.5.

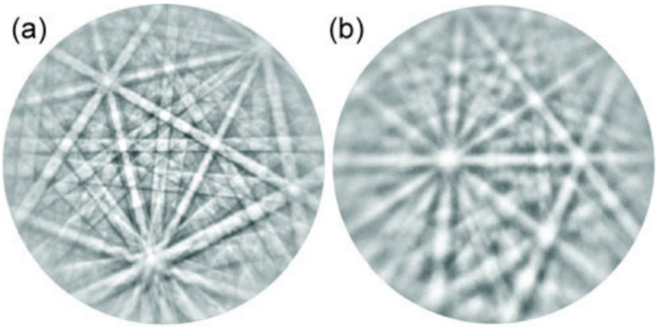

Figure 2.5: Representative EBSD patterns collected from a) well prepared and b) poorly prepared zirconium, illustrating the importance of sample preparation, taken from Wright, *et al.* [84].

Electron microscopy was performed at the microscopy facility located in the California Nanosystems Institute at UCSB. An FEI® (Hillsboro, Oregon) XL30 field emission gun (FEG) scanning electron microscope (SEM) was used exclusively to collect SEM micrographs. Detectors attached to this microscope include: standard secondary electron (SE), dedicated backscattered electron (BSE) detector, an EDAX® (Mahwah, NJ) Si-drift EDX detector for compositional analysis, and an EDAX® EBSD detector that provides crystallographic information. A 20 keV accelerating voltage and a spot size between 4 – 6 were used for SE and BSE imaging.

EBSD was performed on samples to determine the crystal orientation and, with subsequent data analysis, the local misorientation by calculation of the Kernal average misorientation (KAM) and grain orientation spread (GOS), through which the presence or absence of both dynamic and static recrystallization can also be determined. The KAM is defined for a given point (pixel) as the average misorientation of that point with respect to

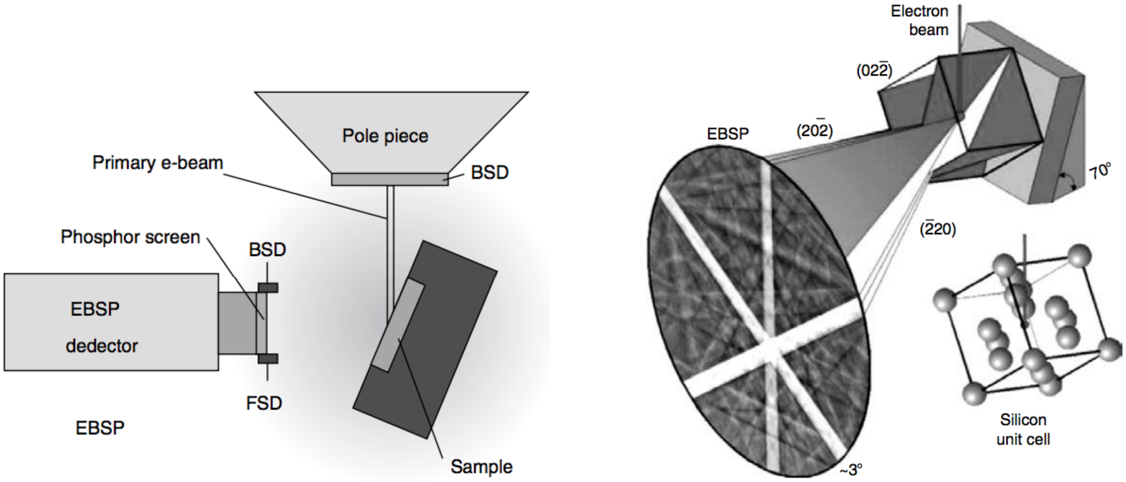

(a) (b)

Figure 2.6: Schematics illustrating a) the EBSD collection setup inside an electron microscope specimen chamber and b) the formation of Kikuchi patterns due to the generation of diffracted electrons as a result of electron beam and specimen interactions. Taken from Maitland, *et al.* [85].

its neighbors, the grain reference orientation deviation (GROD) is the orientation difference between a point and the average orientation of the point-containing grain, and the GOS is the average deviation in orientation between each point in a grain and the average orientation of that same grain, leading to the assignment of a single GOS value for each grain [84, 86, 87]. Typical scan conditions involved a sample tilt of 70 °C, a working distance of between 8 – 12 mm, beam voltage of 20 kV and a step size of 0.06 – 10 μm depending on the size of the area scanned and the features investigated. The EBSD collection setup is shown schematically in Figure 2.6. The minimum grain size was set to 5 voxels and a grain tolerance angle of 5° was used to partition the raw data.

2.3.1 Resonant Ultrasound Spectroscopy

In concert with mechanical testing, a non-destructive evaluation (NDE) technique, specifically resonant ultrasound spectroscopy (RUS), was employed for damage detection. RUS was used to monitor resonant frequency shifts primarily caused by changes in the elastic properties of the material due to recrystallization. RUS measurements were collected using a setup provided by Vibrant NDT Corporation, shown in Figure 2.7. The setup consists of four piezoelectric transducers, a transceiver unit, and a control software package developed by Magnaflux. A drive transducer sends elastic waves through the specimen from 1 – 200 kHz, while two other transducers receive the resulting amplitudes every 3 Hz. A fourth transducer is required to properly support the specimen.

Scans require approximately one hour to complete and this technique has been shown to precisely replicate resonant frequencies within 0.02 – 0.05% of the driving frequency for SiC spheres [88]. Frequencies corresponding to resonance peaks were determined and tracked to calculate a resonance frequency shift due to a change in specimen condition. RUS scans were collected from creep and SPLCF specimens in various conditions including but not limited to: the as-machined (baseline), plastically deformed, and heat treated (rejuvenated).

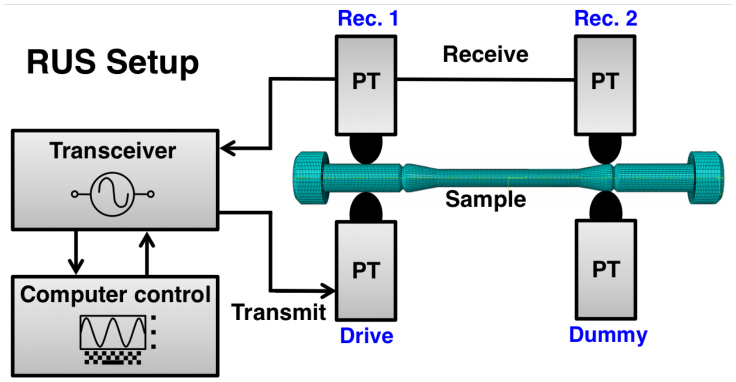

(a)

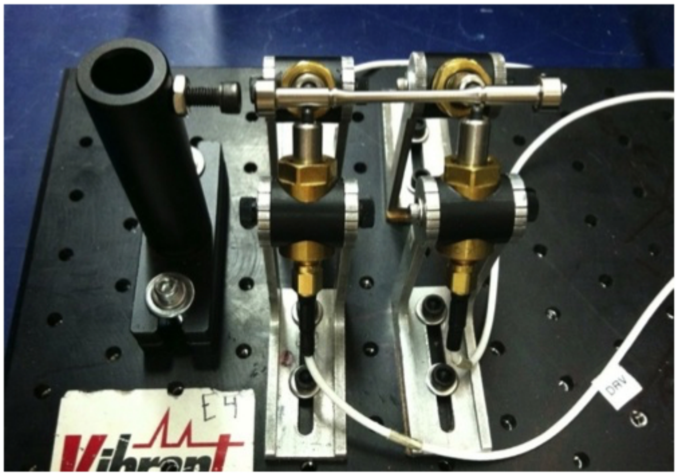

(b)

Figure 2.7: a) Schematic and b) image of a creep sample in the RUS setup developed by Vibrant and modified to inspect mechanical test specimens. The specimen rests on four piezoelectric transducers (PTs). A swept sinusoidal signal is driven through one PT from 1 to 200 kHz, exciting resonance in the specimen. Resonance generates macroscopic deflections that are measured by two other PTs that generate a corresponding voltage.

2.4 Heat Treatments

Coupons were cut from specimens of GTD444(CG) and René N5(SX) that were crept to 2% and 5% strain for initial rejuvenation heat treatment studies. Virgin coupons were also heat treated to determine the influence of strain on the dissolution, reprecipitation, and growth of the γ' phase. The heat treatment conditions are summarized in Table 2.1 with only the solution temperature being changed between experimental variants. Cooling and heating rates were chosen to be consistent with GE Power material specifications, and were performed in a reducing atmosphere of 5% H_2/Ar. All heat treatments were performed in a OXY-GON® vacuum resistance furnace, shown in Figure 2.8, that had a hot zone large enough to accommodate full size creep and fatigue specimens. A calibrated external R-type thermocouple was used to monitor the coupon/specimen temperature.

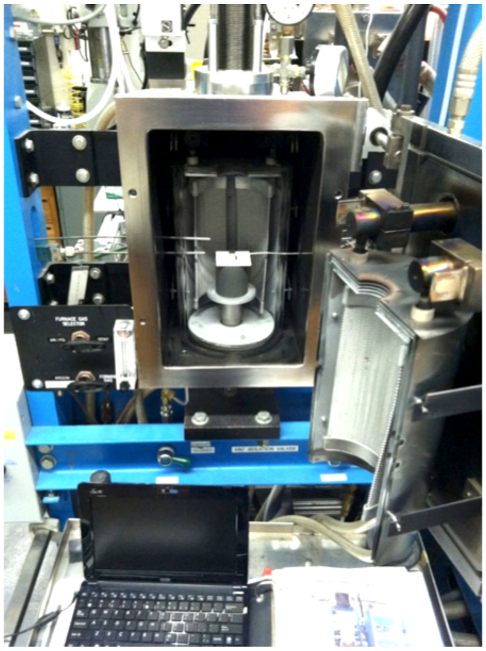

Figure 2.8: Image of the OXY-GON® vacuum resistance furnace used to perform heat treatments of coupons and mechanical test specimens in a reducing atmosphere.

Table 2.1: Summary of the rejuvenation heat treatments performed on 2% crept, 5% crept, and virgin coupons of GTD444 and René N5(SX). The only difference between heat treatments was the solution temperature, which was at either the γ' solvus temperature or at a multiple of 14 °C below the full γ' solvus temperature.

	Solution Temp.	Time (h)	Aging Temp. °C	Time
GTD444(CG)	Full Solvus	2	1079	4
	-14 °C	2	1079	4
	-28 °C	2	1079	4
René N5(SX)	Full Solvus	2	1079	4
	-14 °C	2	1079	4
	-28 °C	2	1079	4
	-42 °C	2	1079	4
	-56 °C	2	1079	4

Chapter 3

Microstructural Evolution and Damage During Mechanical Testing

In this chapter, the damage processes that occur as a function of strain during creep of a CG alloy and a SX crystal alloy are examined. Detailed EBSD analysis provides new insights that are incorporated into a creep damage model. Fatigue damage arising during SPLCF testing to various fractions of expected life was also examined through metallography and quantitative measurements of crack depth and spacing.

---

[1] The contents of this chapter have substantially appeared in references [89, 90]: L. H., Rettberg, M. Tsunekane, and T. M. Pollock. Rejuvenation of Ni-base Superalloys GTD444(DS) and René N5(SX). Superalloys 2012 (2012): 341-349 ©2012 Wiley and L. H., Rettberg, and T. M. Pollock. Localized recrystallization during creep in Ni-base superalloys GTD444 and René N5. *Acta Materialia* **73** (2014): 287-297 ©2012 Elsevier.

3.1 Creep

Creep tests of both GTD444(DS) and René N5(SX) to rupture exhibited an extended tertiary creep regime as expected. Representative strain rate and creep strain versus time plots of a René N5(SX) specimen are shown in Figure 3.1. A photograph of a GTD444(CG) specimen crept to rupture, Figure 3.2, shows significant necking that extends several millimeters away from the fracture surface. Metallographic examination of additional constant load creep tests performed to 2%, 5%, 10% and 20% strain provided information on rafting, cavitation, and localized dynamic recrystallization, a newly observed creep phenomenon for DS Ni-base superalloys. Refer to Section 2.1 for additional details on the creep testing procedure.

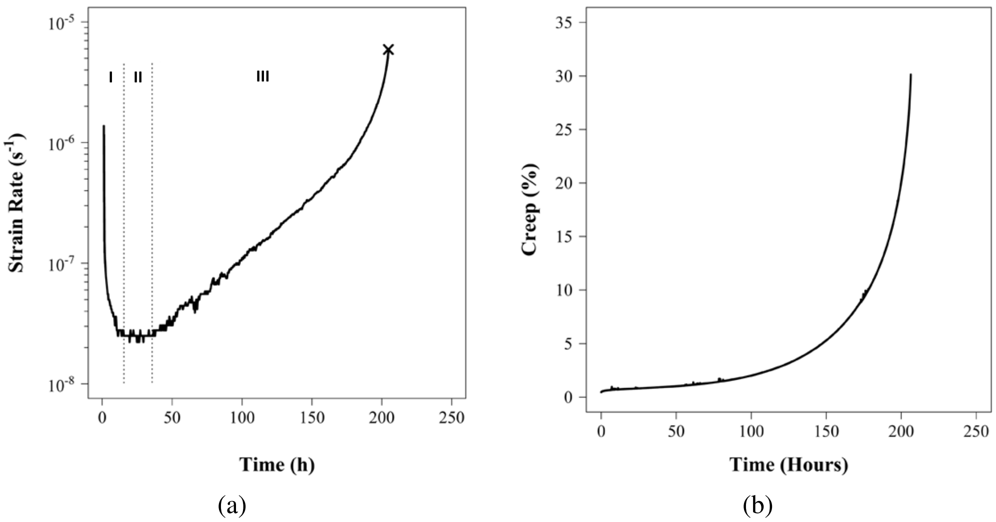

(a) (b)

Figure 3.1: a) Creep strain rate with the I. primary, II. secondary, and III. tertiary creep regimes labeled, and b) creep strain plotted as a function of time. The data was obtained from a creep test of a René N5(SX) specimen at 982 °C/206 MPa.

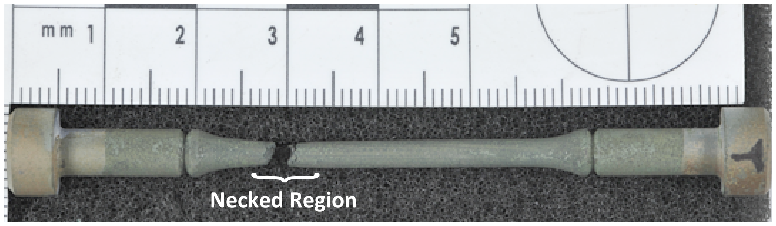

Figure 3.2: Photograph of a GTD444(CG) specimen crept to rupture at 982 °C/179 MPa. Notice the significant necking near the fracture surface.

3.1.1 Microstructural Evolution

Examination of the post-test microstructure indicated that, due to the negative lattice misfit of both alloys, rafting occurred perpendicular to the stress axis, Figure 3.3. Rafting is unavoidable in the studied alloys due to the level of misfit present in most commercial alloys. The rafted structure coarsens over time at high temperature, resulting in the thickest rafts being observed after failure. Complete inversion of the microstructure (γ' becoming the continuous matrix phase) did not occur likely due to the low volume fraction of the γ' phase in the alloys investigated. The formation of the rafted structure is well studied, although its effect on the creep behavior is a subject of much debate in literature, with many authors reporting contradictory results. Early work indicated that rafting improved the creep performance, however, subsequent reserach has shown that the influence of rafting depends on the superalloy and the test conditions [27, 91]. It is currently believed that during testing at higher stresses, rafting is detrimental to creep performance, and during testing at low stresses, it is beneficial [30, 92, 93]. At high stresses, dislocations can cut the γ' rafts and the overall effect of rafting on the creep performance is detrimental due to concurrent coarsening of the microstructure. At low stresses, where climb is the rate controlling mechanism and the dislocations cannot readily penetrate the γ' rafts, the dislocations circumvent the rafts by climb and glide. Thus, since rafting creates long horizontal interfaces, it is expected that the creep resistance will be improved [22].

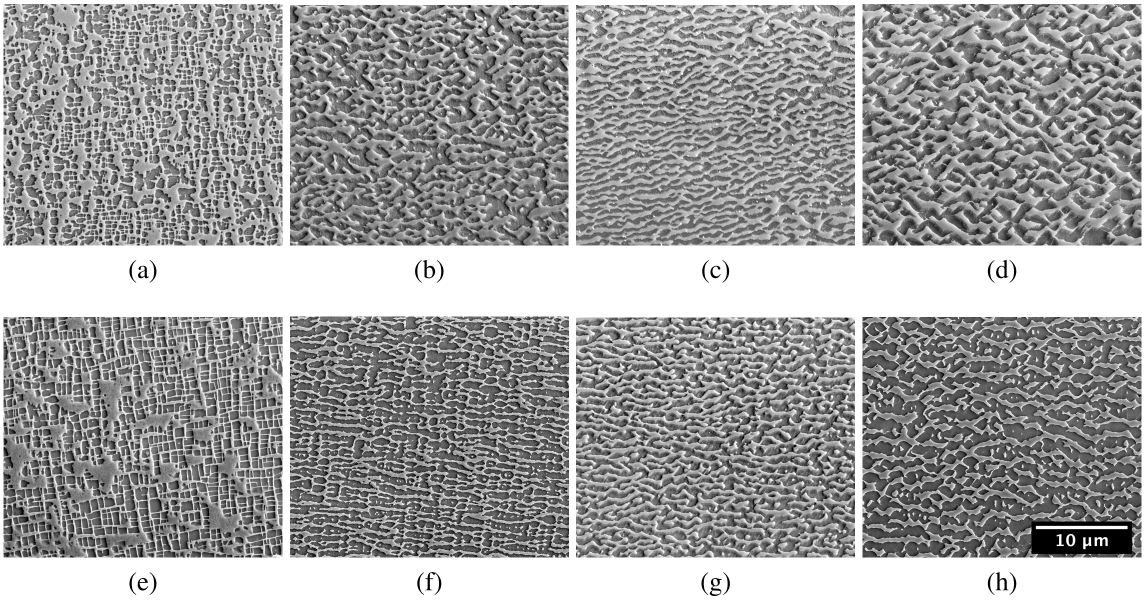

Figure 3.3: Montage of secondary electron micrographs showing the progression of rafting as a function of accumulated creep strain for GTD444(CG) a) virgin, b) 2% creep strain, c) 5% creep strain, and d) post-failure, and similarly for René N5(SX) (e–h). The stress axis is along the vertical direction of the page. The scale is the same for all images and the samples were etched. The etchant used for both alloys consisted of 33% distilled water, 33% acetic acid, 33% nitric acid, and 1% hydrofluoric acid.

Creep cavitation was also monitored at the tested levels of creep strain by using optical microscopy, Figure 3.4. No significant creep cavitation was observed at 2% or 5% creep in either alloy. The René N5(SX) specimen crept to approximately 20% did show minor cavitation, Figure 3.5, and extensive cavitation was observed near the fracture surface in post-failure specimens.

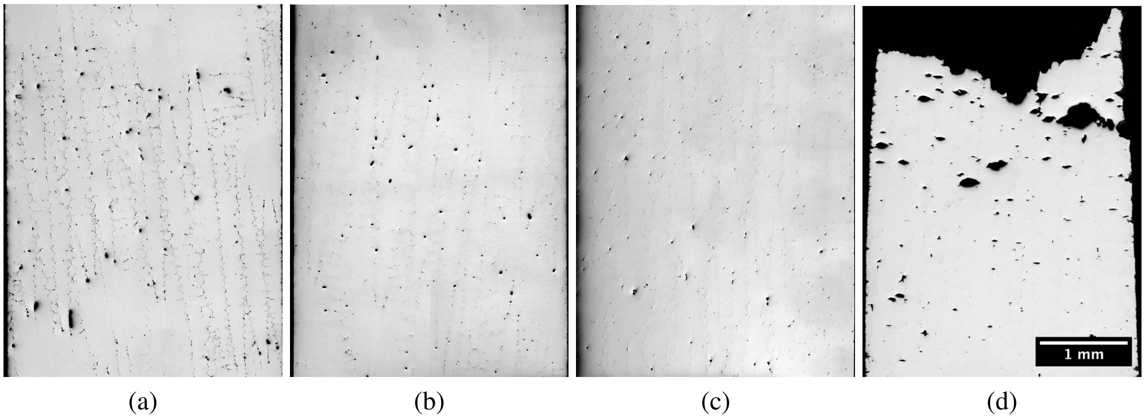

(a) (b) (c) (d)

Figure 3.4: Montage of optical micrographs showing the initial porosity and creep cavitation in René N5(SX) as a function of strain. The microstructure was examined in the a) virgin, b) 2% strain, c) 5% strain, and d) post-failure conditions. The amount of porosity and creep cavitation for GTD444(CG) was similar to René N5(SX) at all conditions. The scale is the same for all images and the samples were imaged in the as polished condition. The stress axis is along the vertical direction of the page.

Close examination of the cavities in a failed specimen revealed that the cavities are typically located in the interdendritic regions near carbides, Figure 3.6. Cavities are also commonly reported in literature to form around carbides, topologically close packed (TCP) phases, and casting porosity in the interdendritic regions of the microstructure [39, 94–97]. Carbides and TCP phases are hard, non-deforming particles and act as stress concentrators, resulting in enhanced dislocation activity in surrounding areas and crack formation. Likewise, pores, inherent to the casting process, are defects that can grow readily into cavities during creep.

An interesting result was reported by Ai, *et al.*, in a CMSX-2(SX) specimen with only 15 ppm carbon that was crept to 15% strain at 850 °C/520 MPa [38]. The authors determined that the number of pores in the as-received material was comparable to the number

Figure 3.5: Optical micrograph showing creep cavitation in a René N5(SX) specimen crept to approximately 20%. The stress axis is along the horizontal direction of the page.

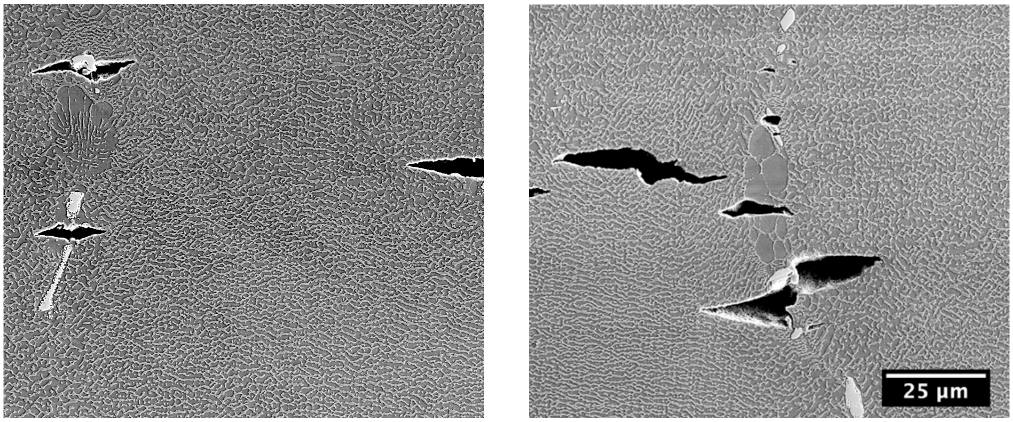

Figure 3.6: Secondary electron micrographs of creep cavities in a René N5(SX) specimen crept to rupture. The loading direction is along the vertical direction of the page. The scale is the same in both images.

of pores in a specimen interrupted during advanced tertiary creep, indicating limited nucleation of new cavities during creep. This was attributed to the low carbon levels in the alloy and the associated low fraction of carbides. Failure should then be controlled by the rate at which existing defects (porosity) grow. However, it should be noted that these results were collected from 2D sections and may not be represent the true behavior. Both alloys used in this study have carbon levels an order of magnitude higher than the CMSX-2(SX) alloy used in Ai's work.

Two EBSD scans were collected from an area with the largest observed cluster of creep cavities in a GTD444(CG) specimen crept to rupture, as shown in Figure 3.7. The inverse pole figure maps and, more clearly, the GOS maps of EBSD Scan 1 indicate that recrystallization has occurred; similar results were observed in René N5(SX) samples, see Figure 3.8. This is an interesting result as the coherent γ' precipitates would be expected to provide a significant barrier to the growth of recrystallized grains; this will be discussed in more detail in a later section.

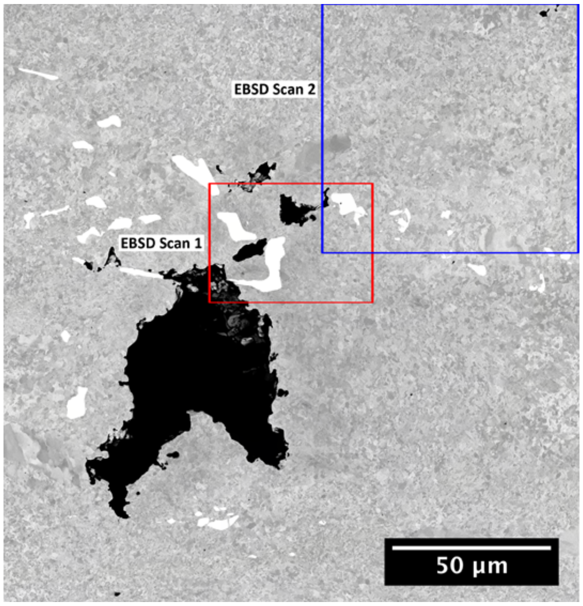

Figure 3.7: Backscatter electron image of a cluster of creep cavities located near the fracture surface in a GTD444(CG) specimen crept to rupture. Two electron backscatter diffraction scans were collected from this region, EBSD Scan 1 and EBSD Scan 2, which correspond to Figures 3.8 and 3.9, respectively. The loading direction is along the horizontal direction of the page.

The areas around creep cavities near the fracture surface are misoriented by as much as 40° compared to the cavity-free regions. The crystallographic orientation of the recrystallized grains is random, indicated in Figure 3.8(d), and the average grain diameter is 0.71 μm with a standard deviation of ±0.46 μm. A GOS value of less than 3° was used as the cutoff between recrystallized and non-recrystallized material, as shown in Figure 3.8(c). Scans of other areas indicated that recrystallization typically occurred near carbides and around creep cavities, especially in the areas connecting neighboring cavities. Figure 3.9, the area of which corresponds to EBSD Scan 2 in Figure 3.7, shows two clusters of creep cavities connected by a band of recrystallized grains over a distance of ~70 μm. Recrystallization was not observed around every carbide or cavity and was less common in areas further away from the fracture surface. Based on the available literature, subsurface dynamic recrystallization during creep in DS Ni-base superalloys has not been reported previously. This may be due to the difficulty in detecting the presence of recrystallized grains, which is not obvious in SE or BSE micrographs, see Figures 3.7 and 3.8a.

Limited recrystallization was also observed in a René N5(SX) creep specimen interrupted at 20% strain, occurring in small ligaments of material near creep cavities that were presumably deformed significantly, as shown in Figure 3.10a. Similar to GTD444(CG), after rupture, René N5(SX) specimens showed bands of recrystallized grains connecting nearby creep cavities, see Figure 3.10b. After holding a René N5(SX) specimen at 982 °C for 50 h after rupture, the recrystallized grains grew to an average diameter of ~2.3 μm, as shown in Figure 3.10c. The recrystallized grains are believed to grow by the dissolution

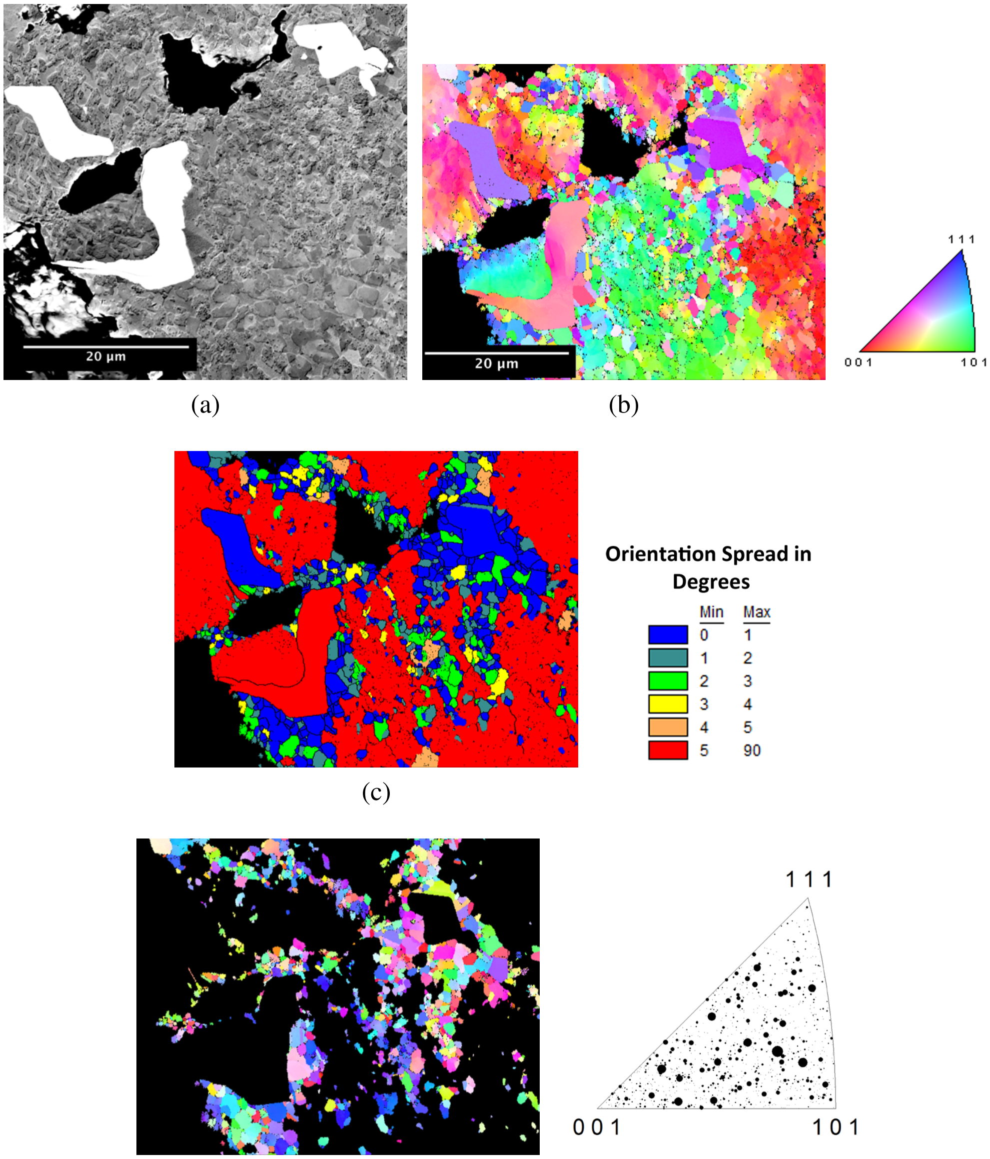

(a) (b)

(c)

(d) (e)

Figure 3.8: a) Backscatter electron image, b) loading direction inverse pole figure map, and c) grain orientation spread map from a GTD444(CG) specimen crept to rupture. The loading direction is along the horizontal direction of the page. The bright white regions in (a) are carbides. Maps were collected in the interdendritic regions near the fracture surface. d) Partitioning the scan to include only grains with a grain orientation spread less than 3° allows the texture of the recrystallized grains to be determined (e). Points in (e) are scaled by the size of the grain they represent. All EBSD maps have the same scale.

of the γ' precipitates at the grain interface followed by discontinuous precipitation to relieve the supersaturation of solute, Figure 3.10d. Some grains (<2 μm) were composed of only the γ or the γ' phase.

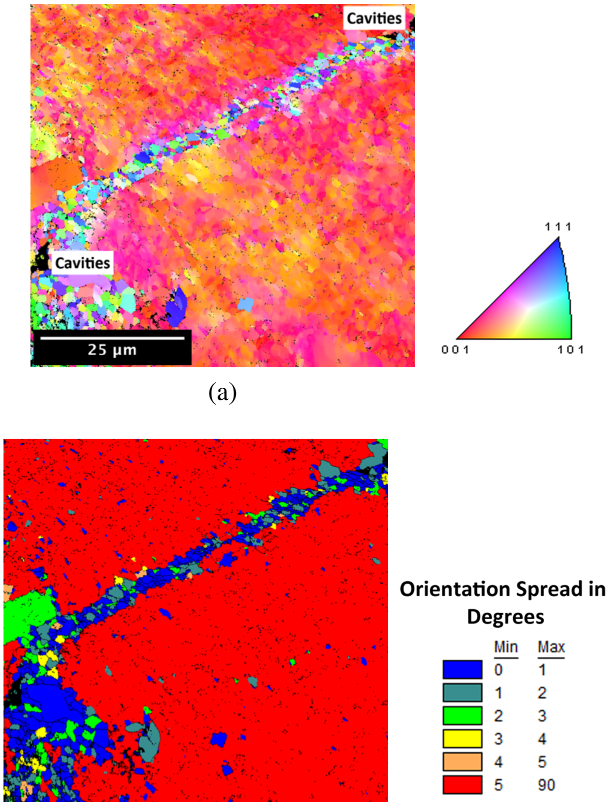

(a)

(b)

Figure 3.9: a) A band of recrystallized grains connects two groups of creep cavities in a loading direction inverse pole figure map from a GTD444(CG) specimen crept to rupture. b) A grain orientation spread map is shown from the same region. The loading direction is along the horizontal direction of the page. Both maps have the same scale.

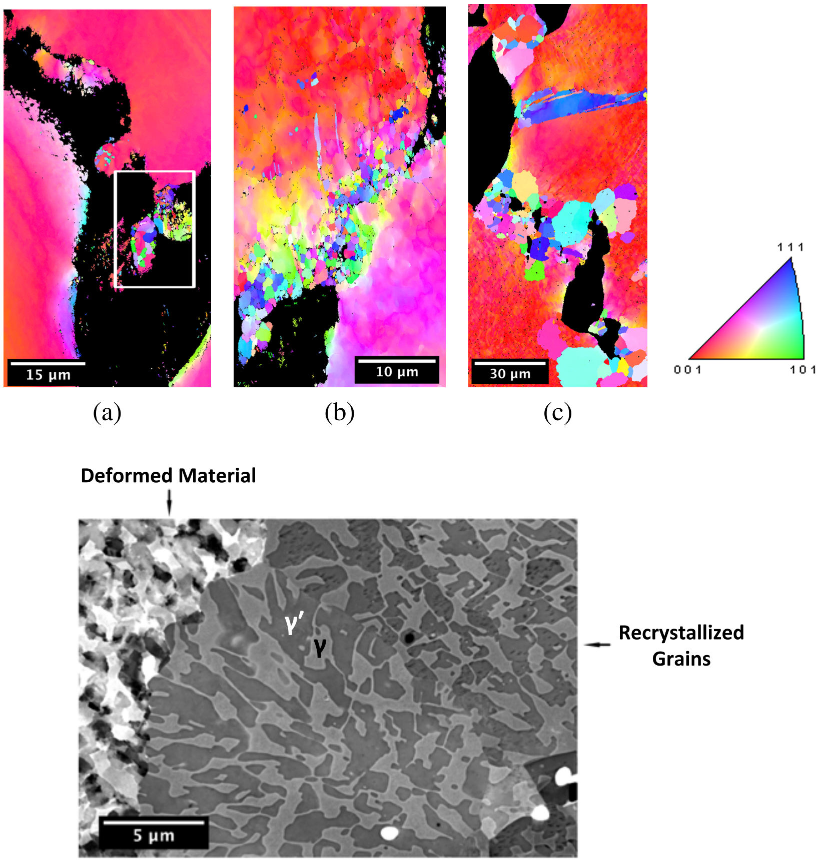

(a) (b) (c)

(d)

Figure 3.10: Inverse pole figure maps with respect to the loading direction of René N5(SX) specimens a) crept to 20% strain, b) after rupture, and c) held at 982 °C for 50 h after rupture. The region of recrystallization is highlighted by a white box in (a). d) To characterize the particle-interface interaction, backscattered electron micrographs were collected. The loading direction is along the horizontal direction of the page.

3.1.2 Localized Dynamic Recrystallization

Although briefly mentioned in Section 1.4.1, the discovery of localized dynamic recrystallization in crept specimens warrants a more detailed discussion of the recrystallization process specific to advanced Ni-base superalloys with significant ($\geq 50\%$) volume fraction of the γ' phase. The driving force for recrystallization is the stored energy in the material, as reflected in the dislocation density. The boundary energy of the newly formed grain and the coherent γ' precipitates serve as the barriers to recrystallization. During recrystallization in Ni-base alloys there are two types of boundary-particle interactions of relevance [98]:

1. Dissolution of γ' precipitates at the moving interface and reprecipitation in the new grain, either discontinuously or continuously.
2. Pinning of the boundary by γ' precipitates and coarsening with solute supplied along the grain boundary.

The balance between the local driving force and local barriers to recrystallization determine which type of interaction will occur. It has been observed experimentally, Figure 3.10d, that type (1) is active during creep at 982 °C/179-206 MPa provided that the strain is ≥ 20%, meaning that a high level of stored energy is needed to overcome the local barriers. The onset of dynamic recrystallization in Ni-base superalloys is examined in the following sections and approximate calculations examine the stored energy and recrystallization barrier.

3.1.2.1 Nucleation

During high temperature creep in the present study at $T/T_m \simeq 0.7$, the stored energy is expected to be low. Unlike bulk single phase Ni, Ni-base superalloys do not form a well-defined subgrain structure, making the nucleation of recrystallized grains inherently difficult [27]. However, in local highly deformed regions, subgrains have been observed in Ni-base superalloys [99, 100]. The observations in the present study demonstrate that the presence of cavities and carbides in GTD444(CG) and René N5(SX) can result in local regions of high deformation and the formation of subgrains, meeting a critical criterion for initiation of dynamic recrystallization [101]. In general, a particle stimulated nucleation (PSN) mechanism requires a large (> 1 μm) non-deforming particle (such as a carbide) as a site for the development of a recrystallization nucleus because, during deformation, the region surrounding the particle contains a high dislocation density and large orientation gradient [102]. The alloys investigated in this study contain carbides that are significantly larger, as shown in Figure 3.7, than the 0.5-2 μm critical particle radius required for a recrystallized nucleus to grow in Al alloys as determined by Humphreys [103].

3.1.2.2 Stored Energy

The stored energy in a material containing non-deformable particles, carbides in this case, is approximated by consideration of the contributions from the geometrically necessary dislocations (GND), and statistically stored dislocations (SSD) [104, 105]. The GNDs form low-angle boundaries and the stored energy of these boundaries can be approximated by using the Read-Shockley equation (Equation 3.1) [106]. The misorientation, θ, is in radians, while E_0 is a constant depending on the elastic properties of the material (shear modulus, G, Burgers vector, b, and Poisson's ratio, ν) and A depends on the core energy of a dislocation (dislocation core radius, r_0). The kernel average misorientation (KAM) map of EBSD Scan 1 (Figure 3.11) shows areas with up to 5° of misorientation with the average KAM being 1°.

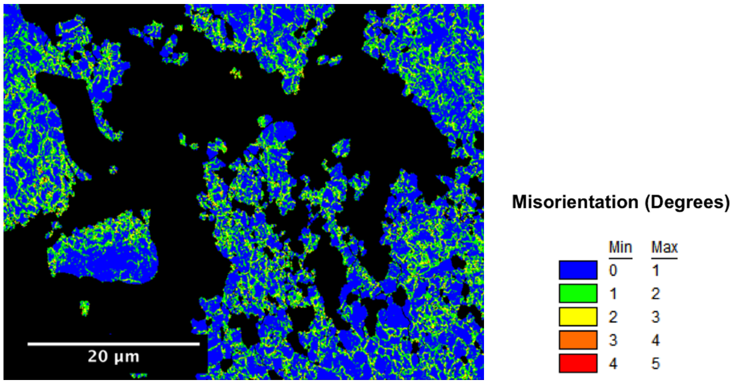

Figure 3.11: Kernel average misorientation map of the same area shown in Figure 3.8. Recrystallized grains and carbides have been segmented out of the map.

$$\begin{aligned} E &= E_0\theta(A - \ln\theta), \\ \text{where } E_0 &= \frac{Gb}{4\pi}(1-\nu) \\ \text{and } A &= \ln\left(\frac{b}{2\pi r_0}\right) + 2/e \end{aligned} \tag{3.1}$$

Using $\theta = 0.087$ radians, $G = 48.2$ GPa, $b = 0.25$ nm, $\nu = 0.25$, $r_0 = b$, and 2/e $\simeq$ 1 leads to a calculated energy per unit area of 217 mJ/m^2. This compares favorably with calculations performed by Sangid, *et al.* [107]. Assuming a hexagonal array of subgrains with an estimated size of 1 μm, the energy per unit volume is 0.718 MJ/m^3.

Calculations to determine the SSD density, ρ_s, are based on the Orowan equation (Equation 3.2), where $\dot{\gamma}$ is the shear strain rate, ρ_m is the mobile dislocation density, and v_c is the climb velocity; all other terms have been defined previously. In Ni-base superalloys, the statistically stored dislocation density consists nominally of the mobile dislocation density and the misfit dislocation density. Misfit dislocations accumulate at the γ/γ' interface to reduce the elastic energy associated with misfitting precipitates. In this sense, misfit dislocations lower the elastic energy of the system and do not provide an additional driving force for recrystallization. Thus, it is assumed that the mobile dislocation density, as required by the Orowan equation, is approximately equal to the SSD density.

$$\dot{\gamma} = \rho_m b v_c \tag{3.2}$$

Srinivasan, *et al.*, have calculated the $a/2\langle 110\rangle$ dislocation climb velocity in CMSX-4 at 1000 °C to be approximately 4×10^{-8} m/s [108]. The axial creep rate near rupture has been determined experimentally and is approximately 6×10^{-6} /s; however, this is the macroscopic creep rate, which will vary from the local creep rate near creep cavities where recrystalllization is observed. The local creep rate can be estimated by taking into account a stress concentration factor of $\simeq 3.14$ for an average creep cavity and a creep exponent for René N5(SX) of $n = 5.14$ [27].

$$\rho_s = \rho_m = \frac{\dot{\gamma}}{b v_c} = \frac{360 \cdot \sqrt{3} \cdot 6 \times 10^{-6}\ \text{/s}}{0.25 \times 10^{-9}\ \text{m} \cdot 4 \times 10^{-8}\ \text{m/s}} = 3.7 \times 10^{14}\ \text{/m}^2$$

This dislocation density is consistent with experimental measurements by Pollock and Field at 850 °C [27]. The associated stored energy per unit volume (E = $1/2\rho G b^2$) is 0.557 MJ/m^3, using $G \simeq 48.2$ GPa and by combining contributions from the SSDs and GNDs, the total stored energy is estimated to be 1.28 MJ/m^3.

3.1.2.3 Recrystallization Barrier

The barrier to the growth of a recrystallized nucleus is primarily due to the grain boundary pinning effect of the γ' phase, requiring dissolution. Dissolution of the γ' phase below the solvus temperature has an associated free energy penalty; an estimate of the free energy penalty for complex Ni-base superalloys can be determined by using computational thermodynamics. Thermo-Calc was used to determine the increase in the free energy of the system due to suppressing the γ' phase at 982 °C for a Ni-10.25 wt% Al alloy and for the complex superalloys used in this study [109]. Results indicate ΔG_D values of 694.4 MJ/m^3, 1370 MJ/m^3 and 1385 MJ/m^3 for Ni-10.25 wt% Al, GTD444(CG), and René N5(SX), respectively. A more significant barrier to the dissolution of the γ' phase is expected in the complex superalloys compared to Ni-Al binary alloy due to the presence of additional γ' forming elements such as Ta, Ti, and Nb, which may vary significantly due to local solidification-induced variation in alloy composition. The calculated ΔG_D values are between two and three orders of magnitude larger than the stored energy of 1.28 MJ/m^3.

However, complete dissolution of the γ' phase in the nucleus may not be necessary as reprecipitation occurs discontinuously, allowing diffusion of solute along the boundary of the recrystallized grain from precipitates in the deformed matrix to discontinuous precipitates in the recrystallized grain, effectively reducing the barrier to recrystallization [98, 110]. In Ni-Al alloys, the diffusion coefficient of Al through moving boundaries has been measured to be three orders of magnitude higher than through stationary boundaries

[111]. Even for Re, an element with extremely low bulk diffusivity, the diffusivity through a boundary was observed to be approximately four orders of magnitude higher than its lattice diffusivity [112]. It is hypothesized that the stored energy overcomes the local recrystallization barriers with the aid of boundary diffusion. This allows dynamic recrystallization to occur during creep, as is observed experimentally.

3.1.2.4 Discussion of Relevant Literature

Dynamic recrystallization during creep was first observed by Hirst and later by Gifkins in single crystals of lead [113, 114]. The strain rates associated with dynamic recrystallization during creep were shown to be cyclic with rapid increases upon recrystallization due to primary creep of the new grains. Besides lead, dynamic recrystallization has been observed during high temperature deformation of a number of pure and lightly alloyed FCC metals [115]. At high temperatures (> 0.75 T_m), the nucleation of dynamic recrystallization in single crystals of copper is believed to be associated with fluctuations in the subgrain size distribution during rearrangement processes and subsequent discontinuous subgrain growth [115, 116]. It has also been suggested that dynamic recrystallization during creep of polycrystalline copper may occur locally and in small volumes so that the creep behavior is affected only gradually, rather than discontinuously as in single crystals [116].

It is important to note that a majority of previous studies on dynamic recrystallization during creep have involved the use of pure and dilute single phase alloys, whereas in this research, Ni-base superalloys, which contain many alloying elements and several different phases, have been investigated. However, there have been a number of previous studies on static recrystallization in DS Ni-base superalloys similar to those investigated here [100, 117–122]. Indentation, cold working, or shot peening are commonly used to induce surface damage, followed by a subsequent heat treatment to promote recrystallization at the surface. The most commonly observed boundary particle interaction reported is type (1) and is often described as cellular recrystallization with additional nucleation events occurring ahead of the moving interface [100, 117, 121, 122]. Of particular relevance to the current study is the work by Bürgel, *et al.*, where interrupted creep testing of CMSX-6 to 15% strain at 760 °C and 980 °C was used to further investigate the nucleation of the recrystallized grains in the γ/γ' microstructure [117]. As a result of the creep deformation, cracks formed around casting pores and, after annealing at 980 °C, recrystallization was observed at the crack tips due to the high amount of local plastic deformation. It is unclear in the work of Bürgel, *et al.*, if recrystallization was also observed before the annealing treatment.

Localized recrystallization has also been observed during TMF up to 1000 °C by Moverare, *et al.*, within bands of localized deformation near fatigue cracks [123]. The intersection of deformation-induced twins was believed to be the primary nucleation point for the recrystallization process. Dynamic recrystallization located at the specimen surface has been reported during creep between 800 °C and 900 °C for up to 1000 h [124]. Surface recrystallization during creep testing is generally a result of the formation of a γ' depleted zone near the specimen surface due to oxidation and residual stress from machining.

3.1.2.5 Dynamic Recrystallization and Mechanical Behavior

The presence of recrystallized grains is expected to significantly reduce fatigue and creep life, especially for thin walled gas turbine engine components. Literature on the effect of recrystallization on mechanical properties of Ni-base superalloys is limited to surface recrystallization, where a thin layer of cellular recrystallization was found to cause a higher crack density during low-cycle fatigue and, due to the presence of grain boundaries normal to the stress axis, had a higher creep rate than that of virgin specimens [117, 125]. Dynamic recrystallization that occurs internally could be a contributing factor to the increasing creep rate during tertiary creep in directionally solidified Ni-base superalloys. To assess the extent to which localized dynamic recrystallization could contribute to the acceleration of creep, a model for the creep rate based on the Cocks and Ashby model of void growth is developed [126, 127].

3.1.3 A Model for Recrystallization-Accelerated Tertiary Creep

In general, creep rupture occurs by the growth and coalescence of voids on grain boundaries. However, in the CG and SX alloys used in this study, transverse boundaries have been removed to improve material properties, causing the void growth to be controlled by power-law creep of the surrounding material rather than a boundary or surface diffusion process. In the Cocks and Ashby model, a bound theorem is used to produce approximate analytical expressions for the void-growth rates and creep rates (Equation 3.3) of a cylindrical element of material centered on a void, shown schematically in Figure 3.12a [126, 127]. Region 1 creeps at a rate equal to the minimum or steady state creep rate, $\dot{\epsilon}_0$, while region 2, occupying a fraction of the cylinder described by $2r_v/d$, creeps faster by a factor of $1/(1-f_v)^n$ because the stress acting on this material is greater due to the presence of a void [126, 127].

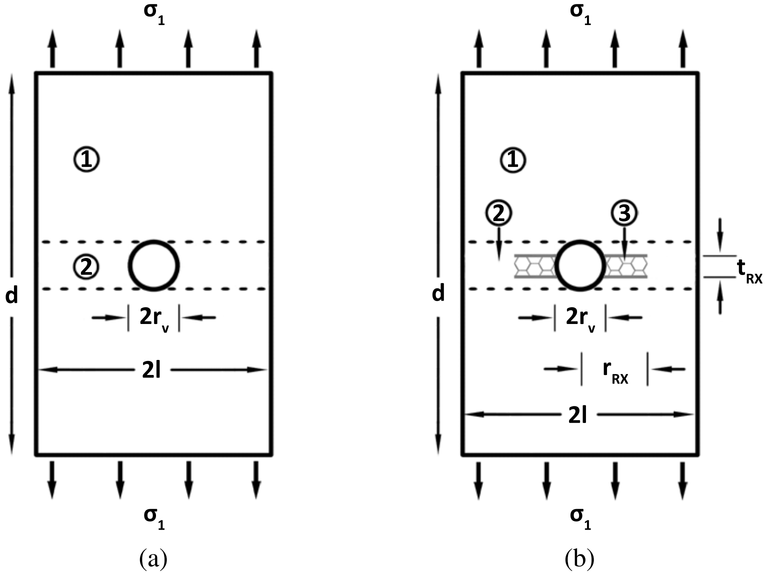

(a) (b)

Figure 3.12: Schematics showing a) the basic framework for the Cocks and Ashby model and b) the modified model. Region 1 is a solid volume of material and region 2 contains a spherical void that causes a reduction in load bearing cross-sectional area, increasing the stress on the surrounding material. Region 3 contains recrystallized grains.

$$\frac{\mathrm{d}\epsilon}{\mathrm{d}t} = \dot{\epsilon}_0 \left\{ 1 + \frac{2r_v}{d}\beta\left[\frac{1}{(1-f_v)^n} - 1\right]\right\} \tag{3.3}$$

Here, $\mathrm{d}\epsilon/\mathrm{d}t$ is the axial strain rate, r_v is the radius of the void, d is the distance between voids along the tensile axis, f_v is the fraction of voids in region 2 ($f_v = {r_v}^2/l^2$), $2l$ is the void spacing perpendicular to the tensile axis, n is the creep exponent, and β takes into account the stress triaxiality due to the stress state and, for simple tension, is $\simeq 0.6$.

To account for recrystallization, an annular ring of softened material is considered as shown in region 3 in Figure 3.12b. Additional terms have been added to Equation 3.3 to take into account the fraction of recrystallized grains contained in region 2, f_{RX}, and for the creep rate of the recrystallized material, $\dot{\epsilon}_0^{RX}$, which is expected to be approximately equal to the creep rate of a polycrystalline Ni-base superalloy; this yields Equation 3.4. It is worth noting that the model takes into account the experimental observation that the presence of voids are critical to the nucleation and growth of recrystallized grains by assuming that at $f_v = 0$ the axial strain rate will always be equal to the steady state value.

$$\begin{aligned}\frac{\mathrm{d}\epsilon}{\mathrm{d}t} = \dot{\epsilon}_0 \left\{1 + \frac{2r_v}{d}\beta\left[(1 - f_{RX})\left(\frac{1}{(1 - f_v)^n} - 1\right)\right]\right\} \\ + \dot{\epsilon}_0^{RX}\frac{2r_v}{d}\beta\left[f_{RX}\left(\frac{1}{(1 - f_v)^n} - 1\right)\right] \qquad (3.4)\end{aligned}$$

For simplicity, void growth by surface or boundary diffusion is assumed to be negligible. Creep transients were not included in the model to provide the most conservative comparison with experimental results. Assuming a homogeneous distribution of spherical voids, $2r_v = d$, the creep rate has been plotted for various f_{RX} values, where $f_{RX} = ((r_{RX} - r_v)^2/l^2) * (t_{RX}/2r_v)$, in Figure 3.13. A minimum creep rate, $\dot{\epsilon}_0$, of 2.22×10^{-8} /s was used along with $\dot{\epsilon}_0^{RX} = 2 \times 10^{-7}$ /s.

The creep rate of the recrystallized material was estimated from the Mar-M200 deformation mechanism map [128]. The grain size of the Mar-M200 material was 100 μm while the observed recrystallized grains were ~1 μm making the used $\dot{\epsilon}_0^{RX}$ a conservative estimate. It is worth noting that, at the creep conditions used in this study, pure Ni with a 1

μm grain size creeps at a rate of 1 /s, providing an upper bound [128].

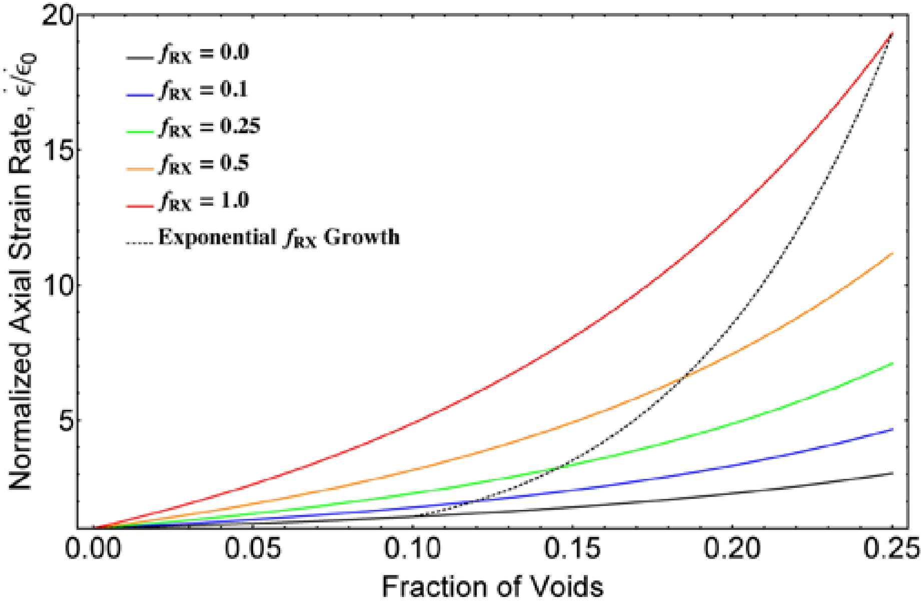

Figure 3.13: Plot of the modified Cocks and Ashby model assuming a homogenous distribution of spherical voids. The solid lines assume a constant volume fraction of recrystallized grains until rupture, while the dashed line uses a nucleation criterion and assumes exponential growth until $f_{RX} = 1$. The axial strain rate has been normalized by the minimum creep rate, $\dot{\epsilon}_0$.

If the voids are instead assumed to be inhomogenous, $2r_v < d$, the increase in strain rate would be less significant. In the above analysis a constant volume fraction of recrystallized material was assumed; the dashed line in Figure 3.13 uses an assumed nucleation criterion for recrystallization of $f_v = 0.1$ and assumed exponential growth until $f_{RX} = 1$. A failure criterion of $f_h = 0.25$ is used in accordance with the original Cocks and Ashby model [127]. The analytical model indicates that the axial strain rate increases by approximately one order of magnitude from the onset of recrystallization to rupture, comparing favorably to the experimentally observed phenomenon of approximately one order of magnitude increase in creep rate from 180 h to rupture in Figure 3.1a. This supports the assertion that dynamic recrystallization contributes to the tertiary creep behavior of directionally solidified Ni-base superalloys. The predicted increase in creep rate is strongly influenced by the value of $\dot{\epsilon}_0^{RX}$ which, in this model, has been conservatively estimated. Increasing $\dot{\epsilon}_0^{RX}$ by two orders of magnitude, where a nucleation criterion and exponential growth are again assumed, results in an increase of 1800 times the axial strain rate at rupture, compared to the 20 fold increase when $\dot{\epsilon}_0^{RX} = 2 \times 10^{-7}$ /s, as shown in Figure 3.14.

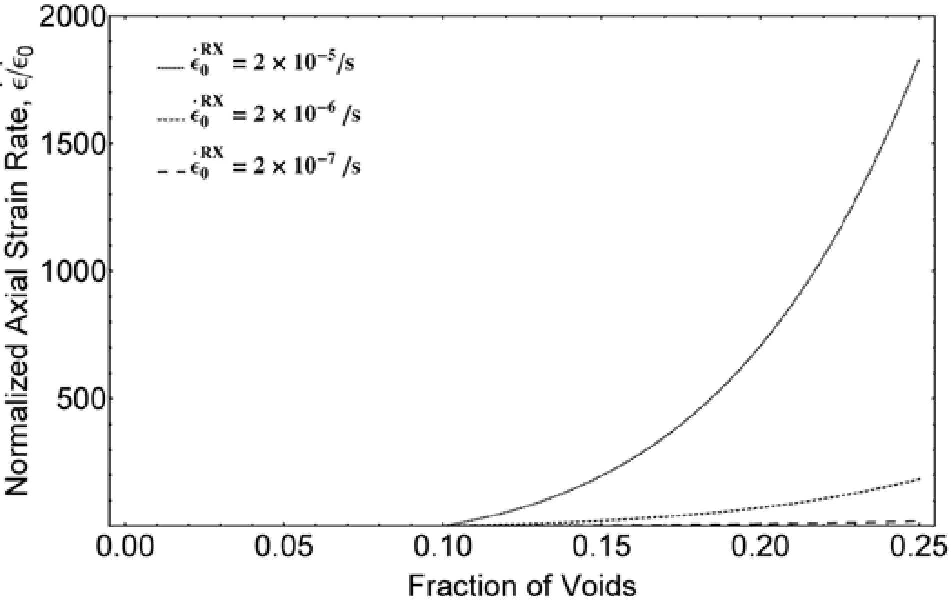

Figure 3.14: Plot showing the effect of increasing the creep rate of the recrystallized material. The same nucleation criterion and exponential growth are assumed for all curves, and the axial strain rate has been normalized.

3.1.4 Summary of Creep Damage

Creep damage in directionally solidified Ni-base superalloys initially consists of an increasing dislocation density in the γ phase, and the formation of nodal networks that relax the misfit between the γ matrix and γ' precipitates. Rafts of the γ' precipitates form during high temperature testing and coarsen over time. Shearing of the γ' precipitates begins after the local stresses reach sufficient levels in the tertiary creep regime. Cavitation and crack formation, while limited in advanced DS alloys due to the elimination of transverse grain boundaries, does occur at high levels of creep strain (> 10%) at carbides and solidification porosity. Additionally, localized dynamic recrystallization has been observed in CG and SX Ni-base superalloys as early as 20% creep strain.

Dynamic recrystallization during creep testing of GTD444(CG) and René N5(SX) is expected to occur first at a critical defect in the specimen, such as a large void, a cluster of carbides, or a combination of both. The initial recrystallization event is difficult to locate with traditional 2-D sections and thus determining the creep strain at which recrystallization first occurs requires large-scale 3-D analyses of crept specimens. The lack of previously published observations of dynamic recrystallization in these alloys may be a result of the difficulty in observing the recrystallized grains. With an average grain size of ~1 μm and the high degree of damage induced in the specimens, observation via optical microscopy is not feasible and electron microscopy leads to inconclusive results, which can only be confirmed by using recently available high resolution EBSD techniques. Analytical calculations of the stored energy due to deformation indicate an insufficient driving force near carbides and creep cavities to overcome the barrier of dissolving γ' precipitates below the γ' solvus temperature for a Ni-10.25 wt% Al alloy, GTD444(CG), and René N5(SX). This indicates that complete dissolution of the γ' precipitates is not necessary and boundary diffusion of solute aids in the discontinuous reprecipitation of γ' in the recrystallized grain. A model for recrystallization-accelerated tertiary creep shows comparable behavior to the experimental creep rate versus time curve, indicating that dynamic recrystallization is a significant contributor to the increasing creep rate during tertiary creep. It is hypothesized that dynamic recrystallization is a fundamental part of creep in the high temperature and low stress creep regime.

3.2 Sustained Peak Low-Cycle Fatigue (SPLCF)

Besides creep, fatigue loading also causes damage to turbine blades during operation that must to characterized in order to develop an appropriate repair procedure. Specifically, SPLCF (compressive-hold fatigue) cycling often limits the performance of aviation and land-based gas turbines [50]. Depending on the testing conditions, SPLCF tests have been shown to reduce fatigue life by up to a factor of 100x when compared to tests without a compressive hold [54]. This illustrates the importance of oxidation and creep relaxation on the progression of damage. Failure during SPLCF testing is a result of surface initiated cracks that oxidize and progressively grow through coatings into the superalloy substrate. Models of this process have been developed by Evans, *et al.* and have been discussed previously in Section 1.3.2 [51]. SPLCF testing in this thesis work will be limited to uncoated René N5(SX) specimens. The primary factors that influence the rate of crack growth in an uncoated specimen are the oxide growth stress (a result of oxidation on the transverse grain boundaries of the thermally grown oxide (TGO)) and the yield strengths of both the superalloy substrate and TGO [54].

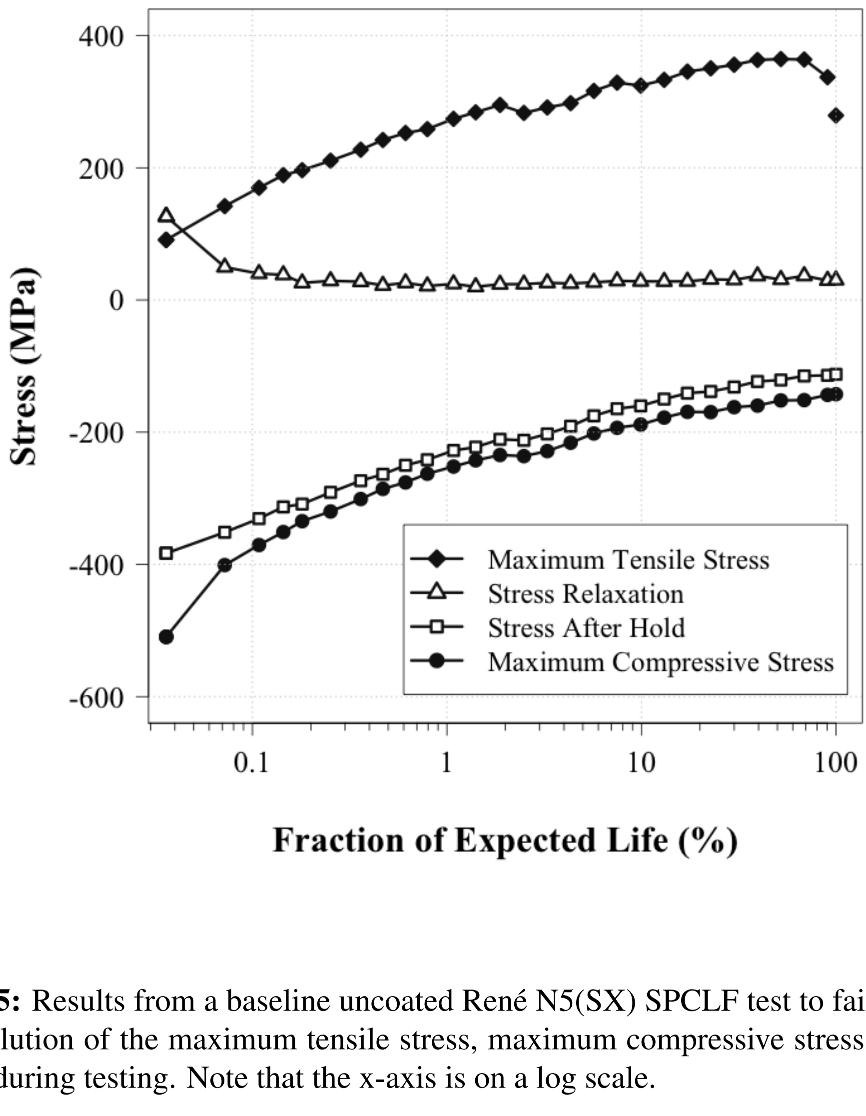

Figure 3.15: Results from a baseline uncoated René N5(SX) SPCLF test to failure, showing the evolution of the maximum tensile stress, maximum compressive stress, and stress relaxation during testing. Note that the x-axis is on a log scale.

A representative SPLCF test to failure of an uncoated René N5(SX) specimen showed, as expected, an evolution of the maximum stress, minimum stress, and, during the hold period, stress relaxation as the number of cycles increased, as shown in Figure 3.15. From the first cycle creep relaxation value of ~130 MPa, a steady-state value of ~26 MPa was reached after the first 1% of expected life. First cycle and half-life hysteresis loops, shown in Figure 3.16, further illustrate the extensive stress relaxation that occurs during testing.

The increase in maximum tensile stress over time is due to creep relaxation, and because SPLCF tests are performed in strain control, once a significant level of damage has been reached the maximum tensile stress decreases until the specimen fails/ruptures, as shown in Figure 3.17. Refer to Section 2.2 for additional details on the SPLCF testing procedure.

3.2.1 Oxidation Assisted Fatigue Cracks

The most obvious form of damage during dwell fatigue is the formation and growth of surface cracks via cyclic plasticity that are oriented perpendicular to the stress axis and after growing to a critical depth transition into macroscopic long cracks [50]. Assuming a long crack threshold of ΔK_{th} = 7 MPa $\cdot$ m$^{1/2}$ and using a maximum tensile stress of 370 MPa, consistent with the SPLCF testing conditions used in this study, the transition will occur at 114 μm. Prior to the transition to long crack behavior, oxidation and creep are primarily responsible for crack growth. Cracks forming during SPLCF are filled with α-Al_2O_3 TGOs, as shown in Figure 3.19, and the effective growth of the TGO during testing causes initial crack growth [51]. The growth of the TGO is accommodated by substrate

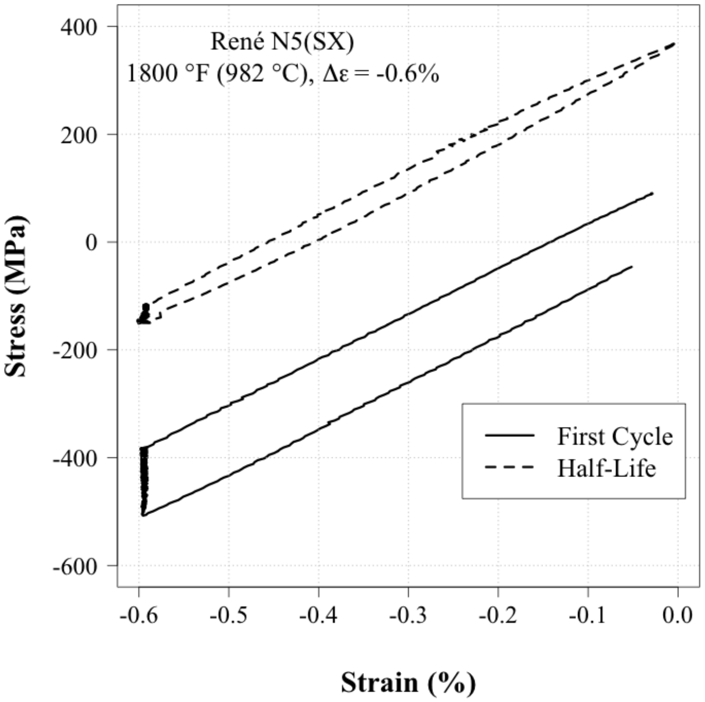

Figure 3.16: Hysteresis loops from the first cycle and half-life of an uncoated René N5(SX) SPLCF test. Testing was performed at a constant temperature of 982 °C in air with a strain range of 0.6% and R = -∞ (A = -1.0). The vertical segments at -0.6% strain for both hysteresis loops correspond to the hold period in the SPLCF cycle, where significant stress relaxation occurs.

creep around the crack tip. The crack spacing measurements collected from interrupted and failed specimens are summarized in Table 3.1 and shown graphically in Figure 3.18. Crack spacing and length measurements indicate that specimens exposed to more SPLCF cycles had more cracks (smaller average crack spacing) and a larger average crack depth, as expected. The average crack length for a specimen interrupted at 50% of expected life was 27.1 μm. The average SPLCF crack was oriented perpendicular to the loading axis and rafting occurred parallel to the load direction due to the applied compressive load and

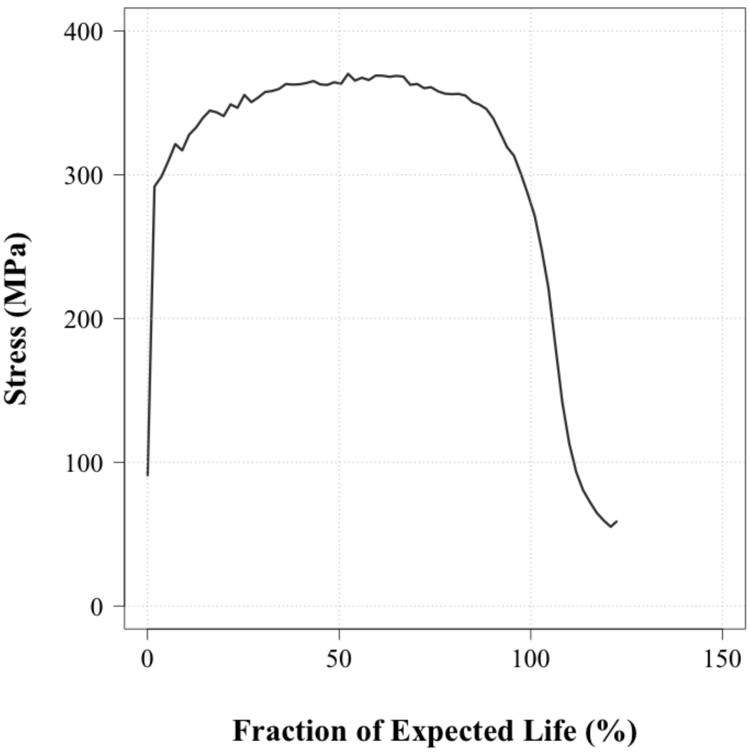

Figure 3.17: Plot of maximum stress versus fraction of expected life until the test was discontinued. Failure was defined at a 25% load drop from the maximum stabilized value.

the negative misfit of René N5(SX) (Figure 3.19).

Rafting has been shown to be beneficial to fatigue life when the rafting direction is perpendicular to the crack growth direction [129]. This is due to the presence of long vertical γ/γ' interfaces that act as a barrier to crack propagation when compared to a cuboidal microstructure where cracks are easily able to open along the γ channels between γ' precipitates. The fatigue tests conducted in literature to determine the influence of rafting do not include a hold period and thus are exposed to elevated temperature (950 °C or 1050 °C) for only several hours, while the specimen tested via SPLCF to failure lasted hundreds of

Table 3.1: Sustained peak low-cycle fatigue crack measurements collected from René N5(SX) specimens interrupted at various fractions of expected life and tested to failure. N is the number of fatigue cycles tested and N_f is the number of cycles to failure (based on one test).

N/N_f	N	Avg. Spacing (μm)	Avg. Length (μm)	Max. Length (μm)
0.1	337	1440.0	8.8	18.0
0.2	672	1433.2	15.5	38.0
0.3	1007	1151.8	15.7	48.0
0.5	1696	527.0	27.1	91.0
0.75	2691	123.3	27.6	494.0
1	3350	212.6	100.3	1299.0

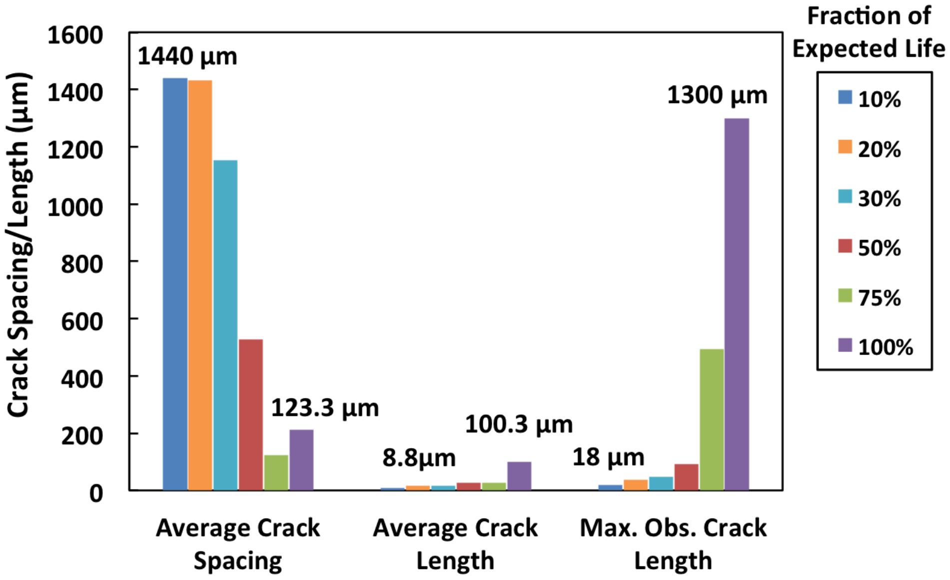

Figure 3.18: Bar chart displaying the change in the average crack spacing, average crack length, and maximum observed crack length until specimen rupture.

hours. Oxidation plays a much more important role during SPLCF testing, and the dissolution of the γ' due to Al depletion near atmosphere-exposed cracks is expected to minimize the influence of the rafted morphology on the crack growth rate.

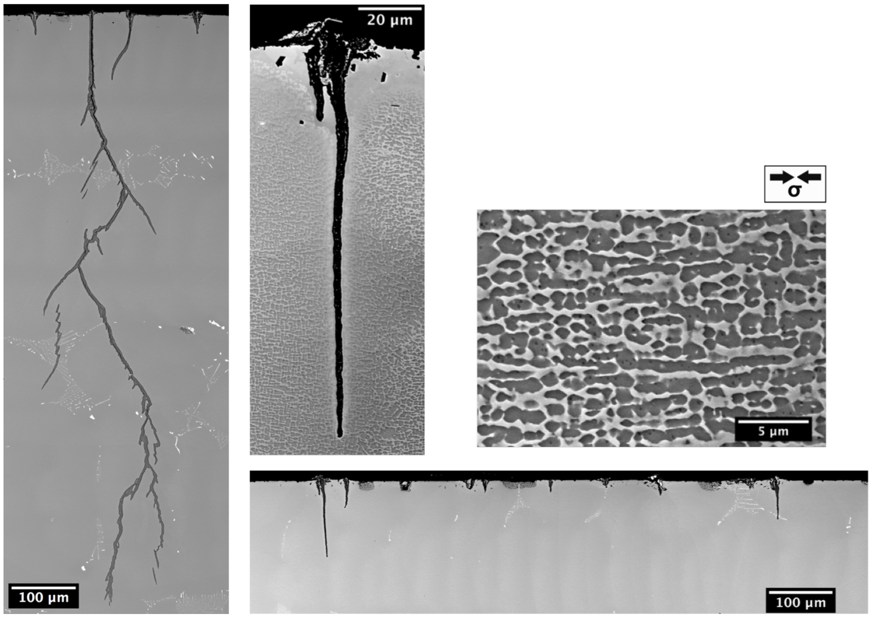

Figure 3.19: Representative micrographs of an uncoated René N5(SX) SPLCF specimen tested to failure showing rafting (directional coarsening) and oxidation-assisted crack growth.

Using the detailed examination of both creep and fatigue damage presented and discussed in this chapter, a rejuvenation procedure can now be designed to repair the primary forms of damage.

Chapter 4

Design of a Rejuvenation Procedure

This chapter will outline a repair procedure designed to remove the damage observed in René N5(SX) and GTD444(CG) superalloy specimens subjected to interrupted creep or fatigue testing. Additionally, results from exploratory rejuvenation heat treatments will be presented along with the multiple rejuvenation testing approach used to validate the repair procedure. The outcome of multiple rejuvenation testing protocols will be discussed in a subsequent chapter.

As mentioned in Section 3.1.4, the damage observed up to 5% strain during high temperature (982 °C) and low stress (172-206 MPa) creep consisted of an increase in the dislocation density and rafting of the γ' phase. A rejuvenation heat treatment is capable of reducing the dislocation density by recovery and dissolving the γ' rafts into solution. Re-precipitation of cuboidal γ' precipitates will occur during cooling from the rejuvenation heat treatment temperature. Consequently, it is proposed that in order to recover the virgin creep properties and extend creep life, only a rejuvenation heat treatment will be required if < 5% creep strain has been accumulated.

4.1 Rejuvenation Heat Treatment - Creep

To test the effectiveness of a rejuvenation heat treatment in restoring the original microstructure at various solution temperatures and creep strain levels, initial heat treatment studies were performed on coupons cut from creep specimens of GTD444(CG) and René N5(SX) crept to 2% and 5% strain. Virgin coupons were also heat treated to determine the influence of strain on the dissolution, re-precipitation, and growth of the γ' phase. The heat treatment conditions are summarized in Table 2.1. Cooling and heating rates were chosen to meet typical industry specifications, and were performed in either vacuum or a 5% H_2/Ar reducing atmosphere. Representative micrographs for each alloy after heat treatment are shown in Figures 4.1 through 4.4.

As the solution temperature was decreased from the γ' solvus, the volume fraction of unsolutioned phases in GTD444(CG) increased regardless of initial condition, as shown in Figure 4.1. Similar results were observed for heat treated René N5(SX) coupons. When examining the γ' morphology in the dendrite core regions, the lowest solution temperature used for GTD444(CG) of 28 °C below the γ' solvus was unable to dissolve all of the rafted precipitates, Figure 4.2a. Thus, of the solution temperatures used in this study, the minimum temperature capable of at least partially recovering the initial γ' morphology for GTD444(CG) is 14 °C below the γ' solvus. For René N5(SX) the rafted structure was successfully eliminated at solution temperatures equal to and above 56 °C below the γ' solvus. After aging, the γ' size has increased and a cuboidal morphology is achieved for both alloys, see Figures 4.3 and 4.4. It is worth nothing that as the solution temperature is decreased, the γ' morphology becomes less cuboidal; this is especially evident in GTD444(CG).

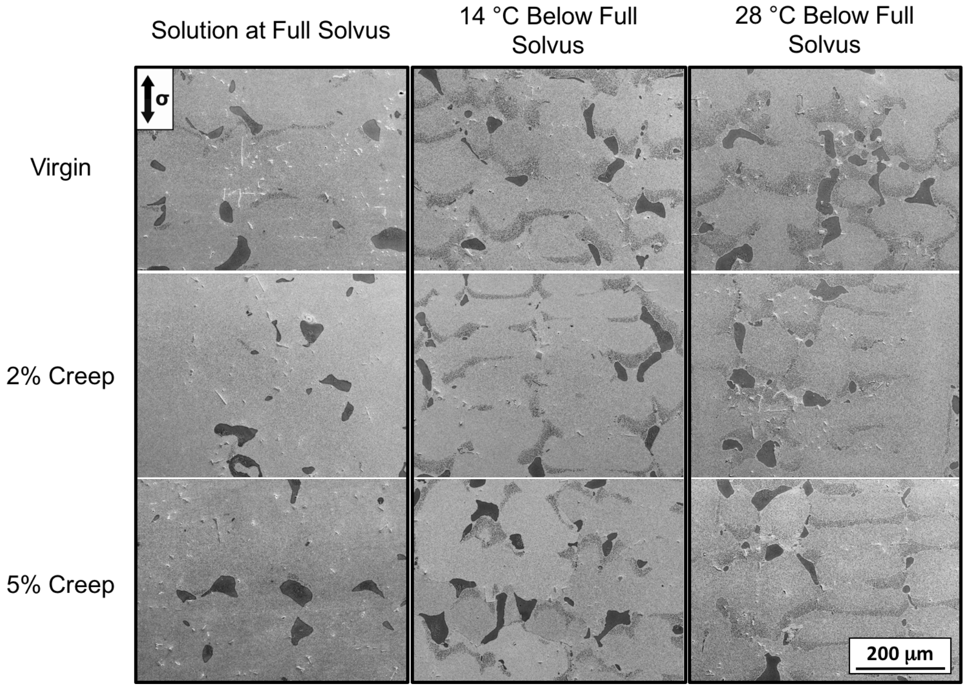

Figure 4.1: Low magnification micrographs collected from solution treated coupons of GTD444(CG). Notice the volume fraction of unsolutioned phases increases as the solution temperature is decreased from the γ' solvus. All solution heat treatments were held at temperature for 2 hours.

The primary goal of the rejuvenation heat treatments is to restore the initial microstructure and promote recovery while avoiding recrystallization. As shown in Figures 4.1 through 4.4, the rafted microstructure can be removed and the initial gamma prime morphology restored by rejuvenation heat treatment near the γ' solvus temperature and subsequent aging. However, surface recrystallization occurred during the rejuvenation heat treatment in the 5% creep strain coupon. As the solution temperature is decreased, the volume fraction of unsolutioned γ' increases but recrystallization is not observed at 5%

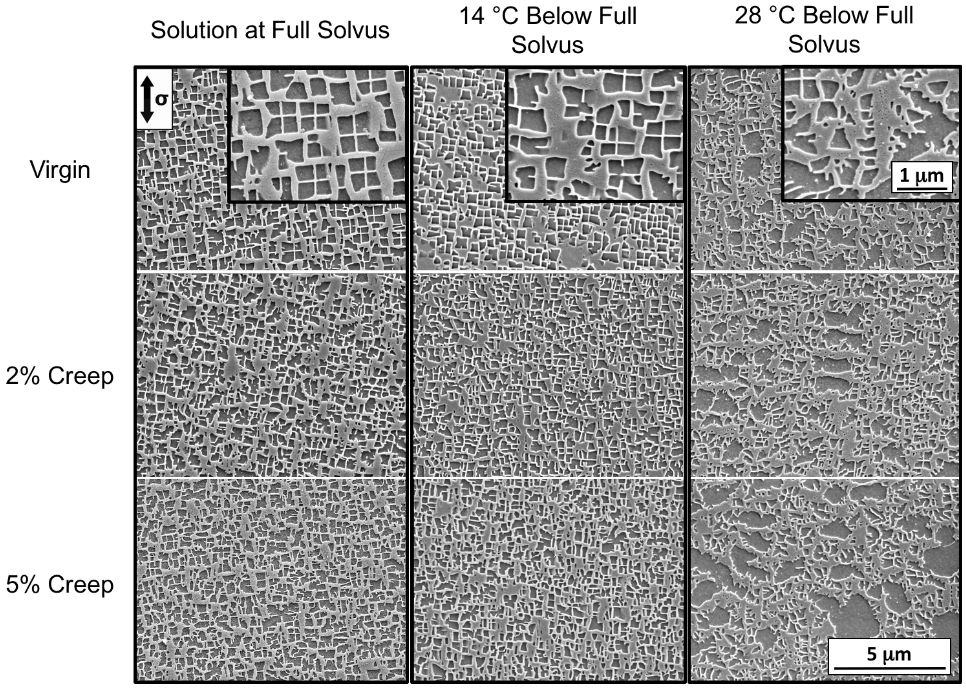

Figure 4.2: High magnification micrographs collected from the dendrite core regions of solution treated coupons of GTD444(CG). Solution heat treatments were held at temperature for 2 hours. Dissolution of the γ' phase did not occur in dendrite core regions at a solution temperature 28 °C below the γ' solvus temperature.

creep strain. The unsolutioned γ' is primarily located in the interdendritic region where the local γ' solvus is higher due to solidification induced segregation of γ' forming elements Al, Nb, Ta, and Ti [10]. The presence of unsolutioned γ' is expected to degrade creep performance by an increase in γ channel width and corresponding decrease of the Orowan stress due to precipitate coarsening during heat treatment [130]. The retention of misfit dislocation networks in unsolutioned areas may also increase creep rates when compared to virgin material by serving as dislocation sources [27].

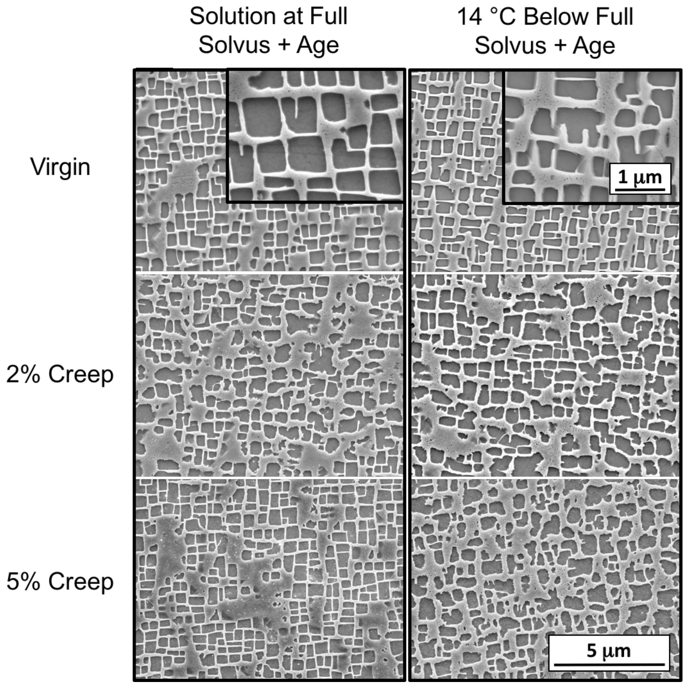

Figure 4.3: A comparison of the resulting microstructure after a solution + age heat treatment of GTD444(CG). Images were collected from the dendrite core regions of the microstructure.

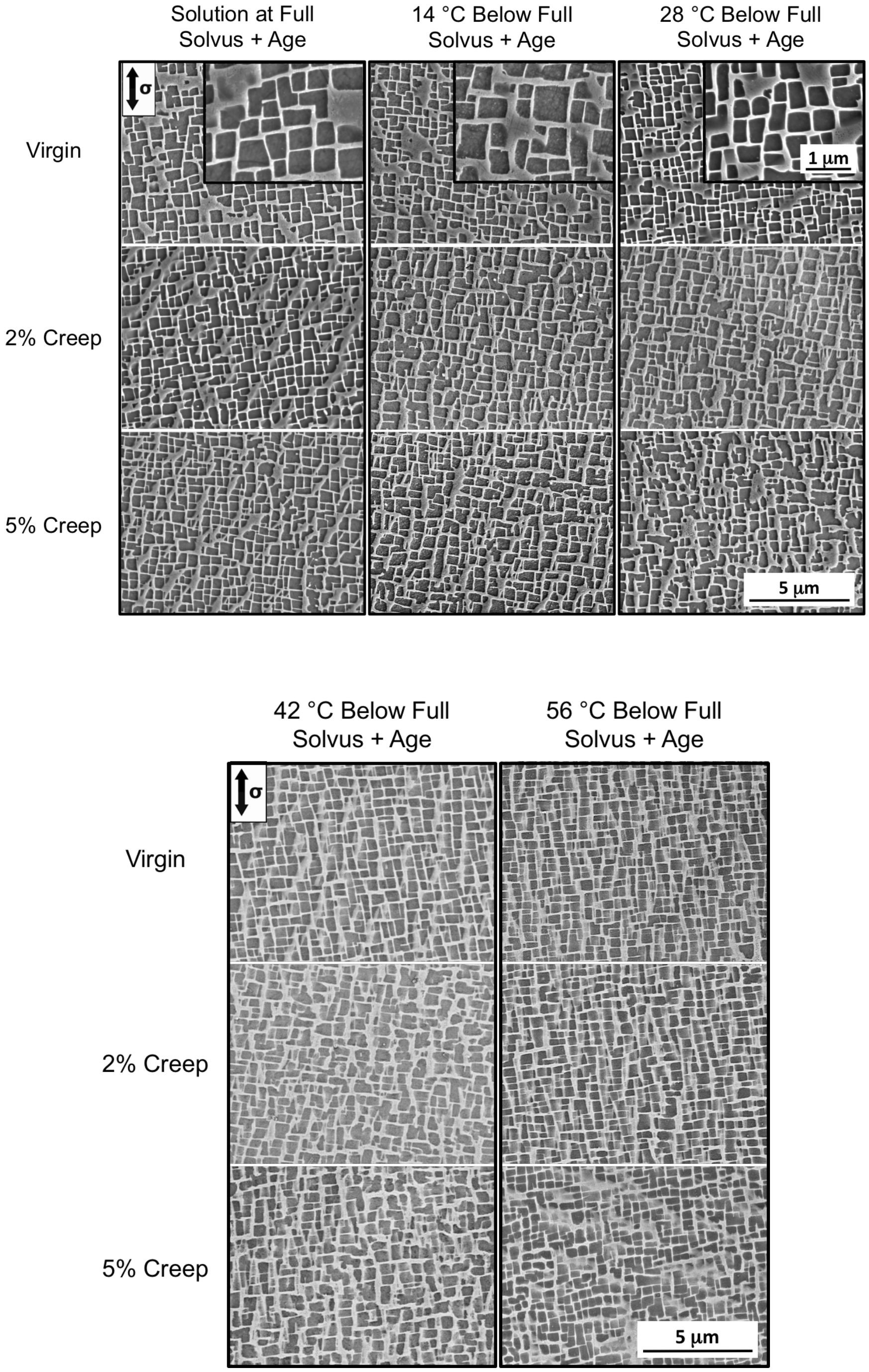

Figure 4.4: Micrographs of the René N5(SX) microstructure after a solution + age heat treatment at various creep strains and solution temperatures. Images were collected from the dendrite core regions of the microstructure.

As discussed in Section 1.4.1, recovery is necessary for the nucleation of recrystallized grains, thus avoiding recrystallization may not be possible. However, the initial heat treatments indicate that recrystallization has been avoided up to 5% creep strain for solution heat treatments below the γ' solvus temperature. This indicates that recrystallization in DS Ni-base superalloys may be inherently difficult due to the dislocation substructure formed under the influence of a large volume fraction of misfitting γ' precipitates and the pinning effect of the γ' precipitates as discussed in Sections 3.1.2.1 and 3.1.2.3.

4.1.1 Discussion of Relevant Literature

Investigations of the annealing/solution temperature limits and strain limits of recrystallization have been performed in literature by Cox, *et al.*, and Bürgel, *et al.* [118, 131]. Cox, *et al.* performed tensile tests at 950 °C and 1025 °C with a strain rate of $4{\times}10^{-4}$ s^{-1} to 4% plastic strain and then conducted annealing treatments at various temperatures for 6 h. Recrystallization was not observed following annealing at 1260 °C (55 °C below the γ' solvus) and below for specimens deformed at 950 °C, while recrystallization was observed at all annealing temperatures for specimens deformed at 1025 °C. Bürgel, *et al.* used room temperature axial compression tests to induce plastic strain and determined for a variety of Ni-base superalloys that solutioning above the γ' solvus after at least 1% strain caused rapid recrystallization [131]. Grain nucleation occurred at the surface and, at annealing temperatures below the γ' solvus, the grain boundary motion was hindered by interdendritic γ' precipitates. Prior studies are in good agreement with the coupon heat treatment results, namely suppression of recrystallization at solution temperatures below the γ' solvus at strains up to 4-5%.

4.1.2 Quantitative Microstructural Analysis

In order to quantify the microstructural differences due to mechanical testing and rejuvenation, moment invariants are used to characterize the γ' precipitate morphology. The moment invariants of interest are second-order and fourth-order moments that are invariant with respect to affine and similarity transformations. They are also central moments, meaning that each object has been translated so that the center of mass is located at the origin. Micrographs are first segmented using an algorithm that fills shapes based on an edge map before the moment invariants can be calculated. The segmentation process is outlined in Figure 4.5. Segmentation and the calculation of the moment invariants were performed in collaboration with Dr. Patrick Callahan of the University of California, Santa Barbara.

Moment invariants have been used previously in literature to successfully characterize 2D and 3D phase field generated precipitates and to characterize simulated rafted microstructures for Ni-Al alloys [132–134]. Equation 4.1 was used to calculate each object's moment invariaints at coordinates (x, y) with respect to the object's center of mass at coordinates (x_c, y_c). The order of the MIs, n, is equal to $p + q$.

$$\bar{\mu}_{pq} \equiv \iint_D dxdy(x - x_c)^p(y - y_c)^q. \tag{4.1}$$

Callahan, *et al.* generated second-order moment invariant maps to illustrate the 2D

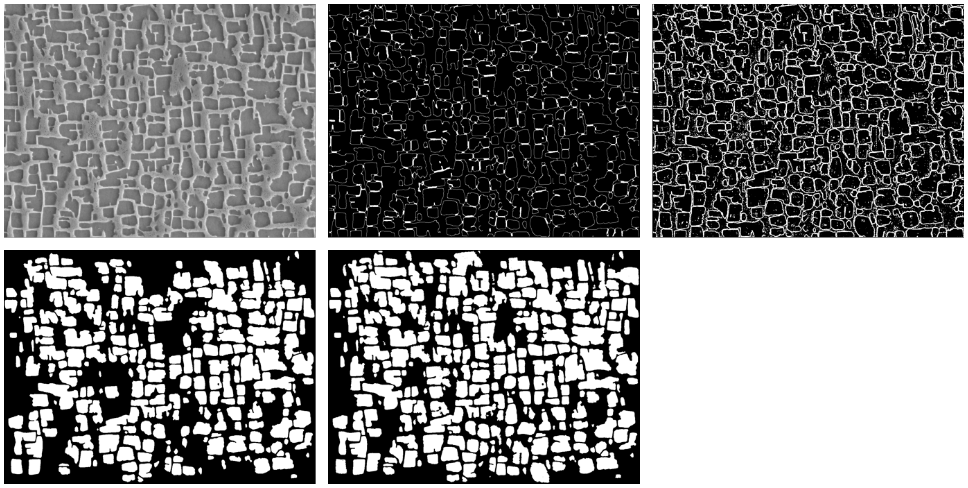

Figure 4.5: Representative images outlining the segmentation process that creates a binary image of white γ' precipitates and a black γ matrix for subsequent calculation of the moment invariants. From the original micrograph, edges are determined and the precipitates are filled. Manual adjustment is required in some situations to capture all of the γ' precipitates (with edge precipitates being ignored). Image courtesy of Dr. Patrick Callahan.

moment invariant space, as shown in Figure 4.6 [132]. The two second-order MIs used to generate this map are referred to as ω_1 and ω_2 (see Equations 4.2 and 4.3), respectively. The MIs have been normalized by a factor of the object's surface area, A = μ_{00}, so that 0 $\leq \omega_i \leq$ 1.

$$\omega_1 \equiv \frac{A^2}{2\pi(\bar{\mu}_{20} + \bar{\mu}_{02})}; \tag{4.2}$$

$$\omega_2 \equiv \frac{A^2}{16\pi^2(\bar{\mu}_{20}\bar{\mu}_{02} + \bar{\mu}_{11}^2)}. \tag{4.3}$$

Area weighted averages of the fourth order moments, τ_1, τ_2, and τ_3, were also calculated and are analogous to the kurtosis, which for the case of a 1D distribution describes the peakedness. The second order and fourth order moment invariants are listed in Table

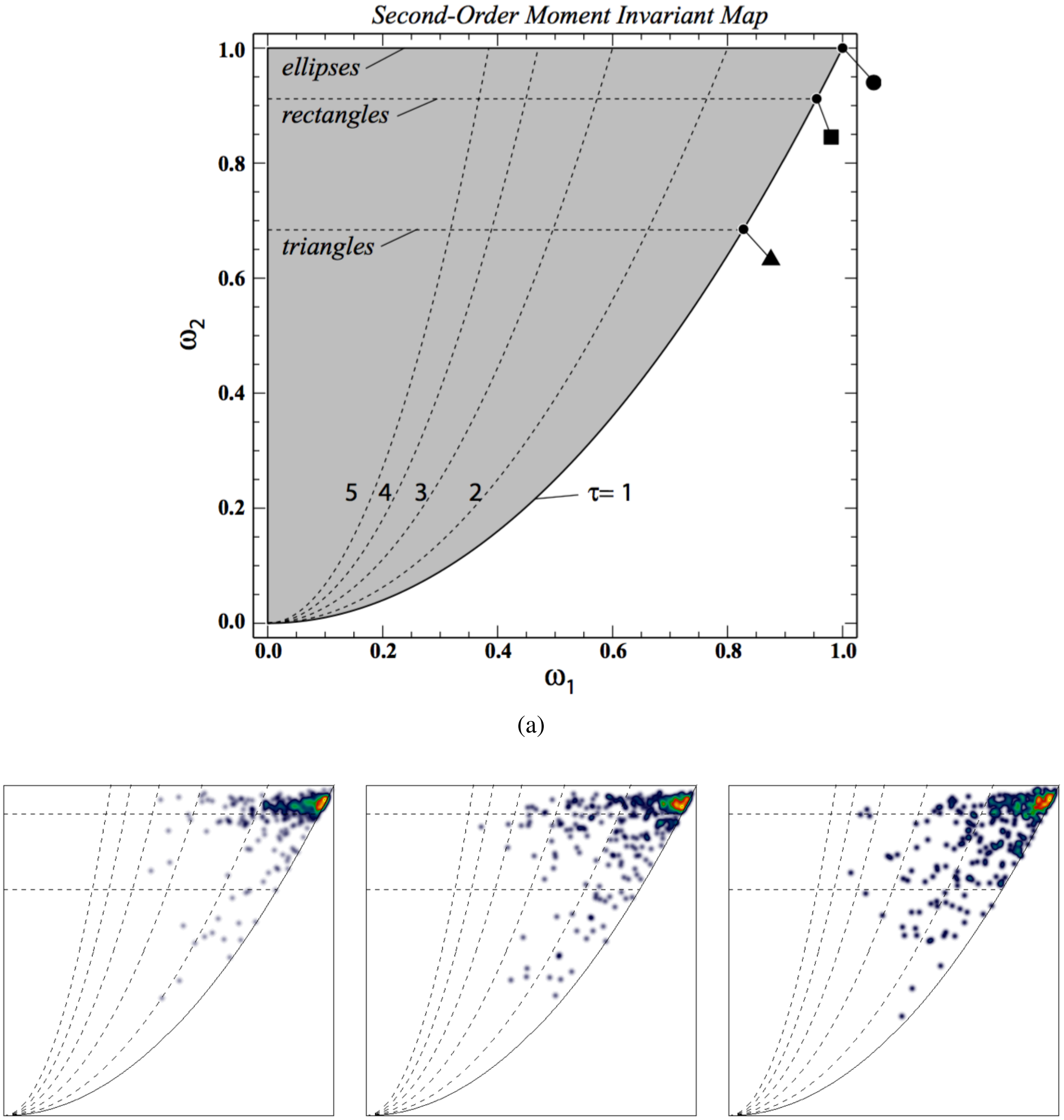

(a)

(b) (c) (d)

Figure 4.6: a) Map of normalized second-order moment invariants, ω_1 and ω_2. Both moment invariants are normalized by a factor of the surface so that $0 \leq \omega_i \leq 1$. The grey region indicates all possible shapes with the location of several common shapes indicated. τ is the aspect ratio of the shape's principal axes. Figures (b), (c), and (d) are the second order moment invariant maps collected from segmented micrographs of the virgin, 2%, and 5% creep strain coupons that were rejuvenated at 28 °C below the γ' solvus and aged. Unpublished and published original work by Callahan, *et al.* [132]. Images courtesy of Dr. Patrick Callahan.

4.1 for the coupon heat treatment studies performed. The precipitates used to calculate the moment invariants were from the dendritic core regions of René N5(SX) specimens. At solution temperatures greater than or equal to 14 °C below the γ' solvus, no trend was evident in the moment invariants as a function of prior creep strain. However, at solution temperatures less than and equal to 28 °C below the γ' solvus, all of the calculated second and fourth order moment invariants decreased as the prior creep strain increased. Thus, a more complex precipitate shape was present after heat treatments in specimens with higher levels of creep strain at lower solution temperatures when compared to the baseline 0%

Table 4.1: Table listing the second order (ω_1 and ω_2) and fourth order (τ_1, τ_2, and τ_3) moment invariants from micrographs of crept and subsequently heat treated René N5(SX) specimens. Coupon solution heat treatments were performed at either the full γ' solvus temperature or at a multiple of 14 °C below the full γ' solvus temperature with all specimens being aged at 1079 °C for 4 h.

Solution Temp.	Creep Strain (%)	ω_1	ω_2	τ_1	τ_2	τ_3
Full Solvus	0	0.851	0.854	0.675	0.639	0.638
	2	0.835	0.857	0.647	0.662	0.634
	5	0.843	0.858	0.659	0.649	0.634
-14 °C	0	0.843	0.865	0.666	0.666	0.658
	2	0.801	0.815	0.598	0.603	0.569
	5	0.802	0.836	0.601	0.626	0.600
-28 °C	0	0.839	0.862	0.658	0.664	0.667
	2	0.793	0.813	0.588	0.603	0.574
	5	0.772	0.797	0.550	0.570	0.522
-42 °C	0	0.852	0.874	0.685	0.697	0.682
	2	0.783	0.809	0.568	0.603	0.556
	5	0.763	0.798	0.547	0.589	0.547
-56 °C	0	0.825	0.871	0.642	0.685	0.683
	2	0.817	0.864	0.627	0.684	0.669
	5	0.762	0.798	0.546	0.584	0.543

strain coupon. If the average precipitate shape was a perfect square, the normalized moment invariants would have approximate values of 0.940 for ω_i and 0.800 for τ_i. As expected, the quantitative precipitate shape analysis indicated that at higher solution temperatures a rejuvenation heat treatment is more capable of recovering the microstructure to the baseline precipitate shape up to a creep strain of 5%.

4.2 Rejuvenation Heat Treatment and Material Removal - Fatigue

In addition to recovering creep properties, fatigue damage must also be addressed for complete repair of common service damage. As mentioned in Section 3.2, cracks form during SPLCF testing and are filled with α-Al_2O_3. Similar to creep testing, rafting of the γ' precipitates also occurs.

The unsuccessful attempts reported in the literature to rejuvenate fatigue properties, as discussed in Section 1.4.2, appear to be a direct result of the inability of simple rejuvenation heat treatments and even HIP (in the case of oxidized cracks) to remove the dominant form of damage, surface fatigue cracks. It was hypothesized that interrupting SPLCF tests at 50% of expected life and then grinding and polishing away material to a sufficient depth to remove any surface cracks present and applying a subsequent rejuvenation heat treatment should recover the fatigue properties.

Grinding and polishing of the fatigue specimens were performed with the specimens mounted in a drill press and followed standard procedures. A final polishing step of 3 μm diamond was used to minimize the influence of surface topography on the crack initiation process. Based on interrupted fatigue tests, Table 3.1, the average crack length for a specimen interrupted at 50% of expected life was 27.1 μm. However, in order to determine the appropriate machining depth, the maximum crack length of 91 μm is more relevant. Due to the fact that cracks initiate at the surface, their complete removal can be verified by optical microscopy. Successful recovery of fatigue properties will depend on the removal of the deepest surface cracks, because these cracks will most likely cause early failure upon retesting.

4.3 Defining a Rejuvenation Cycle

In order to determine the success of the repair procedures discussed in this chapter and to elucidate the processes that prevent successful rejuvenation, repeated rejuvenation cycles have been performed. A rejuvenation cycle includes rejuvenation heat treatment and/or small scale material removal, followed by creep or fatigue (SPLCF) testing, as presented schematically in Figure 4.7. Multiple rejuvenation testing is defined in this context as the application of repeated rejuvenation cycles until specimen failure. Prior to initial testing, the fatigue and creep specimens are polished to 3 μm diamond in order to remove surface damage caused by machining and heat treated at the same conditions as the rejuvenation heat treatment to establish a relevant mechanical behavior baseline.

Creep testing was repeatedly interrupted at various creep strain thresholds (2%, 3%, or 5%) to investigate the influence of strain, while SPLCF tests were only interrupted at 50% of expected life. Coated René N5(SX) specimens were also tested at a single creep strain threshold of 2%. Only one SPLCF threshold was used due to the ease of using non-destructive evaluation (visual surface inspection) to confirm the complete removal of fatigue cracks. Interrupting SPLCF tests at a higher or lower fraction of expected life would only change the amount of polishing required. These thresholds were chosen based on the observed damage in the interrupted testing discussed in Chapter 3, specifically the measured length of fatigue cracks during SPLCF testing and the absence of carbide cracking and growth of existing solidification pores during creep to 5% strain.

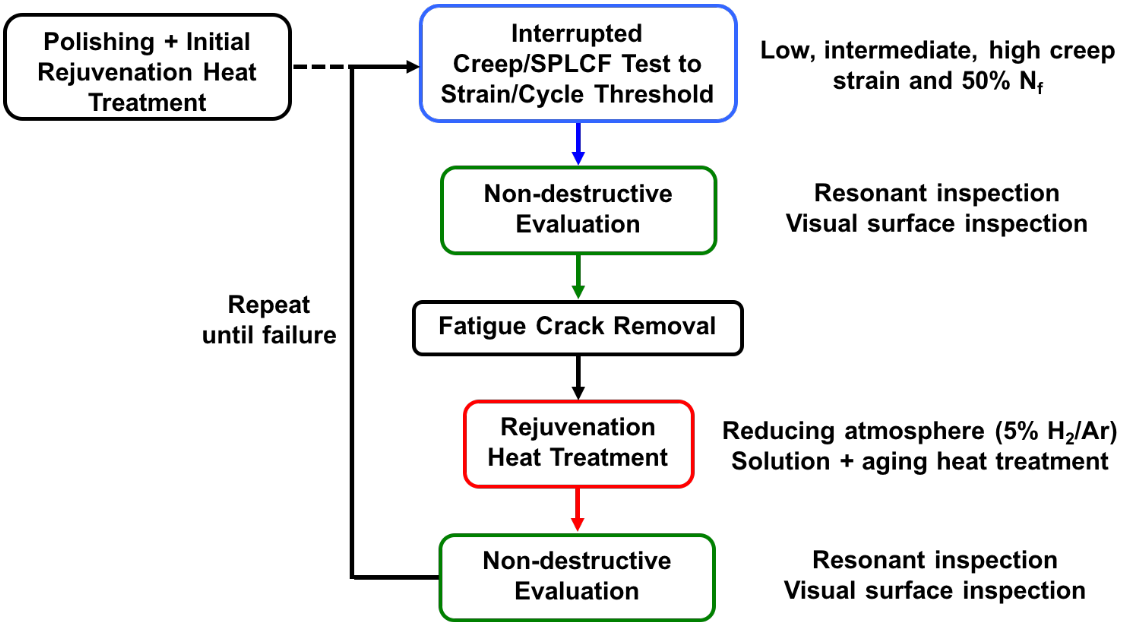

Figure 4.7: Schematic outlining the multiple rejuvenation testing procedure used for both GTD444(CG) and René N5(SX). The fatigue crack removal is only performed during multiple rejuvenation of SPLCF test specimens.

Non-destructive evaluation (NDE) techniques have been implemented in the multiple rejuvenation cycle after each rejuvenation heat treatment and mechanical test to investigate their usefulness in determining the presence of nonrecoverable damage. In this investigation, multiple rejuvenation cycles were conducted until failure, thus the only way to detect the presence and evolution of non-recoverable damage *in situ* is through the use of NDE. Non-recoverable damage includes recrystallization, cracks, and cavities, as mentioned in Section 1.4.4. Besides standard visual surface inspection to detect cracks, resonant ultrasound spectroscopy (RUS) will also be used. The fundamentals of RUS will be briefly introduced here and discussed further in Chapter 7.

Elastic solids have normal modes and natural resonant frequencies that depend on shape, size, and the elastic properties. If driven at a natural frequency, the amplitude of oscillation of the normal mode is enhanced by the quality factor (Q) of the sample, which is significant enough in superalloys to be measured experimentally [135]. RUS takes advantage of the dependence between elastic properties and resonant frequency to determine the elastic tensor of a material from the measured frequencies. Additionally, the resonant frequencies of a sample can be tracked through various processes, including rejuvenation heat treatment and mechanical testing, to detect a change in the elastic properties. Recrystallization of new grains with differing crystal orientations in DS specimens of GTD444(CG) and René N5(SX) will cause an increase in the elastic modulus of the specimen. This is due to the fact that the elastic modulus of Ni is at its lowest value along the [001] crystal growth direction, causing a corresponding increase in certain mode dependent resonant frequencies that can be measured through RUS. The growth of existing porosity and carbide cracking should theoretically result in a decrease in the elastic properties, due the creation of additional void space, but it will be difficult to isolate from the shape change effect which also causes a decrease in the resonant frequencies. Experiments have been performed to confirm the hypothesis that RUS can be used to non-destructively detect recrystallization and are presented in Chapter 7.

4.3.1 Rejuvenation Heat Treatment Parameters

Based on the coupon heat treatment results for GTD444(CG), a rejuvenation heat treatment solution temperature of 14 °C below the γ' solvus was used for multiple rejuvenation creep testing. At this temperature, restoration of the cuboidal γ' morphology occurs, however some of the original γ' precipitates remain in the interdendritic regions during the rejuvenation heat treatment.

For René N5(SX), solutioning was performed at the γ' solvus, 28 °C, and 42 °C below the γ' solvus. A range of solution temperatures was explored due to the overall higher γ' solvus, a result of the increased γ' solute content in René N5(SX) compared to GTD444(CG). The addition of Ta not only increases the γ' stability but also due to the strong tendency for Ta to segregate to the interdendritic regions of the microstructure will lead to an increase in the difference between the dendrite core and interdendritic γ' solvi [10].

The purpose of lowering the solution heat treatment temperature is to retain γ' precipitates in the interdendritic regions of the microstructure which, as discussed in Section 3.1.2.3, provide a substantial barrier to recrystallization. Recrystallization nuclei are expected to preferentially form in the interdendritic regions due to the presence of stress concentrators, such as carbides and solidification porosity; retained γ' precipitates in these regions can pin the recrystallization nuclei, suppressing their growth. Over time, recrystallization nuclei will also form in the dendrite cores and near the specimen surface aided by the depletion of γ' formers via oxidation, thus recrystallization is not expected to be suppressed indefinitely.

Each rejuvenation heat treatment possessed a 2 h hold at the solution temperature followed by a 4 h aging treatment at 1079 °C. The cooling rate from the solution temperature was consistent between all rejuvenation heat treatments and was chosen based on industrial standards. The success of applying each multiple rejuvenation cycle based on subsequent mechanical testing will be discussed in the next chapter for both GTD444(CG) and René N5(SX). Results from both creep and SPLCF mechanical tests will be analyzed with specific focus on answering the outstanding questions posed in Section 1.4.4.

Chapter 5

Life Extension via the Application of Multiple Rejuvenation Cycles

As discussed in Chapter 4, heat treatments of GTD444(CG) and René N5(SX) coupons illustrated the success of a subsolvus solution and aging rejuvenation heat treatment in restoring the initial cuboidal γ' microstructure in the dendritic regions of the microstructure. Additionally, it was believed that fatigue damage could be repaired by polishing away the fatigue cracks observed during interrupted SPLCF testing of René N5(SX) specimens (Section 3.2) and applying a rejuvenation heat treatment with the same parameters used for rejuvenating creep specimens. The multiple rejuvenation test conditions are summarized in Table 5.1 and, henceforth, each test will be referred to by the corresponding label. The results of applying repair procedures after performing creep and SPLCF mechanical tests as part of multiple rejuvenation testing will be detailed in this chapter.

Table 5.1: Table listing all of the multiple rejuvenation creep tests performed in this thesis work. Label convention: alloy type -°C below the γ' solvus or at the full solvus (FS) - creep strain threshold value (%) - coated (CT).

	Label	Solution Temp.	Creep Strain Threshold (%)
GTD444(CG)	444-14-1	-14 °C	1
	444-14-2a	-14 °C	2
	444-14-2b	-14 °C	2
	444-14-3	-14 °C	3
René N5(SX)	N5-FS-2	Full γ'Solvus	2
	N5-28-2	-28 °C	2
	N5-56-2	-56 °C	2
	N5-28-3	-28 °C	3
	N5-28-5	-28 °C	5
	N5-28-2-CT	-28 °C	2

5.1 Multiple Rejuvenation - Creep of René N5(SX)

Creep tests of René N5(SX) specimens were performed to the desired creep strain threshold (either 2%, 3%, or 5% strain) followed by a rejuvenation heat treatment, with NDE before and after each mechanical test and heat treatment. This defined one complete rejuvenation cycle, as outlined in Chapter 4, which was repeated until failure, thus indefinite rejuvenation was not observed. The rejuvenation heat treatments were applied to full, intact creep specimens and, to isolate the influence of the creep strain threshold, solutioning during rejuvenation heat treatments was only performed at a temperature of 28 °C below the γ' solvus. This solution temperature was chosen as a starting point, with the ultimate goal of supressing recrystallization, as discussed in Section 4.3.1, while also partially restoring the initial cuboidal γ' microstructure. All creep tests for René N5(SX) specimens were performed at 982 °C/206 MPa.

5.1.1 Influence of the Creep Strain Threshold

Creep curves from the multiple rejuvenation test N5-28-5 are shown in Figure 5.1 with each creep segment and rejuvenation heat treatment labeled. Three creep tests and two rejuvenation heat treatments were performed before specimen rupture occurred. The total creep life to failure of 305 h was lower than the baseline rupture life of 344 h. There was also a decrease in creep rupture ductility to 18% strain compared to the baseline of 35%. The time to 5% creep strain was reduced by 70% between the first (CT1) and second (CT2) creep tests, as shown in Figure 5.1b and listed in Table 5.2. Additionally, the minimum creep rate for the second creep test increased by a factor of 4 compared to first test. Thus, rejuvenating specimens after every 5% creep strain was not successful, leading to a lower total rupture life and an increased minimum creep rate. Due to unsuccessful rejuvenation, the third creep test (CT3) was not interrupted and the test continued until rupture.

Multiple rejuvenation tests at lower creep strain thresholds of 2% and 3% creep strain (tests N5-28-2 and N5-28-3) resulted in total creep lives of 952 h and 951 h, compared to the baseline of 344 h and creep rupture strains of 12% and 15%, respectively. At both 2% and 3% strain, after the first creep test (CT1) a decrease in creep performance was observed. This was evident in both the time to the creep strain threshold and in the minimum creep rate for the second creep test (CT2), as shown in Figure 5.2. However, each subsequent creep test maintained a similar minimum creep rate and time to the creep strain threshold. Due to the factor of 2.8 increase in the creep rupture life for both the 2%

and 3% creep strain threshold tests and a stable minimum creep rate, rejuvenation was considered successful.

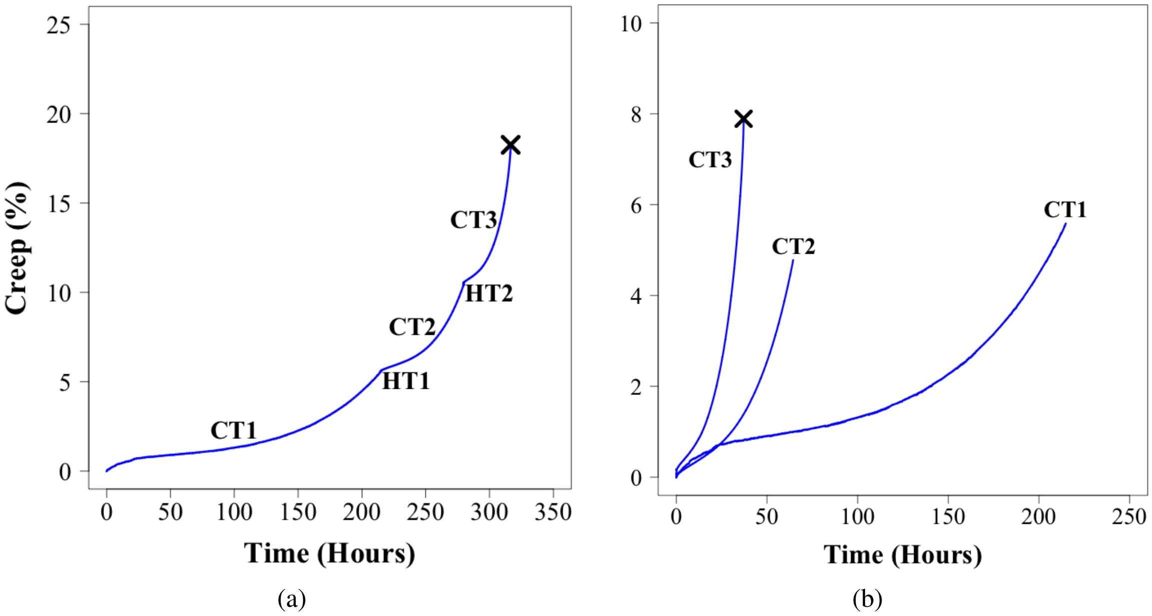

Figure 5.1: a) Multiple rejuvenation creep plot of N5-28-5 with a creep strain threshold of 5% strain. Each creep test and rejuvenation heat treatment is labeled. b) Plotting each creep curve with the same reference point allows for direct comparison between tests.

The inability of a rejuvenation heat treatment to recover creep performance indicates the presence of unrecoverable damage at 5% creep strain, such as creep cavities and cracked carbides that were not observed in the 2D sections of an interrupted creep specimen crept to 5% strain as discussed in Section 3.1.4. At the lower strain thresholds of 2% and 3%, complete recovery of the initial creep properties was also not achieved, however, the minimum creep rate and time to the respective strain threshold were stable during each subsequent

Table 5.2: Summary of the important creep parameters from the multiple rejuvenation tests performed on René N5(SX) creep specimens. The creep test number (CT#) corresponds to the labeled creep curves in Figures 5.1 and 5.2. The minimum creep rate, $\dot{\epsilon}_0$, creep time, and strain for each test is reported. CT3 for the 5% creep strain threshold test was tested to rupture due to unsuccessful rejuvenation. Rejuvenation heat treatments were only performed at a temperature of 28 °C below the γ' solvus.

René N5(SX) Multiple Rejuvenation Tests			
2% Creep Strain Threshold			
	$\dot{\epsilon}_0$ (s^{-1})	Creep Time (h)	Strain (%)
CT1	4.72×10^{-9}	181.40	2.00
CT2	1.69×10^{-8}	150.98	2.01
CT3	1.86×10^{-8}	149.45	2.02
CT4	1.72×10^{-8}	157.36	2.14
CT5	1.58×10^{-8}	151.47	1.98
CT6	1.75×10^{-8}	146.91	2.00
CT7	-	14.31	0.14
	Totals	951.87	12.30
3% Creep Strain Threshold			
	$\dot{\epsilon}_0$ (s^{-1})	Creep Time (h)	Strain (%)
CT1	7.22×10^{-9}	214.72	3.00
CT2	1.36×10^{-8}	184.50	3.01
CT3	1.42×10^{-8}	180.46	3.03
CT4	1.47×10^{-8}	183.65	3.09
CT5	1.39×10^{-8}	176.97	2.99
CT6	-	10.67	0.05
	Totals	950.97	15.17
5% Creep Strain Threshold			
	$\dot{\epsilon}_0$ (s^{-1})	Creep Time (h)	Strain (%)
CT1	1.58×10^{-8}	214.9	5.59
CT2	6.81×10^{-8}	64.5	4.78
CT3	1.32×10^{-7}	37.2	7.89
	Totals	316.5	18.26

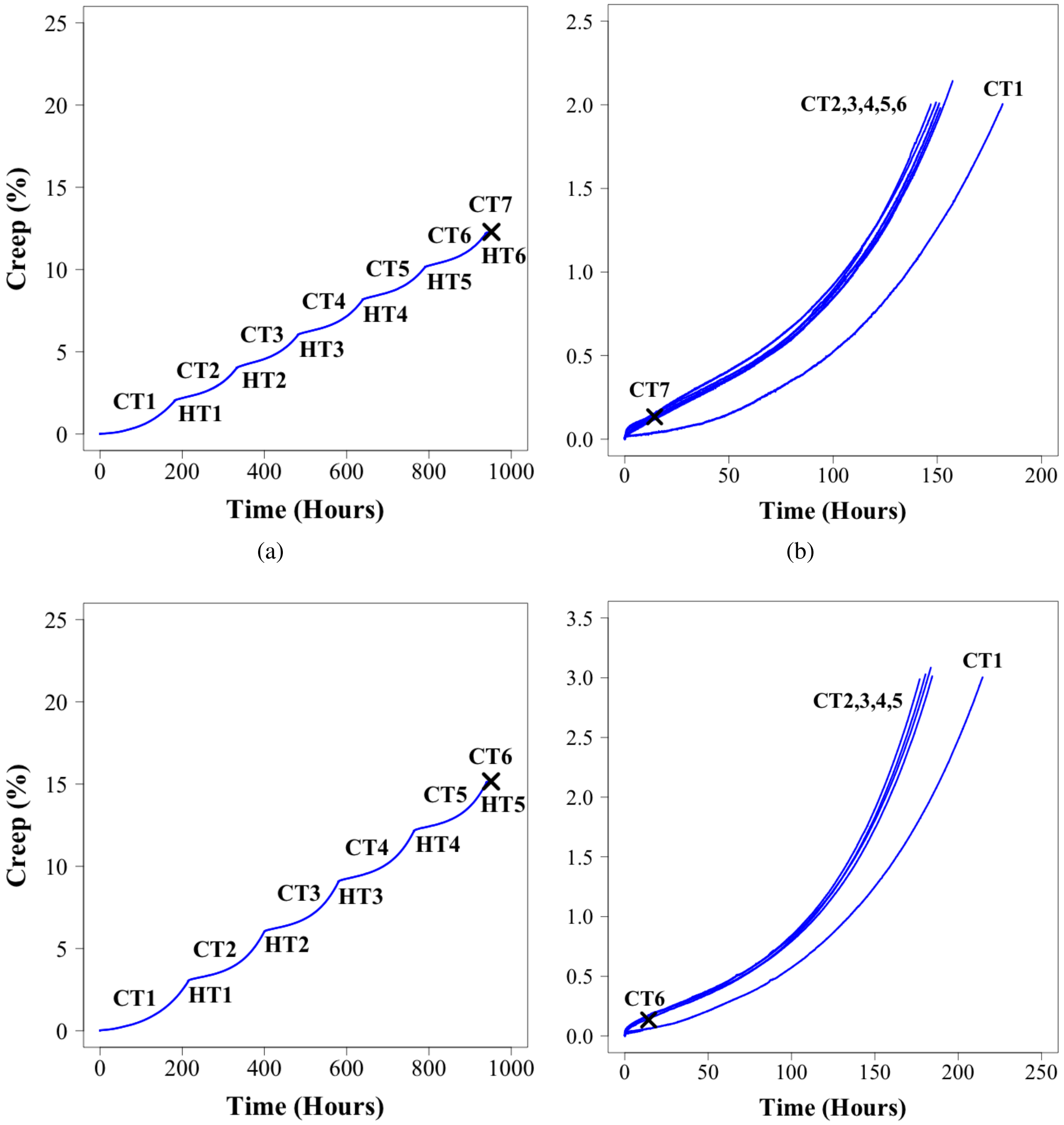

(a) (b)

(c) (d)

Figure 5.2: Multiple rejuvenation ((a) and (c)) creep plots for René N5(SX) tests N5-28-2 and N5-28-3, with a creep strain threshold of 2% and 3% strain, respectively. Each creep test and rejuvenation heat treatment is labeled. Plotting each creep curve with the same reference point ((b) and (d)) allows for direct comparison between each test.

creep test. This led to a significant increase in the overall creep rupture life compared to the baseline. A measurable increase in the amount of primary creep was observed after CT1 for each specimen, with the primary creep being measured by determining the intersection of the maximum primary creep rate and the minimum secondary creep rate [136, 137]. However, due to the variability in the amount of primary creep between specimens and between each subsequent creep test during multiple rejuvenation testing, primary creep was not used to quantify the amount of recovery and will not be discussed further.

Based on the multiple rejuvenation testing of René N5(SX) that incorporated creep testing at 982 °C/206 MPa, a critical creep strain threshold exists between 3% and 5% above which unrecoverable damage is present, inhibiting the successful use of a solution + aging rejuvenation heat treatment. In order to recover creep cavities, hot isostatic pressing (HIP) would need to be incorporated into the multiple rejuvenation test. Even interrupting below the critical creep strain threshold value does not result in complete creep rejuvenation. This is most likely a result of incomplete solutioning of the γ' precipitates leading to a less optimal γ' precipitate size and the retention of misfit dislocation networks in unsolutioned areas as discussed in Section 4.1 [27, 138].

Characterization of the specimens via EBSD after failure led to the discovery of recrystallization, which occurred during the rejuvenation heat treatments, Figure 5.3. Recrystallization was observed in all specimens tested (2%, 3%, and 5% strain threshold tests) and cracking occurred along the grain boundaries of the recrystallized grains that were oriented transverse to the loading direction. It is assumed that a majority of these surface cracks

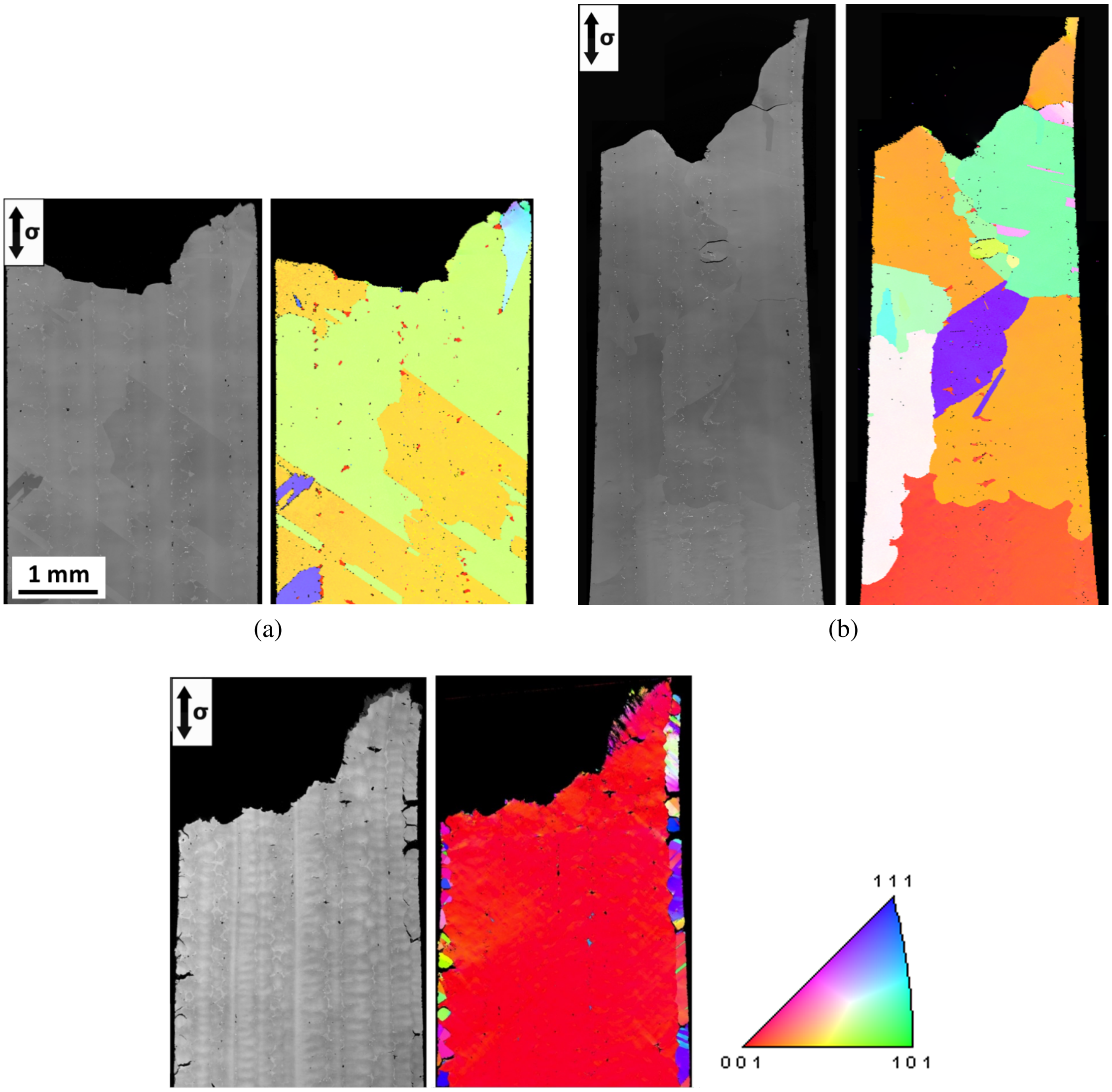

(a)

(b)

(c)

Figure 5.3: Backscattered electron images and inverse pole figure maps with respect to the loading direction of René N5(SX) specimens with a strain threshold of a) 2%, b) 3%, and c) 5% corresponding to tests N5-28-2, N5-28-3, and N5-28-5, respectively. The loading direction is indicated in the images and the scale is the same for each micrograph and EBSD scan.

formed during subsequent creep testing following recrystallization during the previous rejuvenation heat treatment. The entire reduced gauge section of both tests N5-28-2 and N5-28-3 recrystallized with several dominant recrystallized grains being observed.

NDE indicated that detectable levels of recrystallization were present after the last rejuvenation heat treatment performed before failure for each creep specimen. This corresponds to HT6, HT5, and HT2 for the 2%, 3%, and 5% creep strain threshold tests, respectively. The details and results of NDE are discussed further in Chapter 7. Recrystallization and the corresponding surface cracks caused rupture and prevented indefinite rejuvenation. Compared to an uninterrupted creep test, failure due to recrystallization did not involve significant void growth and is comparable to the failure of a polycrystalline specimen.

5.1.2 Influence of the Solution Temperature on Rejuvenation

With a critical strain threshold established, further multiple rejuvenation tests were performed using a 2% creep strain threshold, which is a conservative level of strain based on the interrupted testing. Additional solution temperatures of at the γ' solvus and 56 °C below the γ' solvus were investigated during rejuvenation. This is in addition to the prior test, which used a 2% creep strain threshold and a solution temperautre 28 °C below the γ' solvus, as shown in Figure 5.2a. Figure 5.4 shows the results of N5-FS-2 and N5-56-2, with the important creep testing results being listed in Table 5.3.

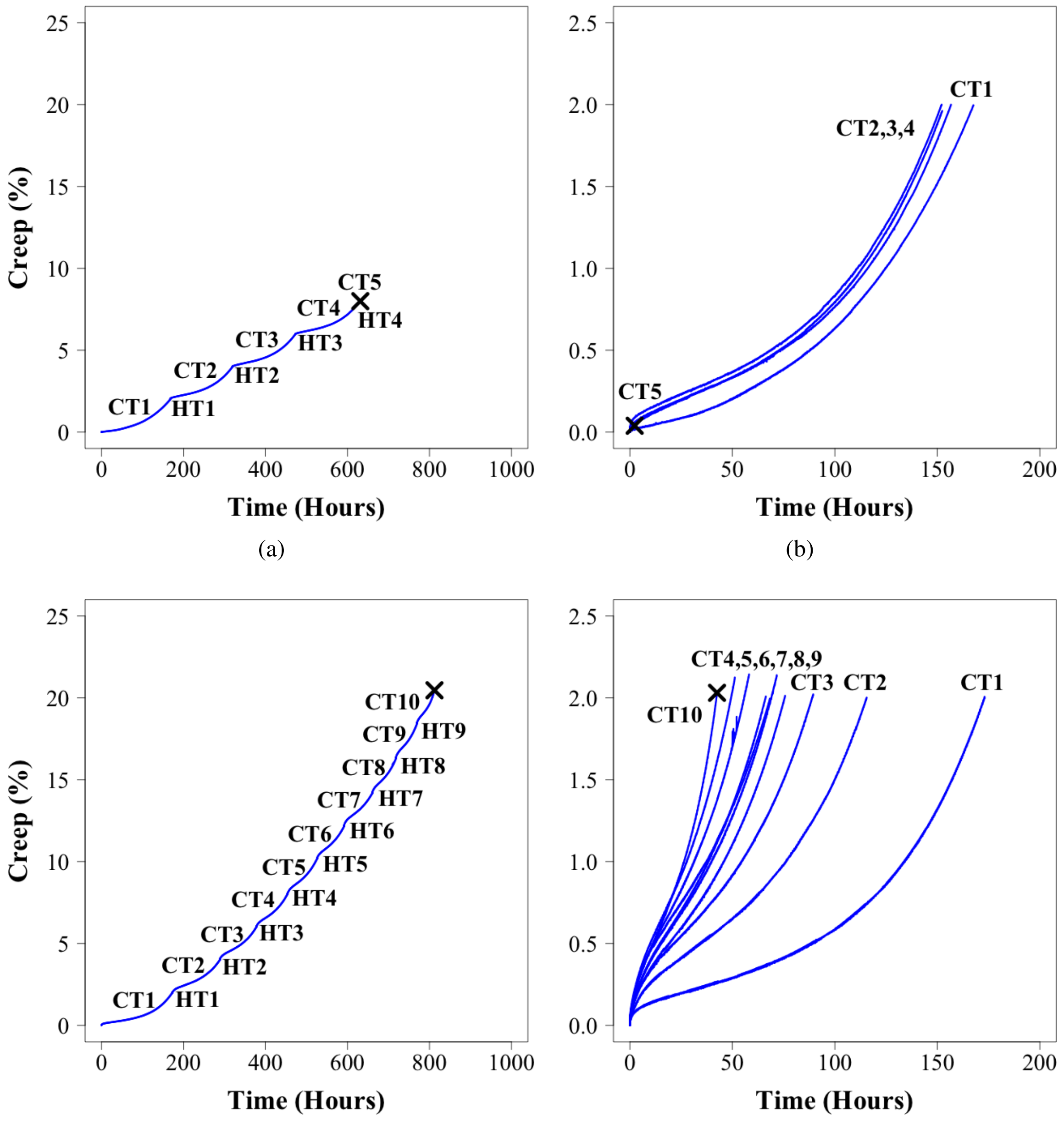

(a) (b)

(c) (d)

Figure 5.4: Multiple rejuvenation ((a) and (c)) creep plots for René N5(SX) with solution temperatures at the γ' solvus and 56 °C below the γ' solvus, respectively (corresponding to tests N5-FS-2 and N5-56-2, respectively). Each creep test and rejuvenation heat treatment is labeled. Each creep curve is plotted with same reference point ((b) and (d)) for direct comparison between tests.

Table 5.3: Summary of the important creep parameters for multiple rejuvenation tests performed on René N5(SX) creep specimens with two different rejuvenation solution temperatures of 56 °C below and at the γ' solvus. The creep test number (CT#) corresponds to the labeled creep curves in Figure 5.4. The minimum creep rate ($\dot{\epsilon}_0$), creep time, and strain for each test are reported. A 2% creep strain threshold was used for both tests.

René N5(SX) Multiple Rejuvenation Tests			
Rejuvenation at the γ' Solvus			
	$\dot{\epsilon}_0$ (s^{-1})	Creep Time (h)	Strain (%)
CT1	7.78×10^{-9}	161.63	2.00
CT2	1.42×10^{-8}	152.13	2.00
CT3	1.39×10^{-8}	152.40	1.96
CT4	1.42×10^{-8}	156.69	2.00
CT5	-	2.34	0.04
	Totals	625.20	8.00
Rejuvenation at 56 °C below the γ' Solvus			
	$\dot{\epsilon}_0$ (s^{-1})	Creep Time (h)	Strain (%)
CT1	9.17×10^{-9}	173.13	1.99
CT2	2.39×10^{-8}	115.55	2.00
CT3	3.50×10^{-8}	89.49	2.02
CT4	4.31×10^{-8}	75.75	2.01
CT5	5.17×10^{-8}	71.70	2.14
CT6	5.36×10^{-8}	66.33	2.01
CT7	5.19×10^{-8}	68.39	2.00
CT8	6.47×10^{-8}	58.14	2.14
CT9	7.28×10^{-8}	51.20	2.13
CT10	7.94×10^{-8}	42.52	2.03
	Totals	812.19	20.47

A rejuvenation heat treatment at the γ' solvus was unable to completely recover the initial creep performance. However, it did provide the best rejuvenated creep performance when compared to lower solution temperatures. Similar to the 2% and 3% creep strain threshold tests performed with solutioning 28 °C below the γ' solvus, each subsequent creep test maintained a consistent minimum creep rate and time to the creep strain threshold. The overall creep rupture life was 625 h, a factor of 1.8 increase over the baseline creep test. Multiple rejuvenation at the γ' solvus resulted in the lowest observed creep rupture strain of 8%.

A longer total creep rupture life of 812 h was observed for N5-56-2, a factor of 2.4 increase over the baseline. The total rupture strain was 20.5%, a result of ten creep tests and a corresponding nine rejuvenation heat treatments before failure. However, due to the low solution temperature the creep performance (minimum creep rate and time to creep strain threshold) degraded rapidly between the first and second test, comparable to N5-28-5. Property degradation continued during subsequent creep tests and did not stabilize.

Using a solution temperature of 28 °C below the γ' solvus provided the greatest increase in total creep rupture life and established consistent creep performance after the first rejuvenation heat treatment for a creep strain threshold of 2%. EBSD of the specimens after failure showed that recrystallization had occurred at all investigated solution temperatures, as shown in Figure 5.3a and Figure 5.5. Note that while the lowest solution temperature specimen did not rupture, due to significant necking it was deemed to have failed. Limited surface recrystallization was observed in the necked region after failure for test N5-56-2 while a majority of the reduced gauge section recrystallized in test N5-FS-2. NDE indicated that recrystallization occurred during the last rejuvenation heat treatment (HT4) for N5-FS-2. However, for test N5-56-2, the volume of recrystallized material was not significant enough for RUS to detect, indicating that the NDE technique

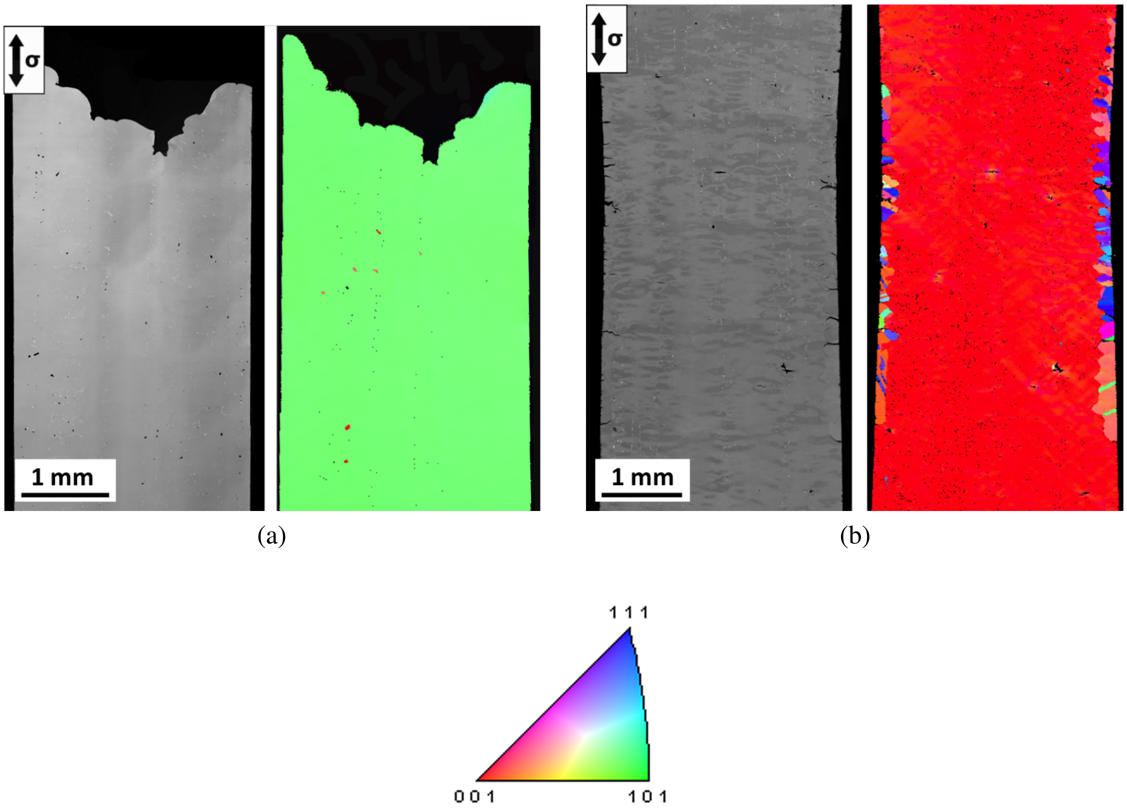

(a) (b)

Figure 5.5: Backscattered electron images and inverse pole figure maps with respect to the loading direction. Images are from multiple rejuvenation tests of René N5(SX) tests N5-FS-2 and N5-56-2, with a strain threshold of 2% and solution temperatures during rejuvenation a) at the γ' solvus and b) 56 °C below the γ' solvus, respectively. The loading direction is indicated on both images. The scale is the same for each micrograph and EBSD scan.

is only capable of detecting recrystallization after a critical volume fraction of recrystallized material has been reached, assuming a random orientation of recrystallized grains.

From the multiple rejuvenation tests of René N5(SX), it can be concluded that recrystallization limits the extent to which a specimen can be rejuvenated over a range of solution temperatures from 56 °C below the full γ' solvus to the full solvus and by interrupting creep tests between 2-5% strain. In the next section, the multiple rejuvenation testing results of GTD444(CG) specimens will be discussed and compared to the René N5(SX) results.

5.2 Multiple Rejuvenation - Creep of GTD444(CG)

Rejuvenation heat treatments for GTD444(CG) were performed at a solution temperature 14 °C below the γ' solvus to recover the initial γ' morphology as discussed in Section 4.1. The results of testing to 1%, 2%, and 3% creep strain thresholds are shown in Figures 5.6 and 5.7, and listed in Table 5.4. All GTD444(CG) specimens were crept at 982 °C/179 MPa. Test 444-14-1 was the most successful with a total creep rupture life and rupture strain of 1037 h and 6.7%, respectively. The baseline creep performance of GTD444(CG) had a rupture life and rupture strain of 740 h and 8.2%, respectively. A consistent minimum creep rate and creep behavior was not established at the solution temperatures and creep strain thresholds investigated.

Two tests were performed at a creep strain threshold of 2% to illustrate the variability in creep performance. Tests 444-14-2a and 444-14-2b had total rupture lives of 600 h and 819

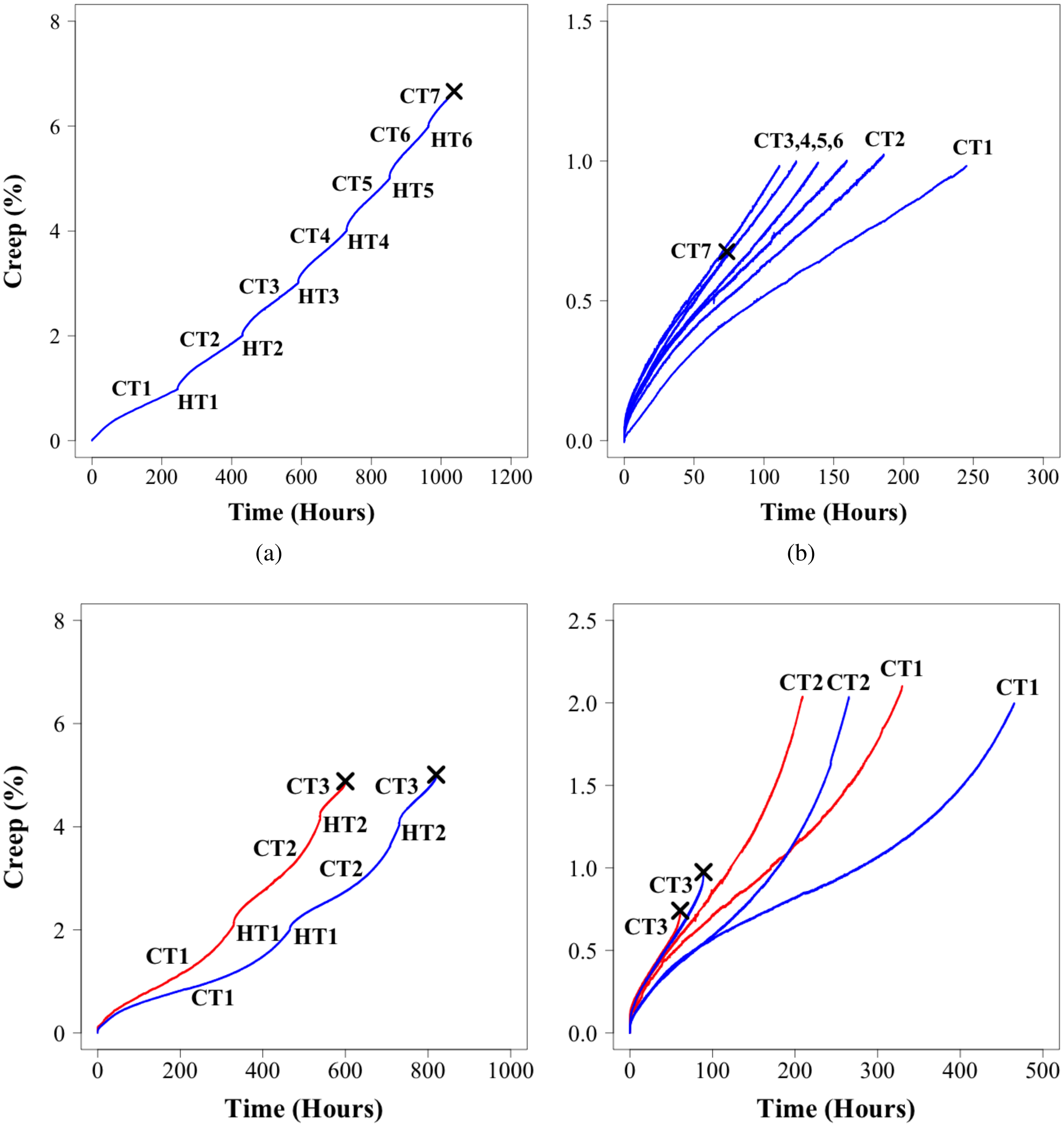

(a) (b) (c) (d)

Figure 5.6: Multiple rejuvenation ((a) and (c)) creep plots for GTD444(CG) tests 444-14-1, 444-14-2a, and 444-14-2b, which were solutioned 14 °C below the γ' solvus and tested to creep strain thresholds of 1% and 2%, respectively. Each creep test and rejuvenation heat treatment is labeled. Plotting each creep curve with the same reference point ((b) and (d)) allows for direct comparison between each test. The red and blue creep curves for the 2% creep strain threshold tests correspond to 444-14-2a and 444-14-2b, respectively.

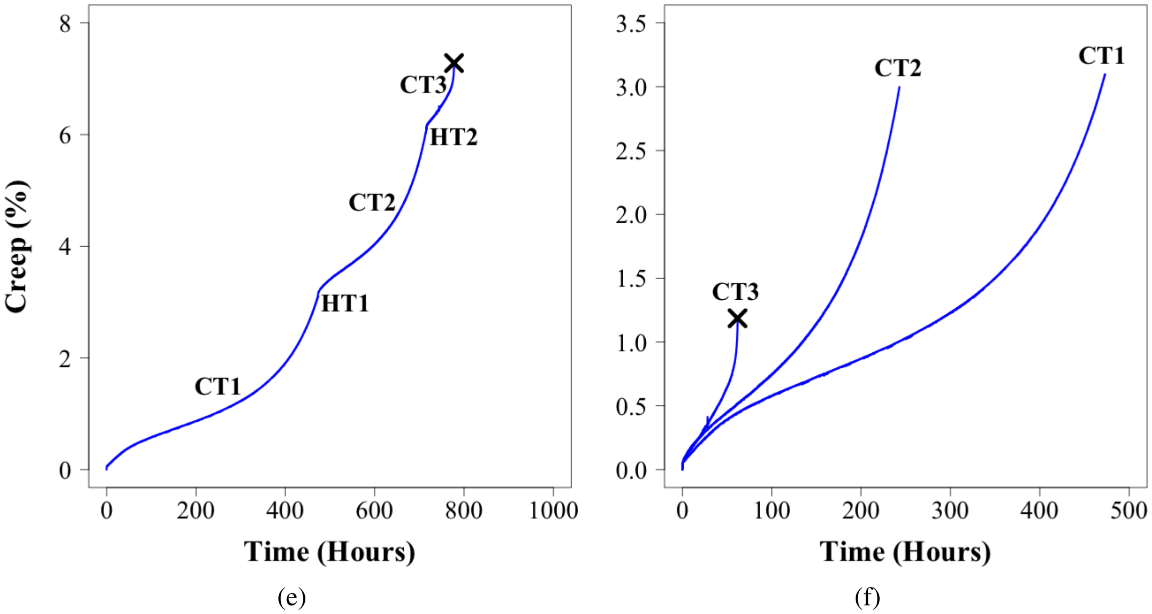

(e) (f)

Figure 5.7: Additional GTD444(CG) multiple rejuvenation creep plots ((e)-(f)); test 444-14-3 was solutioned 14 °C below the γ' solvus and interrupted at every 3% strain. Each creep test and rejuvenation heat treatment is labeled.

h and rupture strains of 4.88% and 5.01%, respectively. Using a 3% creep strain threshold in test 444-14-3 resulted in an increased total rupture life compared to test 444-14-2a of 778 h, 38 h longer than the baseline.

NDE of the GTD444(CG) specimens detected recrystallization during tests 444-14-2a, 444-14-2b, and 444-14-3 after the final rejuvenation heat treatment, corresponding to HT2 for each test. Detectable levels of recrystallization were not present in tests 444-14-1. Additional information on the NDE technique and specific results are presented in Chapter 7. EBSD scans and BSE images confirmed the presence of recrystallization in tests 444-14-2a, 444-14-2b, and 444-14-3, as shown in Figure 5.8. EBSD scans from test 444-14-2a

Table 5.4: Summary of the important creep parameters from the multiple rejuvenation tests performed on GTD444(CG) creep specimens. The creep test number (CT#) corresponds to the labeled creep curves in Figures 5.6 and 5.7. The minimum creep rate ($\dot{\epsilon}_0$), creep time, and strain for each test are reported. Rejuvenation heat treatments were performed 14 °C below the γ' solvus.

GTD444(CG) Multiple Rejuvenation Tests			
1% Creep Strain Threshold			
	$\dot{\epsilon}_0$ (s^{-1})	Creep Time (h)	Strain (%)
CT1	8.61×10^{-9}	241.11	0.98
CT2	1.19×10^{-8}	185.90	1.02
CT3	1.33×10^{-8}	159.44	1.00
CT4	1.47×10^{-8}	138.93	1.00
CT5	1.72×10^{-8}	123.22	1.00
CT6	1.86×10^{-8}	111.14	0.98
CT7	2.00×10^{-8}	73.50	0.68
	Totals	1037.24	6.66
2% Creep Strain Threshold (444-14-2a)			
	$\dot{\epsilon}_0$ (s^{-1})	Creep Time (h)	Strain (%)
CT1	1.11×10^{-9}	329.74	2.10
CT2	1.75×10^{-8}	209.10	2.04
CT3	2.31×10^{-8}	60.95	0.74
	Totals	599.79	4.88
2% Creep Strain Threshold (444-14-2b)			
CT1	6.67×10^{-9}	465.00	2.00
CT2	1.11×10^{-8}	265.15	2.04
CT3	1.97×10^{-8}	89.17	0.98
	Totals	819.32	5.01
3% Creep Strain Threshold			
	$\dot{\epsilon}_0$ (s^{-1})	Creep Time (h)	Strain (%)
CT1	7.78×10^{-9}	472.95	3.10
CT2	1.58×10^{-8}	242.91	3.00
CT3	2.50×10^{-8}	61.73	1.19
	Totals	777.59	7.28

also showed the presence of secondary dendrite arms from a neighboring primary dendrite, as shown in Figure 5.8b. The secondary dendrite arms resulted in the presence of high angle surface boundaries (> 25°) oriented transverse to the loading direction.

Compared to René N5(SX), the rejuvenation of GTD444(CG) was less successful, only able to extend the total creep life over the baseline by a factor of 1.4. Additionally, a stable minimum creep rate and consistent creep behavior were not established during any test, which indicates that even at the lowest creep strain threshold of 1%, unrecoverable damage was present. The presence of unrecoverable damage was most likely a result of transverse high-angle grain boundaries. While ideally the high-angle boundaries of CG alloys should be oriented parallel to the loading direction, EBSD scans shown in Figure 5.8 indicate that due to the tortuosity of the grain boundaries, portions of the grain boundary area are oriented perpendicular to the loading direction. As discussed in Section 1.3.1, grain boundaries transverse to the loading axis are a source of weakness in the microstructure. The low creep rupture ductility of the GTD444(CG) specimens supports this conclusion.

GTD444(CG), while less complex from a processing point of view than René N5(SX), has a more complex microstructure. Depending on where the creep specimen is machined from the plate of material, there can be several grains through thickness, leading to variability in creep properties. The volume fraction of unsolutioned phases was also higher in GTD44(CG) when compared to René N5(SX), as shown in Figure 4.1. The microstructure provides multiple damage initiation sites (carbides, eutectics, and grain boundaries), which prevented successful recovery of creep properties and make GTD444(CG) less amenable

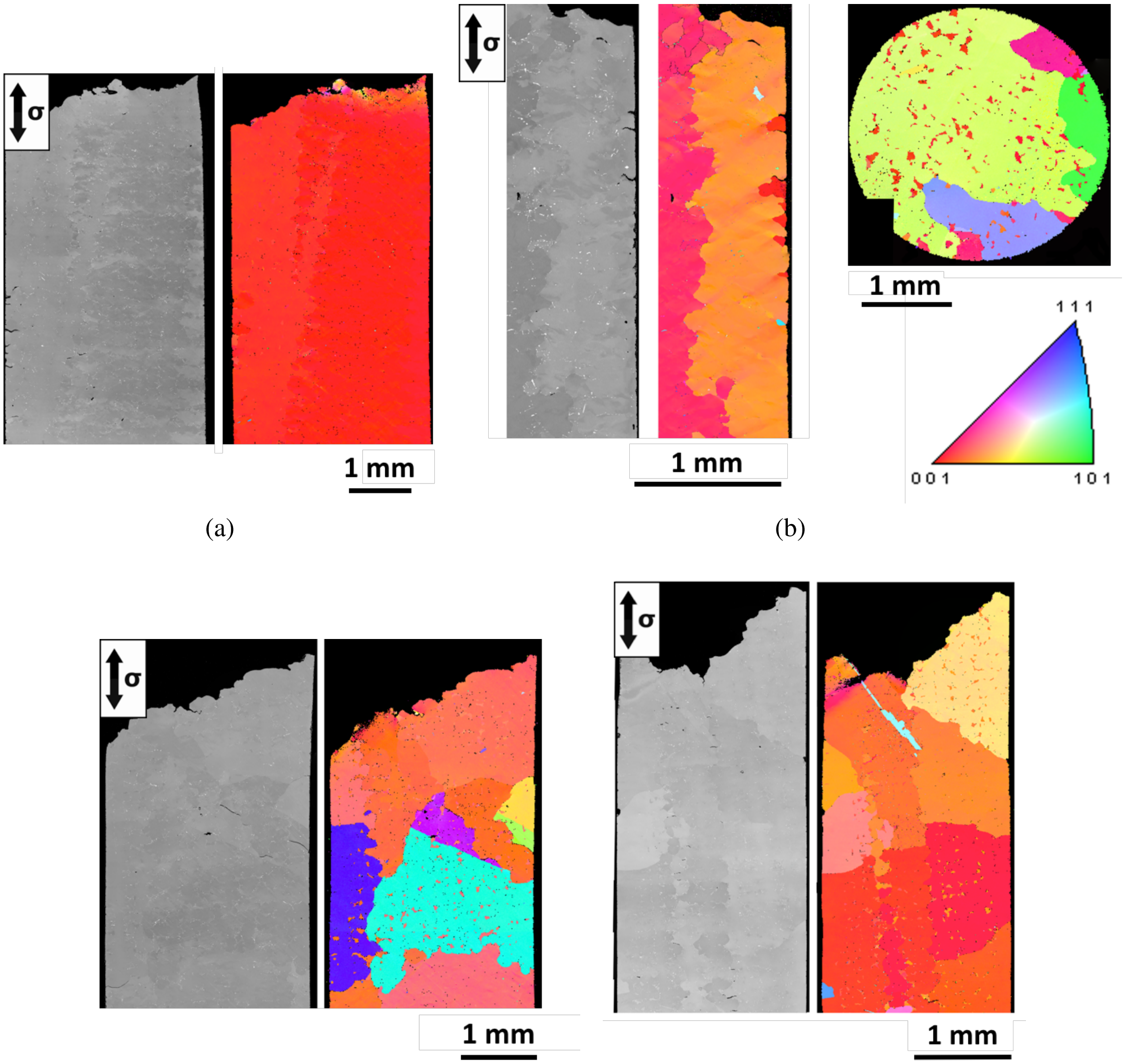

(a) (b)

(c) (d)

Figure 5.8: Backscattered electron images and inverse pole figure maps with respect to the loading direction. Images correspond to multiple rejuvenation tests 444-14-1, 444-14-2a, 444-14-2b, and 444-14-3, with strain thresholds of a) 1%, b)-c) 2%, and d) 3%, respectively. A transverse section of 444-14-2a was required to detect the recrystallization. The solution temperature during rejuvenation was 14 °C below the γ' solvus for all tests.

to rejuvenation than René N5(SX). Additional discussion of the factors limiting rejuvenation of GTD444(CG) and René N5(SX) will be presented in Chapter 6.

5.3 Multiple Rejuvenation - Creep of a β-NiAl Coated René N5(SX) Specimen

In order to determine the influence of coatings on rejuvenation, a β-NiAl coated René N5(SX) specimen was tested. The presence of a coating is expected to aid in the rejuvenation of creep properties by suppressing surface recrystallization [117]. The nucleation of recrystallization at the surface of the superalloy substrate will become less favorable due to the elimination of the free surface. In addition, β-NiAl coated René N5(SX) creep specimens should not contain a γ' depletion zone due to the reservoir of aluminum provided by the coating and will instead have an interdiffusion zone (IDZ) between the coating and superalloy substrate. An aluminide coating is commonly used in industry to promote the formation of a slow-growing and adherent α-Al_2O_3 oxide scale, which serves as a barrier to oxygen diffusion and provides compatibility with a ceramic top coat. Coatings were applied by using an aluminizing process that involved exposing René N5(SX) specimens to a high Al activity environment. This was followed by a diffusion heat treatment to promote the inward diffusion of Al and outward diffusion of Ni creating the IDZ. The IDZ has been shown to be rich in slow diffusing elements such as Re, Ta, and W [2].

A baseline creep test of β-NiAl coated René N5(SX) at 982 °C/206 MPa resulted in a total rupture life and rupture strain of 201 h and 34%, respectively. The rupture life was reduced by 144 h when compared to the baseline uncoated René N5(SX) creep performance at the same testing conditions. The decrease in life was a result of several factors, including the loss of the γ/γ' microstructure near the coating-substrate interface due to interdiffusion. Creep testing from literature indicates that the creep rate of $\langle 100\rangle$ oriented single crystals of β-NiAl is approximately 8 orders of magnitude higher than γ/γ' containing superalloys [139]. Degradation of the coating also occurs during creep testing and rejuvenation heat treatments, influencing mechanical performance. Diffusion of Ni and Al during high temperature exposure and Al depletion due to oxidation leads to the formation of a two phase β and γ' coating. The Ta-rich γ' grains that develop are susceptible to catastrophic oxidation [140]. A topologically closed packed (TCP) phase, σ, rich in Re, W, and Cr, also forms as a result of interdiffusion due to a decreased Ni activity in the γ phase [140, 141]. At high temperatures (> 850 °C), TCP phases decrease creep rupture life primarily due to the depletion of solid solution strengtheners from the matrix phase [2, 10, 142]. Micrographs collected after rupture of the baseline and rejuvenated β-NiAl coated René N5(SX) specimens showed the presence of the γ' phase in the coating, precipitation of TCP phases, and creep cavities, as shown in Figure 5.9.

Multiple rejuvenation testing of a β-NiAl coated René N5(SX) specimen resulted in a total rupture life of 541 h, an increase of a factor of 2.7 compared to the baseline, but had a reduced creep rupture ductility of 13.6%. The results for each creep test are listed in Table 5.5 and shown graphically in Figure 5.10. Recrystallization was not detected by NDE or

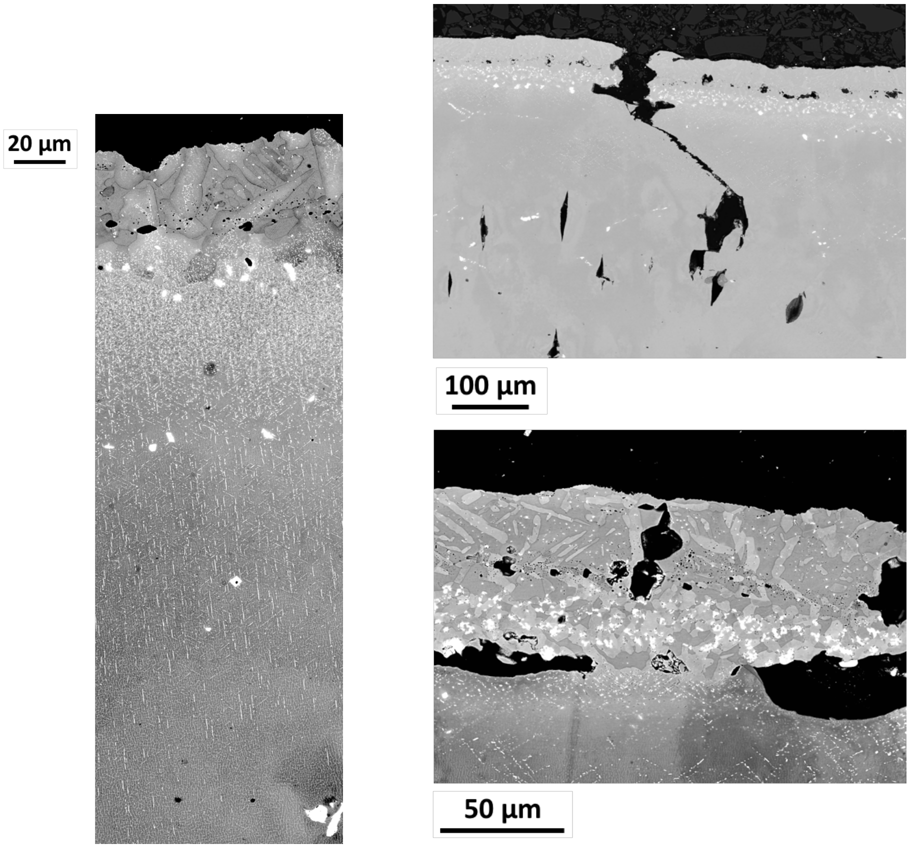

(a) (b)

Figure 5.9: a) Micrographs of the baseline β-NiAl coated René N5(SX) creep specimen tested to failure. b) Additional low magnification (top) and high magnification (bottom) images of the multiple rejuvenation β-NiAl coated René N5(SX) creep specimen after failure.

post-rupture metallographic examination, supporting the theory that recrystallization in the uncoated René N5(SX) specimens was initiated at or near the surface of the specimen.

Compared to the results of uncoated René N5(SX) and GTD444(CG), testing of a coated specimen was as successful and avoided recrystallization-induced failure. However, interdiffusion with the superalloy substrate and corresponding degradation of the coating and precipitation of TCP phases had a similar effect on the creep performance as the

Table 5.5: Table listing the important creep parameters from a β-NiAl coated René N5(SX) multiple rejuvenation test. The creep test number (CT#) corresponds to the labeled creep curves in Figures 5.10. The minimum creep rate ($\dot{\epsilon}_0$), creep time, and strain for each test are reported. Rejuvenation heat treatments were performed 28 °C below the γ' solvus and with a creep strain threshold of 2%.

β-NiAl Coated René N5(SX) Multiple Rejuvenation Tests			
	$\dot{\epsilon}_0$ (s^{-1})	Creep Time (h)	Strain (%)
CT1	1.44×10^{-8}	106.38	1.994
CT2	2.58×10^{-8}	86.42	2.032
CT3	3.19×10^{-8}	81.79	2.052
CT4	2.81×10^{-9}	78.47	2.034
CT5	3.06×10^{-8}	74.99	2.000
CT6	3.25×10^{-8}	76.23	1.994
CT7	3.97×10^{-9}	36.74	1.523
	Totals	541.02	13.63

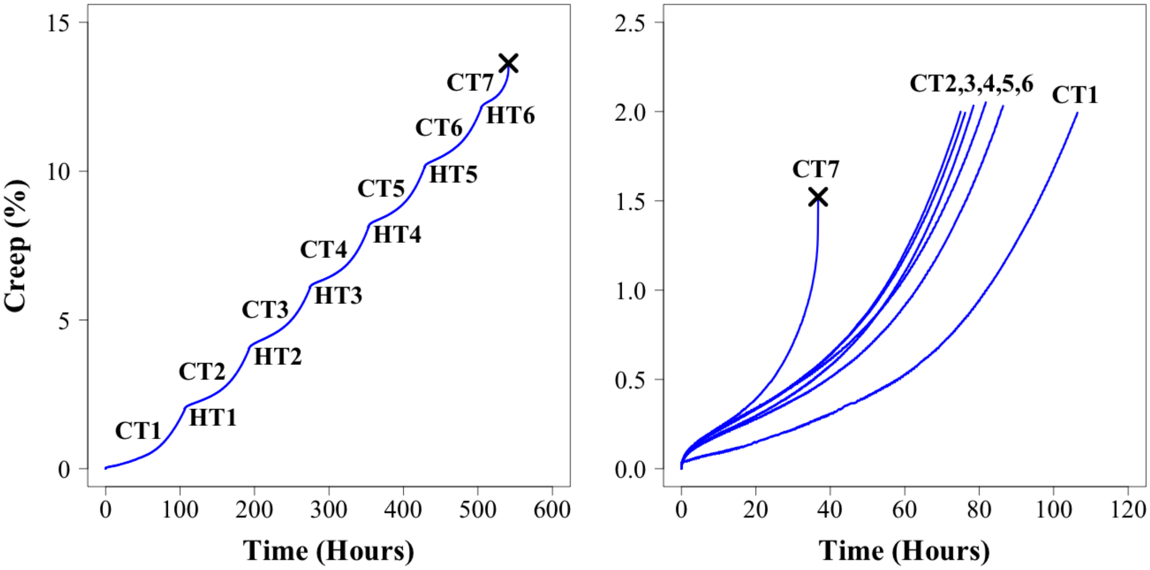

(a) (b)

Figure 5.10: a) Creep curves from multiple rejuvenation testing of β-NiAl coated René N5(SX) test N5-28-2-CT. b) The creep curves are also plotted using the same reference point for direct comparison.

introduction of transverse grain boundaries. While not as catastrophic as recrystallization, where failure occurred during the subsequent creep test, coating degradation was a contributing factor in the decreasing creep performance after each rejuvenation heat treatment.

The previous sections have summarized the results of multiple rejuvenation on recovering creep properties. The next section of this chapter will discuss the use of a rejuvenation heat treatment and removal of fatigue cracks via polishing to repair fatigue damage.

5.4 Multiple Rejuvenation - Fatigue of René N5(SX)

SPLCF testing was conducted on bare René N5(SX) at a temperature of 982 °C in air with a strain range of 0.6% and R = -∞ (A = -1.0). Refer to Section 2.2 for additional information on the SPLCF testing procedure and experimental setup. Rejuvenation heat treatments used a solution temperature of 28 °C below the γ' solvus. Multiple rejuvenation of René N5(SX) led to a factor of 2 increase in fatigue life compared to the baseline with no sign of impending failure, as shown in Figure 5.11. The increase in fatigue life only depended on the removal of previously formed fatigue cracks and not on the application of a rejuvenation heat treatment, indicating that significant recovery of the dislocation substructure is not necessary to extend SPLCF life. Subsequent crack formation and growth does not appear to be influenced by the preexisting dislocation substructure, but rather near surface plasticity and defects such as surface undulations and oxide cracks. This is in sharp contrast to rejuvenation of creep specimens where annealing dislocations and recovering a near virgin microstructural state is necessary to maintain creep properties [61].

Rejuvenation was limited by the amount of material remaining in the gauge section of the fatigue specimens. Approximately 400-600 μm of material was polished away after each fatigue test to remove all fatigue cracks, significantly greater than the maximum crack

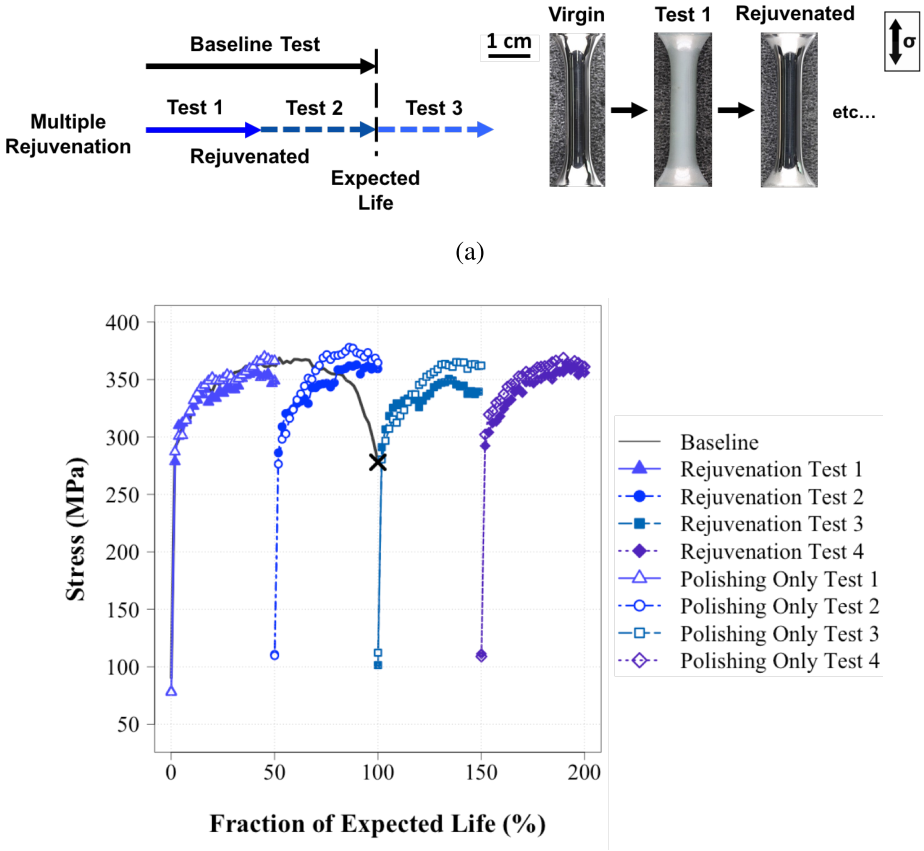

(a)

(b)

Figure 5.11: A summary of the SPLCF multiple rejuvenation test results: a) a schematic of the hypothesized result is shown along with images of a specimen at various steps of the process. b) A plot of the maximum stress in a cycle versus fraction of expected life shows that a specimen that is only polished performed similarly to a specimen that was polished and heat treated.

length of 91 μm observed via optical microscopy on 2D cross sections. This illustrates the importance of 3D microstructural characterization and the development of NDE techniques to more accurately determine crack length.

5.5 Summary & Important Conclusions

A René N5(SX) rejuvenation map was created as a convenient way to visualize the experimental results of multiple rejuvenation creep testing, as shown in Figure 5.12. Only creep tests with at least 80% recovery of the inital time to the creep strain threshold were considered successful. This criterion captured both early failure due to recrystallization and incomplete recovery. However, this successful rejuvenation criterion may not be appropriate for all situations and should be chosen on a case-by-case basis depending on the material and mechanical properties of interest. The area shaded red in Figure 5.12 indicates the region of total creep strain and number of rejuvenation cycles (note: a cycle included one creep test and one rejuvenation heat treatment) where unsuccessful rejuvenation is expected to occur. Conversely, successful rejuvenation was further subdivided based on the solution temperature used during the rejuvenation heat treatment, with the green shaded region being at the γ' solvus and blue region at 28 °C below the γ' solvus. The multiple rejuvenation tests used to generate this map included: N5-FS-2, N5-28-2, N5-28-3, N5-28-5 and a 1% creep strain threshold multiple rejuvenation test that was not discussed previously because the test failed as a result of experimental error. The rejuvenation cycle when recrystallization occurred for each test has also been indicated on the map. More tests are

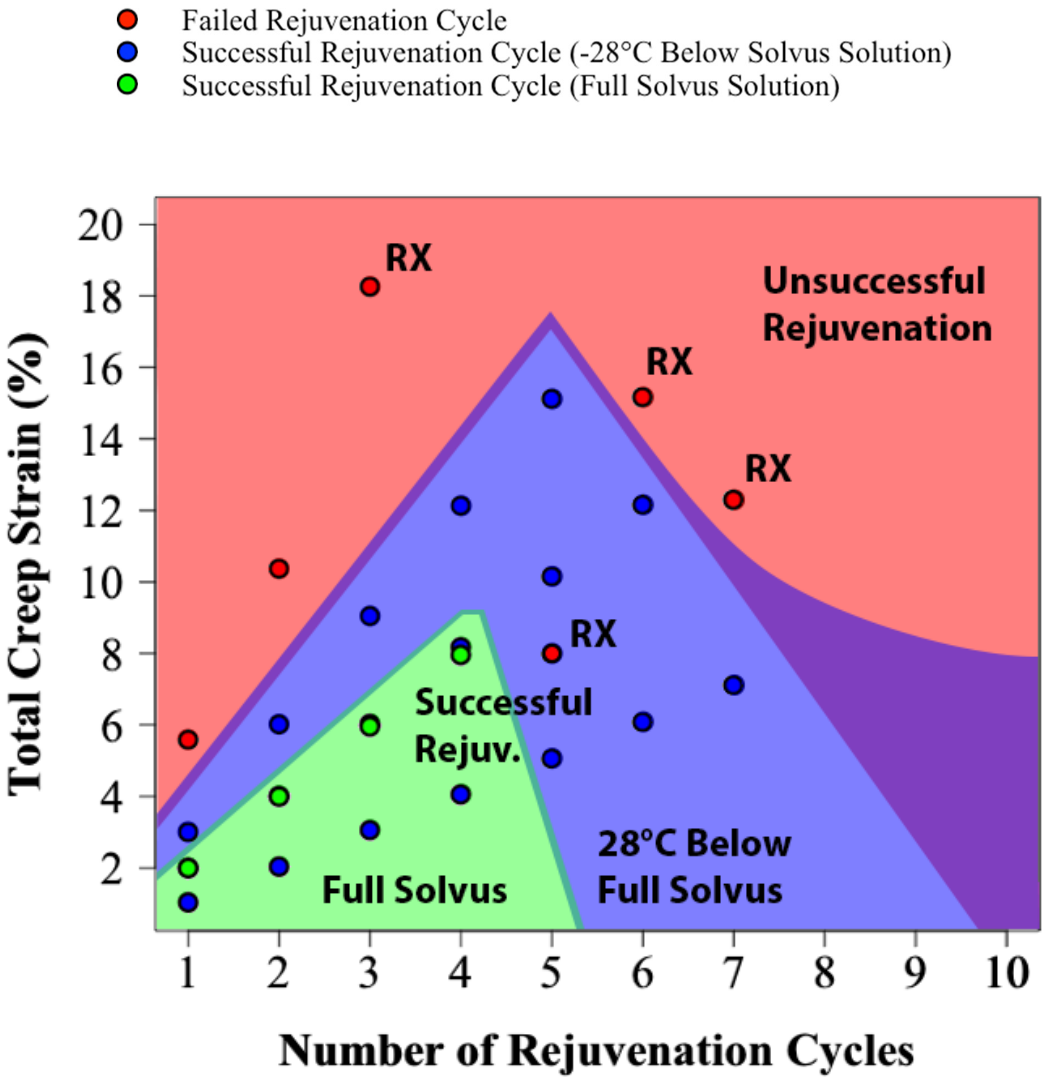

Figure 5.12: A René N5(SX) multiple rejuvenation testing map of total creep strain versus number of rejuvenation cycles with the regions of unsuccessful (red) and successful (blue and green) rejuvenation indicated. Only creep tests with at least 80% recovery of the original time to the creep strain threshold after rejuvenation were considered successful. The successful rejuvenation region is subdivided into two areas depending on the solution temperature, as indicated. This map is based on a limited number of experimental tests (corresponding to N5-FS-2, N5-28-2, N5-28-3, N5-28-5, and a 1% creep strain threshold multiple rejuvenation test) and the regions of uncertainty are indicated in purple. The rejuvenation cycle when recrystallization occurred has also been labeled for each test

required to produce an accurate map and as a result, the current map was conservatively constructed especially at a low total creep strain and a high number of rejuvenation cycles. The regions of uncertainty in the map are roughly outlined by the purple shading.

The general trends of the rejuvenation map are consistent with experimental results, namely, that the creep strain threshold before rejuvenation should be below 5% and that solution heat treatment should be performed near 28 °C below the γ' solvus. When comparing the data from multiple rejuvenation tests N5-28-2 and N5-28-3, which had similar total rupture lives, N5-28-3 would be preferred due to fewer total rejuvenation cycles. It has been shown that the mechanisms preventing successful rejuvenation primarily depend on the extent of high temperature exposure and the accumulation of strain. These factors result in the nucleation of recrystallization grains through the formation and growth of subgrains, which occurs at stress concentrations near the surface where there is a reduced grain growth barrier due to the oxidation induced depletion of γ'precipitates. Even without recrystallization, a critical accumulation of strain prior to rejuvenation prevents sufficient recovery of the initial creep properties.

Based on the experimental results of multiple rejuvenation testing presented in this chapter, several of the unanswered questions and hypotheses posed in Section 1.4.4 are addressed.

- Is rejuvenation possible in advanced DS alloys and, if so, at what total creep strain level is rejuvenation no longer viable?

Rejuvenation is possible in advanced DS alloys, with single crystal alloys being more amenable to rejuvenation than columnar grained alloys. In GTD444(CG), high angle twist boundaries (with respect to the [001] direction) are present and, due to the tortuosity of the grain boundaries, sections of these high angle grain boundaries are oriented transverse to the loading direction; these, along with recrystallization, prevented successful rejuvenation.

A critical creep strain threshold of between 3% and 5% strain exists for successful heat-treatment-only rejuvenation. The critical total creep strain before the introduction of irreversible damage varied depending on the material, creep strain threshold, and solution temperature employed during rejuvenation heat treatment. When recrystallization-induced failure occurred, multiple rejuvenation testing at a higher creep strain threshold and a lower solution temperature resulted in a higher total creep strain before failure. This is due to the presence of a significant volume fraction of γ' precipitates at lower solution temperatures and the specimen being exposed to fewer rejuvenation heat treatments.

- Can rejuvenation treatments be developed to recover damage and, consequently, recover both the creep and fatigue properties?

A rejuvenation treatment was successfully developed to recover both hold-time fatigue and creep damage. For fatigue damage, only the removal of fatigue cracks was required in order to extend fatigue life, indicating that crack growth is controlled by surface plasticity and defects such as surface undulations and oxide cracks.

An impractical amount of material for an industrial setting (400-600 μm) had to be removed from specimens interrupted at 50% of expected life. However, the use of coatings resistant to oxidation-assisted crack growth should allow rejuvenation via re-coating rather than substrate material removal. Specimens could also be interrupted at a lower fraction of expected life to lower the amount of material removal required.

- For the case of CG and SX alloys, can recrystallization be avoided during rejuvenation treatments?

Recrystallization was the life-limiting failure mechanism for a majority of the multiple rejuvenation creep tests performed. However, by reducing the solution temperature, recrystallization can be delayed and by applying a coating, even suppressed. With a coating, the nucleation of recrystallization at the surface of the superalloy substrate became less favorable due to the elimination of the free surface. In addition, β-NiAl coated René N5(SX) creep specimens did not contain a γ' depletion zone due to oxidation.

While there was a comparable extension of total creep rupture life between coated and uncoated tests, testing of a coated specimen did illustrate the feasibility of suppressing recrystallization. Further refinement of the multiple rejuvenation testing to include re-coating between creep tests and/or the application of coatings for use only during heat treatment could be employed to minimize the influence of coating degradation on the mechanical properties. Of course, there is additional cost associated with coating and re-coating and unless, as a result, rejuvenation can be extended substantially, would not be justifiable.

The primary mechanisms limiting rejuvenation appear to be the presence of stress concentrators, such as grain boundaries, and the evolution of the microstructure that occurs during mechanical testing or the rejuvenation heat treatment itself. Further discussion of the factors that limit successful rejuvenation will be presented in the subsequent chapter.

Chapter 6

Factors Limiting Rejuvenation

While multiple rejuvenation was successful in extending the life of single crystal René N5(SX) creep and fatigue specimens, there were several microstructural features potentially limiting recovery that will be addressed in this chapter. These include the presence of transverse grain boundaries due to recrystallization and/or their inherent existence in GTD444(CG) specimens, carbide decomposition, and solidification porosity. Consequently, full recovery of mechanical properties, the primary goal of rejuvenation, may not be possible in the complex alloys investigated. There are additional considerations that will lead to variability in the overall life extension, including the crystal orientation and the formation of topologically closed packed (TCP) phases.

Turbine blades used for land-based gas turbine engines are currently expected to operate for up to 24,000 h or 2.74 yrs before the first inspection interval and potential rejuvenation treatment, as discussed in Section 1.4. This extended high temperature exposure will undoubtedly lead to a difference in the microstructural evolution when compared to the multiple rejuvenation tests performed in this work, which at most were tested for 215 h before being rejuvenated.

All of these points will be addressed in the next few sections along with intermittent discussion of the relevant published literature, beginning with the influence of crystallographic orientation on mechanical properties.

6.1 Influence of Crystal Orientation on Creep and Rejuvenation

Numerous studies have examined the influence of crystal orientation on creep and fatigue properties of Ni-base superalloys [45, 136, 137, 143, 144]. These investigations have focused on creep deformation at intermediate temperatures (760 °C – 850 °C) and high stresses (500 MPa – 750 MPa) where $a\langle 112\rangle$ ribbons capable of shearing the γ' precipitates have been shown to cause large primary creep strains. Because $\langle 112\rangle$ slip can be shut down by the activation of a second $a\langle 112\rangle$ slip system or by sufficient $\frac{a}{2}\langle 110\rangle$ activity, there is a strong orientation dependence.

At higher creep temperatures and lower stresses, comparable to the creep tests performed in this thesis work, the orientation dependence of primary creep is less significant due to the constriction of slip activity to the γ phase and dominance of $\frac{a}{2}\langle 110\rangle$ slip [136, 145–147]. Limiting the discussion to misorientation angles less than 25° from the

[001] direction, the variation in creep performance at these conditions has been rationalized by an increased Schmid factor from 0.41 on the [001] to 0.5 at a misorientation of 25° from the [001] direction, Figure 6.1 [130].

For the multiple rejuvenation tests presented in Chapter 5, the success of a rejuvenation treatment is based on the performance compared to prior creep tests, thus any initial variation due to misorientation is taken into account. However, if multiple rejuvenation tests are interrupted after a certain number of hours rather than a percent creep strain, then the initial orientation will have an impact on the amount of deformation in the specimen prior to rejuvenation and will affect the post-rejuvenation mechanical performance. This scenario would apply to rejuvenation of service-exposed turbine blades where the amount of creep strain will vary locally within a single blade and between blades. In general, crystal

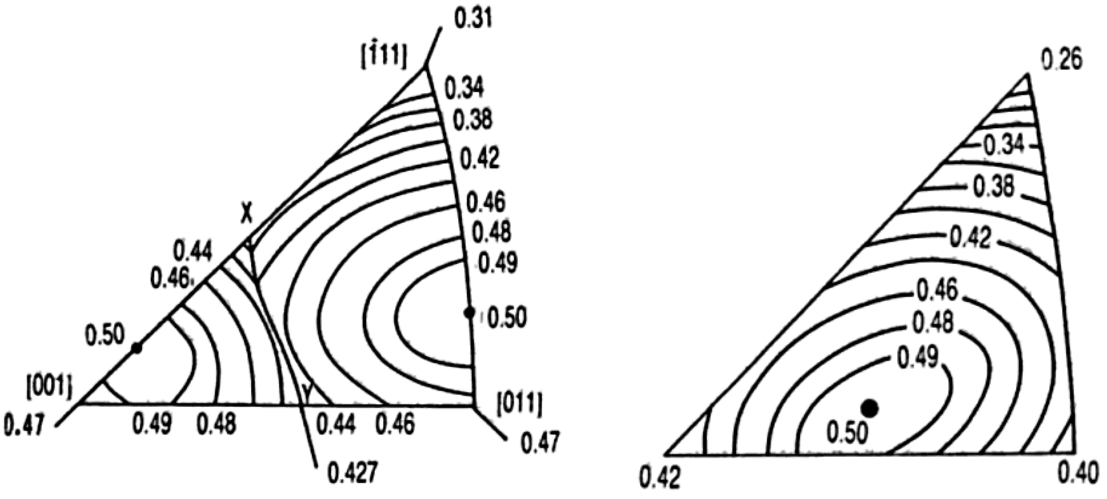

(a) (b)

Figure 6.1: Schmid factor contours for the highest stress slip systems from the: a) $\langle 11\bar{2}\rangle[111]$ and b) $\langle 1\bar{1}0\rangle[111]$ slip system families. Taken from MacKay, *et al.* and Nabarro, *et al.* [130, 137].

misorientation will prevent successful rejuvenation if using a total rupture life criterion due to the rejuvenated creep performance being limited by the initial properties.

6.2 Microstructural Defects

Besides crystal misorientation, microstructural defects such as solidification porosity, intrinsic transverse high angle grain boundaries or grain boundaries introduced via recrystallization, and the evolution and precipitation of minor phases also affect rejuvenation. This section will address the impact of these defects by examining literature and the experimental results of this thesis work, starting with transverse high angle grain boundaries.

6.2.1 Grain Boundaries Transverse to the Loading Direction

As discussed in Chapter 5, transverse grain boundaries are a source of weakness in the microstructure, being responsible for unsuccessful rejuvenation and the cause of failure in all GTD444(CG) and uncoated René N5(SX) multiple rejuvenation tests. Previous studies have examined static surface recrystallization in Ni-base superalloys due to damage associated with shot peening, grit blasting, and cold working [100, 117–122]. The influence of recrystallization on mechanical properties in CG and SX superalloys appears to depend on the alloy composition and the depth of the recrystallized layer [125, 148–151]. In general, recrystallization increases the minimum creep rate and decreases the rupture life due to the introduction of high angle grain boundaries, as discussed briefly in Section 3.1.2.5. There is a linear relationship between the fraction of recrystallized area and decrease in creep rupture life for both CG and SX alloys in the limited studies performed [148–150].

Previous research on bicrystals of Ni-base superalloys GTD444 and René N4 concluded that GTD444 specimens with only 0.09 wt% carbon and 0.009 wt% boron were able to tolerate a misorientation greater than 20° while maintaining the same creep rupture life and a creep rupture ductility over 5%, as shown in Figure 6.2 [152]. Crack formation occurred in GTD444 due to the deformation incompatibility between the two crystals. René N4, with approximately half the concentration of carbon and boron as GTD444, had a decrease in creep rupture life by a factor of 2 and a creep rupture ductility less than 1.5% in specimens with a misorientation greater than 20° between the two crystals [152]. Other alloys that do not have any additions of carbon or boron are even more prone to property degradation with the presence of high angle boundaries. For example, a bicrystal of CMSX-4 with a misorientation of 7° tested at similar creep conditions to the previous study lasted for 100 h while a perfect SX failed at over 10,000 h [2, 153].

The composition of René N5(SX) used in this study contained 0.05 wt% carbon and 0.005 wt% boron, comparable to René N4, thus specimens with grain boundaries having misorientations greater than approximately 10° will experience a decrease in creep rupture life and are sufficiently weak to fracture before significant plastic strain accumulation. This observation is supported by the multiple rejuvenation testing results, shown in Section 5.1, where specimens with extensive recrystallization failed within several hours and at creep strains below 0.2%. It was also hypothesized that inherent transverse grain boundaries in

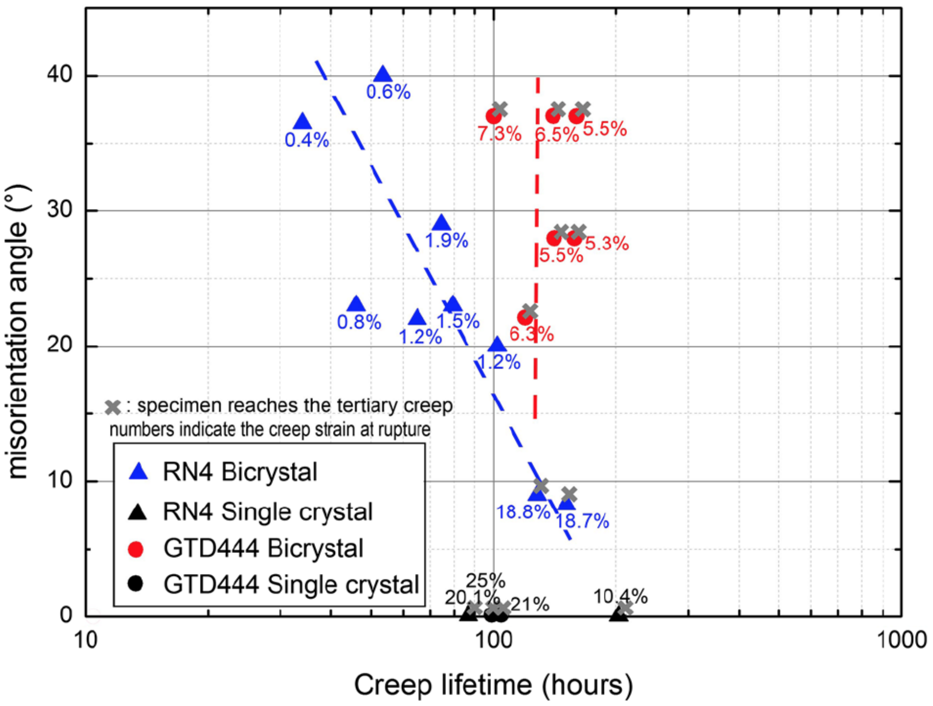

Figure 6.2: Plot of the creep rupture life (h) of René N4 and GTD444 bicrystals as a function of the bicrystal misorientation angle (°), illustrating the effect of the increased concentration of grain boundary strengtheners in GTD444 compared to René N4. From Stinville, *et al.* [152].

GTD444(CG) prevented successful rejuvenation. While GTD444(CG) has a higher concentration of grain boundary strengtheners, the boundaries still serve as a crack initiation sites and constrain the neighboring crystals. As shown by Stinville, *et al.*, the different deformation rates in the neighboring crystals forming the boundary can cause a build up of shear band-induced plastic gradients [152]. Cracking of the boundary occurs once a critical stress has been reached and preferentially occurs at the surface. This agrees well with EBSD scans of multiple rejuvenation test 444-14-2a (Figure 6.3), where intense bands of slip are associated with transverse high angle boundaries and boundaries located at the specimen surface have cracked. Recovery of the intense slip will not be possible with a rejuvenation heat treatment and thus failure should occur once a critical total creep strain value is reached. The comparable total creep rupture strains of between 4.88% and 7.28% for the GTD444(CG) multiple rejuvenation tests performed in Section 5.2 and those reported by Stinville, *et al.* of between 5.3% and 7.3% for bicrystals suggest a similar failure mechanism.

For rejuvenation of single crystals, it may be useful to develop an alloy that is specifically suited to rejuvenation with an increased concentration of grain boundary strengtheners to avoid catastrophic failure due to recrystallization. This, however, will cause a decrease in the incipient melting temperature and require modification of the post-casting heat treatment resulting in a less creep and fatigue resistant initial microstructure.

6.2.2 Solidification Porosity

Another defect to consider is solidification porosity, which can act as a stress concentrator and serves as a crack initiation site. Additionally, the growth of porosity reduces the load bearing cross-sectional area, increasing the effective stress on the remaining material during mechanical testing at elevated temperatures. Cavitation during creep testing of CG and SX alloys is typically limited to near and within the necked region, being observed at high strains during tertiary creep, as discussed in Section 3.1.1. Successful rejuvenation of the creep properties using only a solution and aging heat treatment was achieved by

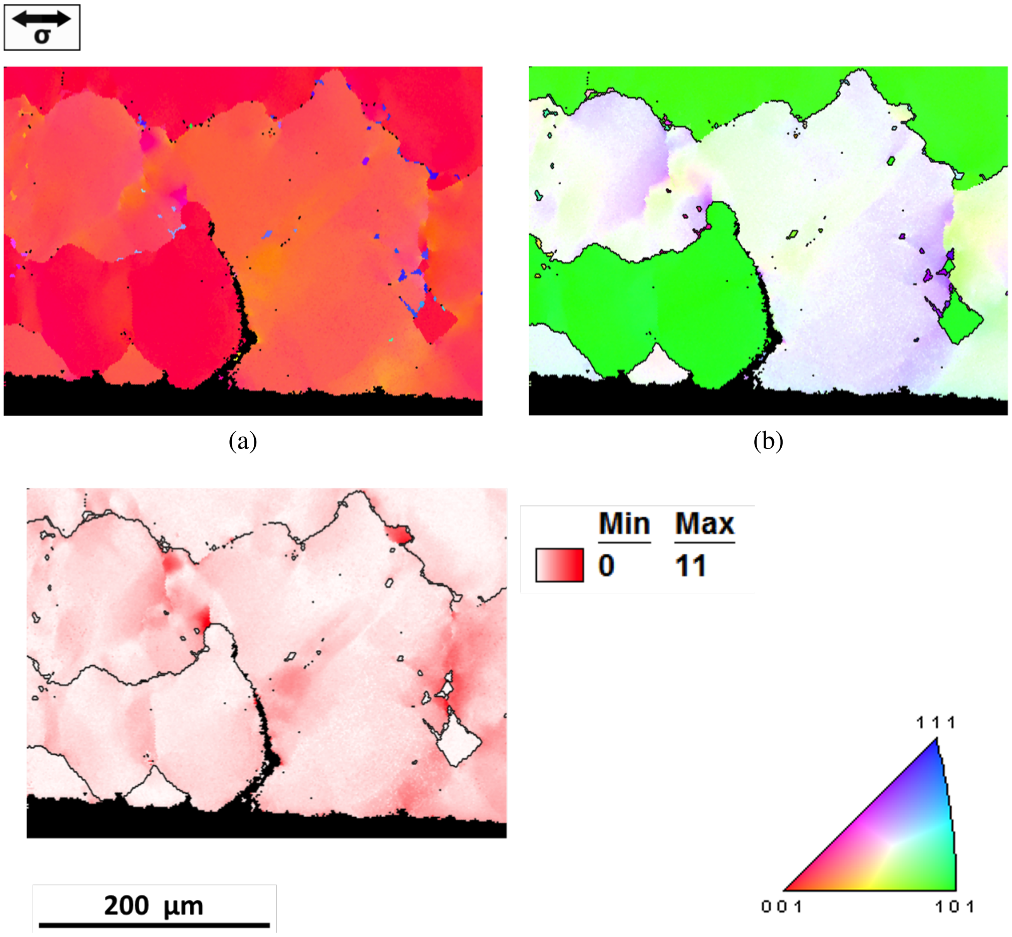

(a) (b)

(c)

Figure 6.3: Electron backscatter diffraction scans of multiple rejuvenation specimen 444-14-2a. Inverse pole figures with respect to the loading direction/growth direction (a) and transverse direction (b) are included along with a grain reference orientation deviation map (c) showing a misorientation of up to 11° near high angle boundaries. High angle boundaries (> 15°) are indicated on (b) and (c) by black lines.

interrupting creep tests at low strains prior to the onset of signification cavitation. Thus, discussion in this section will be focused on the role of porosity in fatigue.

Porosity in Ni-base superalloys forms due to dendritic solidification, where the liquid metal is unable to flow through interdendritic channels to compensate for shrinkage in the pockets of solidifying metal [154–156]. Gas porosity is avoided in Ni-base superalloys by performing casting in a vacuum. SPCLF damage has been successfully rejuvenated, however the primary form of damage in dwell-fatigue is the formation and growth of surface cracks. Observed crack nucleation sites in uncoated René N5(SX) SPLCF specimens include surface undulations and locations where carbides intersect the specimen surface and oxidize rapidly. Fortunately for the rejuvenation of SPLCF damage, surface cracks can be detected non-destructively by simple visual or fluorescent penetrant inspection.

The worst case scenario for the rejuvenation of fatigue damage involves internal crack initiation and growth, which requires hot isostatic pressing (HIP) to remove. Even then, HIP at typical conditions of 100 MPa and 1100 °C may cause recrystallization and less optimal control of the γ' precipitate size and shape [157]. Subsequent heat treatments to obtain the desired microstructure can cause the closed pores and cracks to reopen [157]. Thus, the best way to avoid internal cracks may be improving the alloy's resistance to crack initiation and growth by minimizing the number and size of the initiation sites (primarily porosity) introduced during solidification. Thesis work performed by Brundidge successfully implemented two modifications to improve the low-cycle fatigue life of René N5. As shown in Figure 6.4, the use of liquid metal cooling (LMC) allows faster solidification velocities than the traditional Bridgman method, refining the dendrite arm spacing and reducing the maximum pore size by 70% [158, 159]. The reduction in pore size led to a factor of between 3 – 7 increase in fatigue life depending on the stress amplitude. Adding additional levels of Ta to the base René N5(SX) composition also caused an improvement in fatigue life by strengthening the γ' precipitates, however it also led to an increased pore size compared to the baseline René N5(SX) composition.

Additional reports in the literature showed a factor of 4 improvement in low-cycle fatigue life of LMC specimens of the first generation Ni-base superalloy AM1 at 750 °C when compared to Bridgman cast samples [160]. For all tests performed by Steuer, *et al.* at 750 °C, cracks initiated from internal or near-surface porosity. At 950 °C, LCF life was shown to be independent of casting method and life was apparently limited by oxidation rather than the initial pore size. This was confirmed by conducting tests in vacuum, where LMC specimens displayed an improvement in fatigue life. Applying a coating to a specimen may also help suppress oxidation-induced failure.

Rejuvenation of low-cycle and high-cycle fatigue damage, which is commonly controlled by internal porosity, provides a significant challenge. HIP is capable of closing solidification porosity and healing un-oxidized fatigue cracks, however, it may cause recrystallization and degrade creep properties. Refinement of the microstructure and the addition of γ' strengtheners has been shown to significantly increase the fatigue life, and, through optimization, may prevent traditional fatigue from being the life limiting damage mechanism. Thus, several rejuvenation cycles that use a simple heat treatment that would not modify the internal solidification porosity could be used to repair visible surface cracks and creep damage until approaching the fatigue limit of the component.

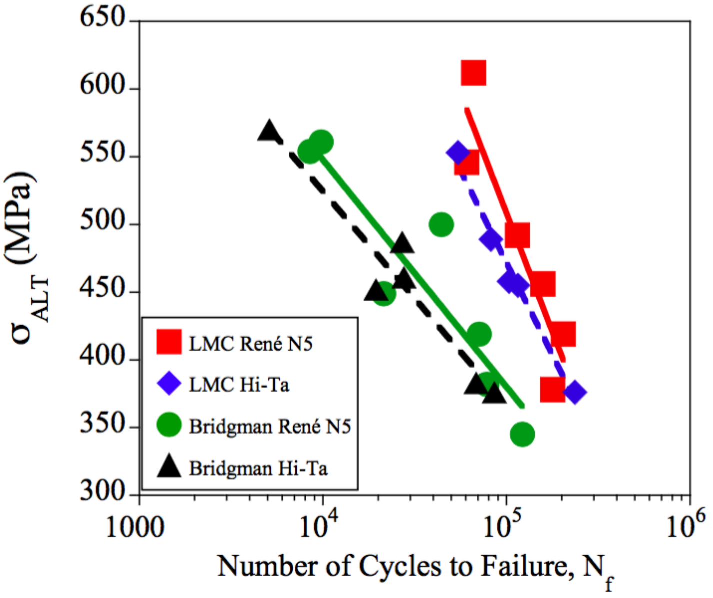

(a)

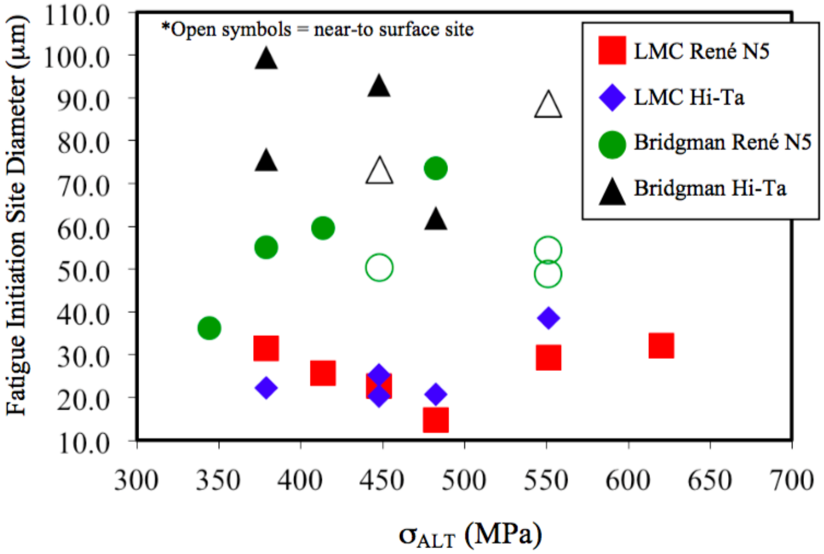

(b)

Figure 6.4: a) S-N curve for low-cycle fatigue tests performed at 538 °C illustrating the beneficial effect of liquid metal cooling on fatigue life. b) Measuring the diameter of crack initiation site for each tested specimen indicated that the improved fatigue life is a result of porosity refinement. Taken from Brundidge, *et al.* [159].

6.2.3 Carbides, Their Decomposition, and Topologically Closed Packed (TCP) Phases

Carbides, as discussed in Section 1.2.2, have cubic crystal structures with no apparent orientation relationship with the γ matrix. The addition of carbon and the formation of carbides is beneficial to the solidification of Ni-base superalloys by suppressing grain defect formation [161, 162]. However, carbides are also stress concentrators and have been observed to crack during creep testing, as mentioned in Section 3.1.1. High resolution EBSD by Karamched, *et al.* has determined, as shown in Figure 6.5, that the geometrically necessary dislocation density increases around carbides by a factor of between 3 – 6, depending on the imposed mechanical strain, compared to areas away from carbides during room temperature bend tests of the CG first generation Ni-base superalloy Mar-M-002 [163].

Long term aging studies have shown that primary (MC) carbides decompose to secondary $M_{23}C_6$, M_7C_3, and M_6C carbides, that are enriched in Cr [81, 164]. The depletion of Cr from the γ matrix leads to the formation of the less ductile γ' phase at the carbide-matrix interface, promoting crack formation during fatigue. However, carbon and boron strengthen grain boundaries, improving creep properties, specifically rupture life for PC and CG Ni-base superalloys [2, 10, 165]. The formation of the $Ni_3(TiTa)$ η phase, with a hexagonal DO_{19} crystal structure, has also been reported in a PC GTD111 alloy with a suggested decomposition reaction of $MC + \gamma/\gamma' \rightarrow M_{23}C_6 + \eta$ rather than the traditional

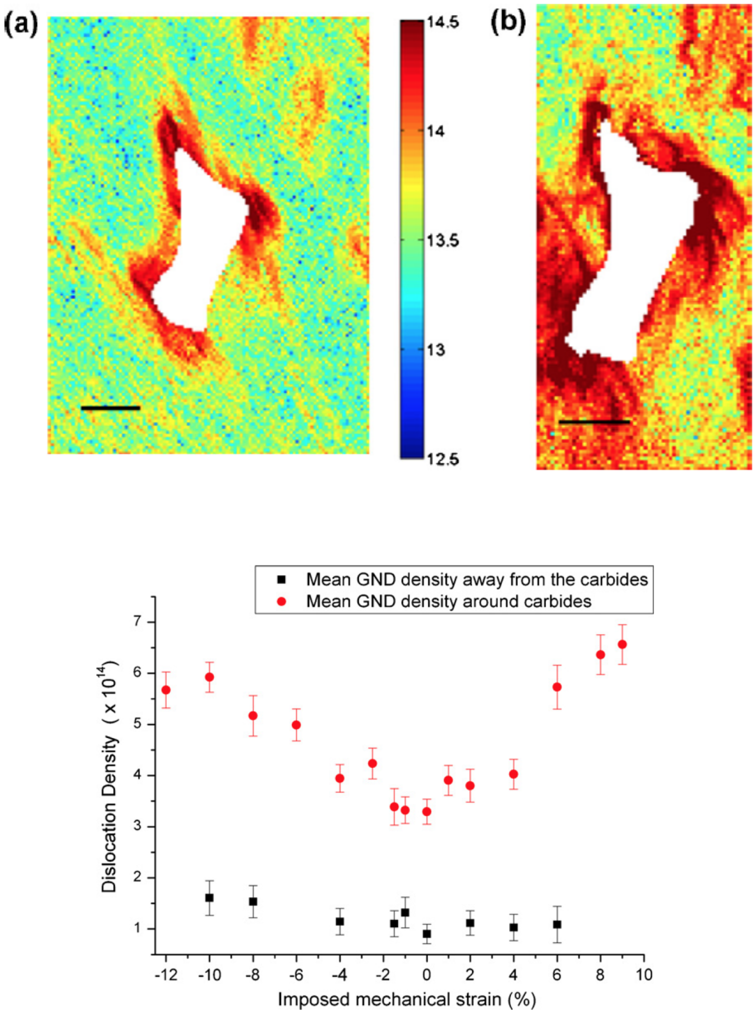

(c)

Figure 6.5: The a) thermally induced and b) after subsequent compression to 6% strain total density of geometrically necessary dislocations per meter squared around a carbide. The scale bars are 5 μm long, and a step size of 0.25 μm was used. c) Karamched, *et al.* also collected scans around carbides along a beam bent to 10%, providing information on the geometrically necessary dislocation density at various strain levels [163].

MC + γ → $M_{23}C_6$ + γ' decomposition reaction [2, 166, 167]. The Ti and Al concentration in the alloy are primarily responsible for the precipitation of the η phase [166, 168, 169]. Ti helps to stabilize the η phase, having the DO_{19} structure, while Al stabilizes γ'.

Blades in service, as mentioned previously, can be under load at temperature for up to 24,000 h before inspection. The creep and fatigue tests typically performed in a scientific setting only last for hundreds of hours, thus the microstructure is expected to be significantly different between the two extremes. To investigate this effect, long term creep specimens of GTD444(CG), provided by Art Peck at GE Power, were examined by electron microscopy, with a specific focus on characterizing the carbide decomposition and its potential impact on mechanical properties and rejuvenation.

A total of seven specimens were crept transverse to the growth direction at various temperatures and stresses until failure, defined by complete specimen separation. Each creep test lasted for at least 1000 h with one specimen lasting over 15000 h. Creep testing was performed by Joliet Metallurgical Laboratories, Inc., per ASTM E138. Examination of the specimens indicated a change in failure mechanism depending on the applied stress. For example, ductile failure was observed for Specimen B which was tested at 276 MPa, while Specimen E was tested at 69 MPa and failed in a brittle manner at two locations along the gauge length. The fracture surfaces of tested specimens showed that internal oxidation along grain boundaries occurred in some cases. Samples with greater than 45% intergranular oxidation (IGO) had a factor of two reduction in plastic strain at rupture compared to specimens with less than 2% IGO. The fracture surfaces of Specimen B and Specimen E are shown in Figure 6.6. Notice the blue color of the mixed oxides on the left side of Specimen E. A Larson-Miller plot of the creep tests along with the rupture strain and extent of IGO evident from the fracture surfaces is shown in Figure 6.7. There appears to be a stress threshold of approximately 120 MPa above which oxidation did not play an important role in failure due to the relatively short test length. IGO was the dominant failure mechanism when samples were exposed to high temperatures for extended periods of time.

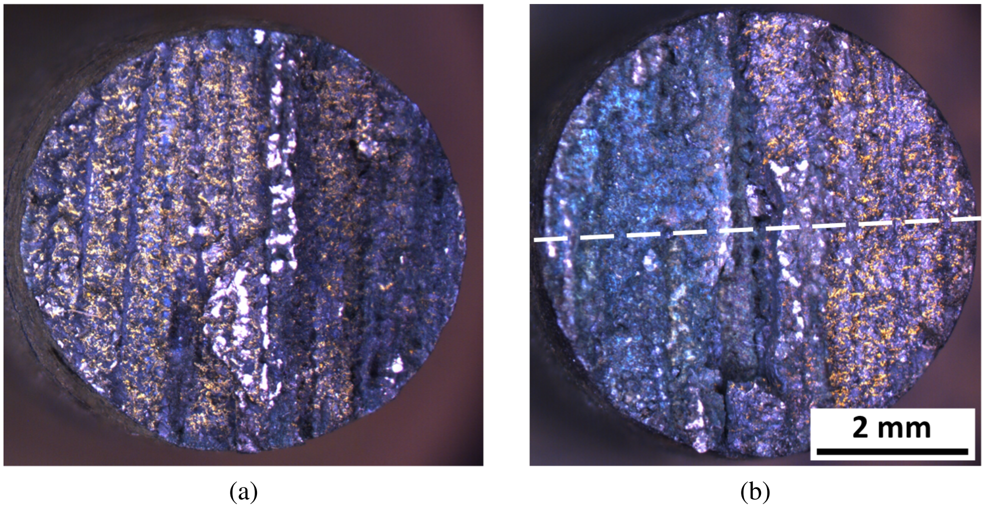

(a) (b)

Figure 6.6: Fracture surfaces imaged via optical microscopy of a) Specimen B and b) Specimen E. The white dashed line indicates how the specimen was sectioned for further metallographic examination.

Specimen E was sectioned along the dotted line shown in Figure 6.6b for further examination via EBSD and electron microscopy. A phase map, inverse pole figure with respect to the growth direction, and backscattered electron image collected near the specimen surface confirmed the presence of the η phase and small regions of surface recrystallization, Figure 6.8. The η phase had a platelet or globular morphology that formed at various angles with respect to the specimen surface.

Several studies have examined the influence of the η phase on the mechanical properties of Ni-base superalloys, with contradictory results [167, 170, 171]. Platelets of η have been

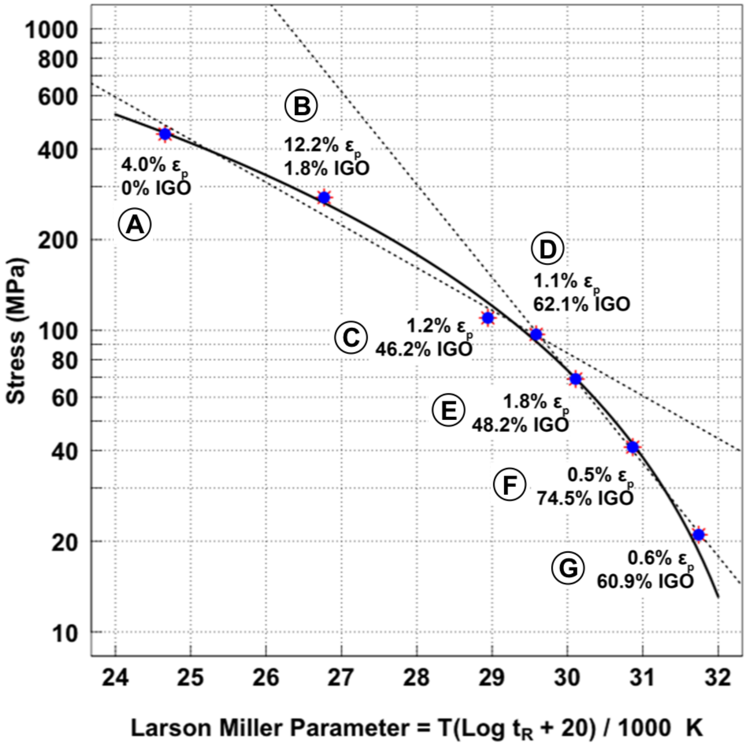

Figure 6.7: Larson-Miller plot for GTD444(CG); creep tests were performed transverse to the growth direction. Each specimen is labeled by an identifying letter, the rupture strain, and fraction of visible intergranular oxidation on the fracture surface.

shown to cause a loss of creep rupture ductility and cracking in conventionally cast PC IN901 [171]. However, in CG alloys such as GTD111, the η phase had no noticeable effect on properties [167]. Creep tests performed on IN740 at 760 °C and 35 MPa for 20,000 h determined that a small amount of the η phase near the grain boundaries did not affect the creep performance [170]. Some researchers have even shown that the η phase may increase creep resistance in Fe-Ni alloys and Udimet 720Li [172, 173]. Clearly the influence of the η phase on the mechanical properties is complex and depends on a number of factors, such as the morphology, location in the microstructure, and loading conditions.

In the case of GTD444(CG), η precipitates were not associated with crack or cavity formation and growth. Platelets of η were only observed near the surface and were typically 50 μm in length, as shown in Figure 6.9. Oxidation was observed on the fracture surface of Specimen E and along high angle grain boundaries away from the primary fracture site, Figure 6.9. Based on the lack of damage associated with the η phase, it appears to have a limited influence on creep properties. However, being hard particles, the η platelets may crack during fatigue loading.

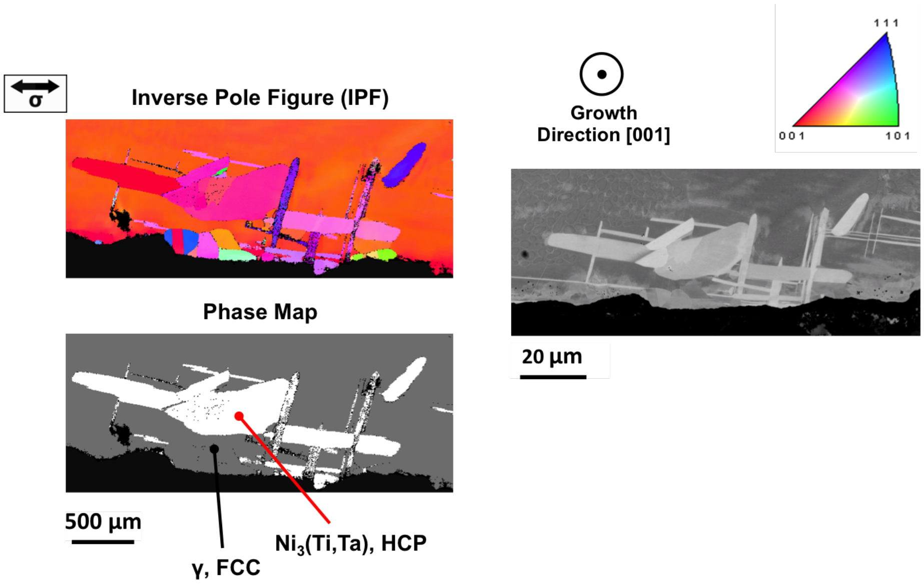

Figure 6.8: EBSD scans and backscattered electron images of a surface region containing the η phase in Specimen E. An inverse pole figure (top left) with respect to the growth direction shows a region of surface recrystallization and a phase map (bottom left) colors the HCP η phase white.

The results of this investigation point to oxidation controlling the transverse creep rupture life during low stress creep tests, where the specimen is exposed to high temperatures for an extended period of time. Recent work by Suave, *et al.* on CG DS200 + Hf specimens

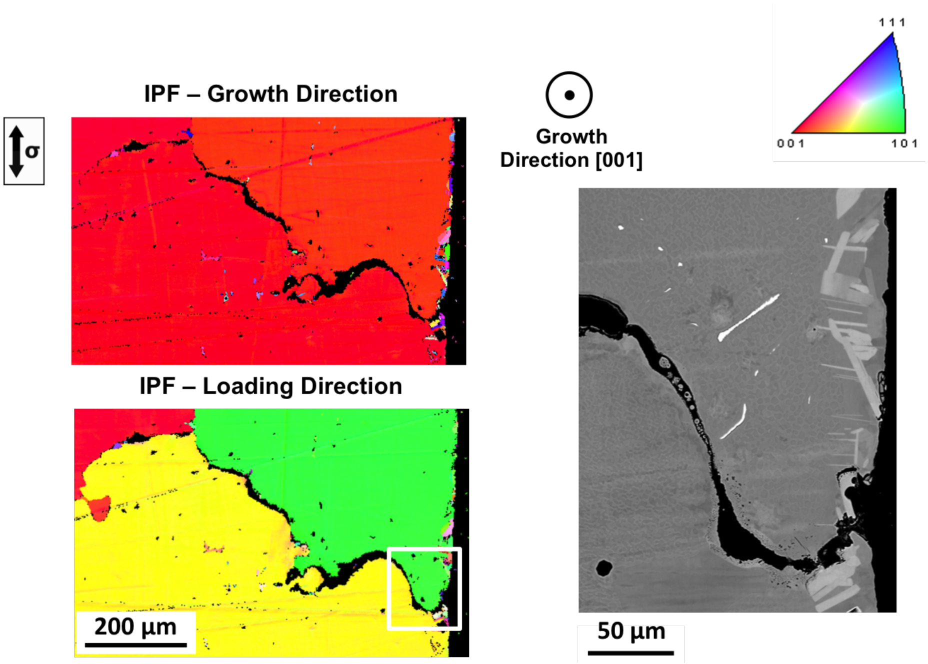

Figure 6.9: Additional EBSD scans from Specimen E were collected away from the fracture surface to show that damage is concentrated near grain boundaries rather than the η platelets. Inverse pole figure maps with respect to both the growth direction (top left) and loading direction (bottom left) indicate the presence of a crack on a high angle twist boundary.

crept transverse to the growth direction above 900 °C at 350 MPa also reported intergranular failure controlled by oxidation [174]. Surface oxidation of the specimen during testing depletes the surface of aluminum leading to the precipitation of η. Thermo-Calc was used to determine the influence of decreasing the aluminum content on the stability of the η phase. The resulting calculated phase diagram, using the composition of GTD444(CG) listed previously in Table 1.1, is shown in Figure 6.10. The creep testing temperatures for all seven specimens are indicated along with the initial aluminum concentration of approximately 9 at%. Each phase of interest has been labeled along with the calculated volume fraction at a point in each phase field. The additional phase field lines in Figure 6.10 correspond to minor carbide, boride and TCP phases below 1% vol. fraction and are not included for this analysis.

At the initial Al/Ti ratio, η is not thermodynamically stable for the range of creep testing temperatures used. However, η is predicted to form once the aluminum concentration drops below a critical value depending on the test temperature, confirming the experimentally inferred oxidation-driven precipitation of η. It is interesting to note that the calculated phase diagram also correctly predicts the η free region directly at the specimen surface, as shown in Figure 6.9, for Specimen E.

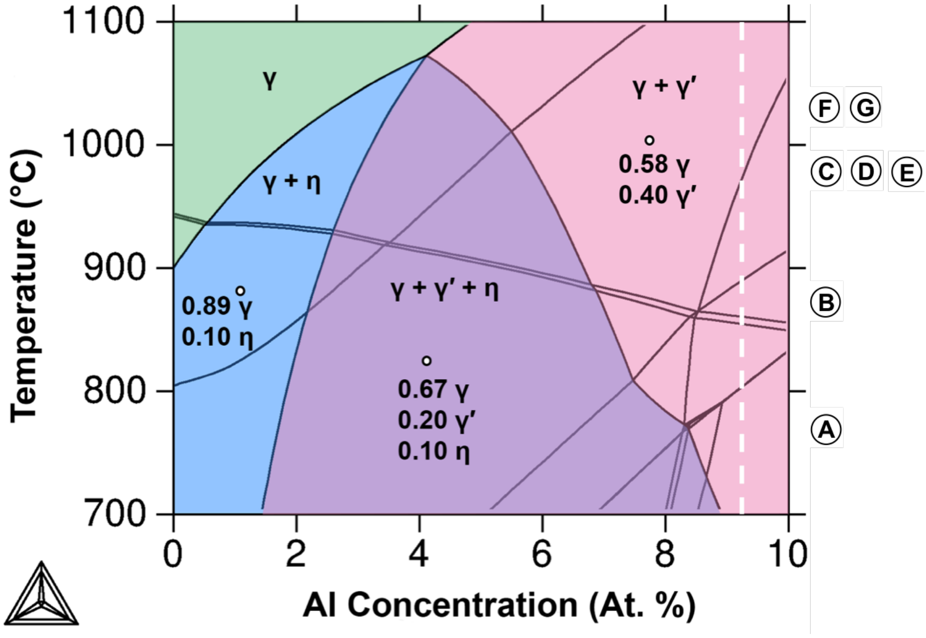

Figure 6.10: Calculated phase digram of GTD444(CG) using Thermo-Calc. The creep test temperature for each specimen is indicated on the righthand side of the plot. Additionally, the white dashed line shows the initial concentration of Al in GTD444(CG). Extra phase field lines correspond to minor phases below 1% volume fraction.

Besides carbide decomposition, the precipitation of additional phases occurs after long term high temperature exposure. Third generation superalloys, heavily alloyed with Re, readily form TCP phases while coatings promote TCP phase formation in second generation alloys such as René N5(SX), as reported in Section 5.3. The formation of TCP phases can be controlled by modifying alloy composition, with Ru being shown to reduce the susceptibility to TCP formation [175–177]. Modification to the coating chemistry and method of application have also helped suppress TCP precipitation [2].

6.2.4 Conclusions

The discussion of the rejuvenation limiting factors up to this point in this section prompts the question: is full recovery possible in Ni-base superalloys? For GTD444(CG) and René N5(SX), rejuvenation was limited primarily by transverse grain boundaries inherent to the microstructure or due to recrystallization. Examination of long term GTD444(CG) creep specimens revealed that carbide decomposition and oxidation led to the precipitation of the η phase but it did not influence creep performance. Rather, intergranular oxidation controlled the transverse creep rupture life below a critical stress at creep conditions more comparable to service. The controlling failure mechanism in GTD444(CG) clearly depends on the creep testing conditions, and the direction of loading with respect to the solidification direction, with oxidation playing a prominent role rather than carbide decomposition. Based on the observed failure mechanisms, full recovery of GTD444(CG) creep properties will not be possible using a solution + aging heat treatment due to the irreversibility of oxidation, recrystallization, and the inherent grain structure. Using HIP is likely to provide only a marginal benefit in creep performance depending on the loading conditions, as oxidized cracks can not be healed.

Multiple rejuvenation of René N5(SX) was experimentally shown to be successful based on an overall extension of total creep rupture life and recovery of 80% of initial time to the creep strain threshold, as mentioned in Chapter 5. This appears to be a result of the more creep resistant initial microstructure and the initial absence of any high angle grain boundaries, when compared to GTD444(CG). The formation of TCP phases and crystal misorientation are potential life limiting factors of René N5(SX), but rejuvenation will still be successful relative to the initial creep performance of the defective specimen. Rejuvenation of fatigue damage caused by surface cracks was also successful, however, internal crack growth initiating at solidification porosity during fatigue testing was not examined as part of this thesis work. Such damage will not be repaired using only a solution + aging rejuvenation heat treatment for both GTD444(CG) and René N5(SX). HIP has been shown to decrease pore size, improving creep and fatigue performance, however, the downside of potentially causing recrystallization and the additional cost must be taken into account. The use of LMC rather than Bridgman casting is another way to improve mechanical properties but will also increase production costs.

While rejuvenation of René N5(SX) was considered successful, full recovery of the creep performance was not attainable even with a solution heat treatment at the γ' solvus. Similar results are expected for GTD444(CG) although rejuvenation heat treatments were only performed below the γ' solvus temperature. This is likely a result of the low initial dislocation density, heterogenous deformation due to stress concentrators in the microstructure, and the inherent recovery mechanisms. As mentioned in Section 1.4.1, during recovery, the stored energy of the material is reduced by the movement of dislocations, resulting in annihilation and rearrangement into lower energy configurations. Pure single crystals of hexagonal close-packed and cubic metals deforming on a single slip system can have their initial mechanical properties and microstructure fully recovered during annealing [178–180]. For Ni-base superalloys, however, full recovery without recrystallization is not possible. This is due to dislocation interactions and extensive crystal rotation near stress concentrators, producing excess dislocations of one sign that cannot be removed by annihilation [24]. The hold-time fatigue behavior of René N5(SX) appears to be less influenced by the existing dislocation substructure, as mentioned in Section 5.4, however due to the limited number of tests and experimental scatter, additional work is required to confirm this observation.

Chapter 7

A Method for Nondestructively Detecting Rejuvenation-Limiting Microstructural Features

This chapter will present a detailed discussion on the fundamentals enabling RUS to be used as a non-destructive evaluation (NDE) technique, followed by a discussion of the experimental results. Resonant ultrasound spectroscopy (RUS) was successfully implemented as a part of a multiple rejuvenation testing procedure to detect recrystallization, as mentioned in Chapter 5. To verify that the RUS results have been correctly interpreted, a finite element (FE) model has also been developed to predict the influence of recrystallization on the resonance frequencies of shot peened and heat treated creep specimens.

7.1 Resonant Ultrasound Spectroscopy

RUS falls under a broad category commonly referred to as ultrasonics, or acoustics when the frequencies of mechanical resonance fall within audible limits. In RUS, resonance modes are excited by piezoelectric transducers that provide a periodic displacement to the surface of the specimen, causing standing elastic waves to develop that constructively interfere and produce amplified deflections [181–185]. These amplified deflections are then recorded across a range of frequencies by additional piezoelectric transducers contacting the specimen to yield a broadband resonance spectrum when plotted as a function of the excitation frequency [181–185]. From peaks in the broadband measurement, resonance frequencies are deduced that are characteristic of the geometry and the material properties of the specimen [181–185]. Furthermore, there are different modes of resonance (i.e. longitudinal, bending, and torsional) that may be more or less sensitive to different types of damage and its location.

7.1.1 Elasticity Considerations

Elastic waves excited in the specimen during RUS inspection are low-energy and generate very small sample deflections such that the assumption of linear elasticity is appropriate. The 3D constitutive law relating stresses (σ_{ij}) and strains (ϵ_{kl}) is Hooke's law, given as:

$$\sigma_{ij} = C_{ijkl}\epsilon_{kl}, \tag{7.1}$$

where C_{ijkl} is the fourth-order stiffness tensor. Voigt shorthand maps the C_{ijkl} of the fourth-order tensor to a 6-by-6 matrix ($C_{ijkl} \rightarrow C_{pq}$).

The two constituent phases of Ni-base superalloy single crystals, γ and γ', possess cubic crystal structures, affording the material cubic elastic symmetry. Cubic symmetry materials are fully defined by 3 independent stiffness values, C_{11}, C_{12}, and C_{44} [183].

An important characteristic for RUS inspection of grain structure is the elastic anisotropy of the material, which is commonly defined for a cubic crystal by the Zener anisotropy ratio [186]:

$$A = \frac{2C_{44}}{C_{11} - C_{12}}. \tag{7.2}$$

Metals with low elastic anisotropy include Al and W with $A_{Al} \approx 1.2$ and $A_W \approx 1.0$, while Ni, Fe, and Cu exhibit significant anisotropy with anisotropy ratios ranging from 2.4 – 3.2 [187]. Table 7.1 provides the stiffness values and calculated A for CMSX-4 [188], a Ni-base superalloy with similar composition and properties to the alloy employed in this study, René N5(SX).

Table 7.1: Single crystal stiffness values for CMSX-4, a single crystal Ni-base superalloy similar in composition to René N5(SX), data from Sieborger, *et al.* [188].

Stiffness	**Value (units)**
C_{11}	252 GPa
C_{12}	161 GPa
C_{44}	131 GPa
A	2.88 unitless

7.1.2 Influence of Recrystallization on Resonance

As a direct result of elastic anisotropy, a single crystal casting will exhibit different resonance characteristics as compared to a polycrystalline casting of the same material, with larger anisotropy leading to greater divergence of resonance characteristics. Conversely, a material with an $A = 1$ would resonate irrespective of grain structure and would not be a candidate material for the detection of recrystallization with RUS.

René N5(SX) is most compliant to normal stresses along $\langle 100 \rangle$ directions, and least compliant to shear on $\{100\}$ planes. Refer to Table 7.2 for the calculated directional elastic moduli values for CMSX-4, a superalloy with similar composition to René N5(SX).

Table 7.2: Directional elastic moduli for single-crystal CMSX-4 specimens, calculated with data from Sieborger, *et al.* [188].

Directional Moduli	**Value (units)**
$E_{[100]}$	126 GPa
$E_{[110]}$	231 GPa
$E_{[111]}$	320 GPa
$G_{\{100\}<\perp>}$	131 GPa
$G_{(110)[1\bar{1}0]}$	45.5 GPa
$G_{(110)[001]}$	131 GPa
$G_{\{111\}<\perp>}$	58.1 GPa

As a [001] single crystal undergoes recrystallization, the recrystallized grains will have an orientation different than the parent material that is stiffer to normal loads, and will be more compliant to shear loading. The consequence of this is that resonance modes involving dilational or extensional motion (bending modes) will encounter a higher stiffness according to the following relation:

$$f_R \propto \sqrt{\frac{E}{\rho}} \tag{7.3}$$

whereby the resonance frequency (f_R) increases. Similarly, resonance modes dominated by shear or torsional motions (torsional modes) will encounter a lower stiffness (G in place of E above), and should exhibit a decrease in f_R.

Ultimately, the goal of using RUS coupled with FE models is to establish a NDE framework for characterizing and monitoring particular resonant modes of a geometrically complex single crystal specimen that contains grain defects, based on the fundamental principles outlined above. Results of using RUS during multiple rejuvenation testing will be discussed in the next section.

7.2 Experimental RUS Results from Multiple Rejuvenation Testing

RUS measurements were collected using an apparatus manufactured by Vibrant NDT Corporation, shown in Figure 2.7 and discussed previously in Section 2.3.1. ASTM standard E2534-15 also discusses the use of RUS setups. Based on the expected behavior of recrystallization on resonance and to simplify the analysis, three reliably measured resonant bending modes were selected and tracked during multiple rejuvenation testing. The tracked modes correspond to FE-model-informed mode numbers 9-10, 11-12, and 13-14. These were selected out of the 50 total modes for the frequency scan range of 1-200 kHz. Only the f_R are monitored with a focus on the evolution of mode-specific changes in f_R

(Δf_R), defined as:

$$\Delta f_R = \frac{f_R^{\text{new condition}} - f_R^{\text{previous condition}}}{f_R^{\text{previous condition}}} * 100\% \tag{7.4}$$

Scans were collected before and after each creep test and rejuvenation heat treatment, as illustrated in Figure 4.7.

Bending modes occur in pairs that theoretically resonate at the same frequency. However, resonance is highly degenerate and, due to asymmetry in the resonating creep specimen, peak splitting occurs [189]. Additionally, in some RUS scans, only a single bending mode was measured experimentally rather than a pair due to weak coupling between the sample and the transducers, or a neighboring high-amplitude peak. Due to these issues, each bending mode pair (9-10, 11-12, and 13-14) was averaged from three separate RUS scans.

The accuracy and precision of the technique is on the order of a tenth of a percent of the resonance frequency, corresponding to a frequency variation of approximately 10-30 Hz [135]. The variability is primarily due to specimen placement on the transducers. Additionally, the amplitudes of the resonance peaks can vary by an order of magnitude, a consequence of the specimen deflecting off the transducers during resonance. For this reason, analysis of the full peak width at half height and subsequent quality factor calculations were not performed. Four representative RUS scans are shown in Figure 7.1 for an as-machined René N5(SX) specimen of the same design as the creep specimens used for mechanical testing, as shown earlier in Figure 2.1a.

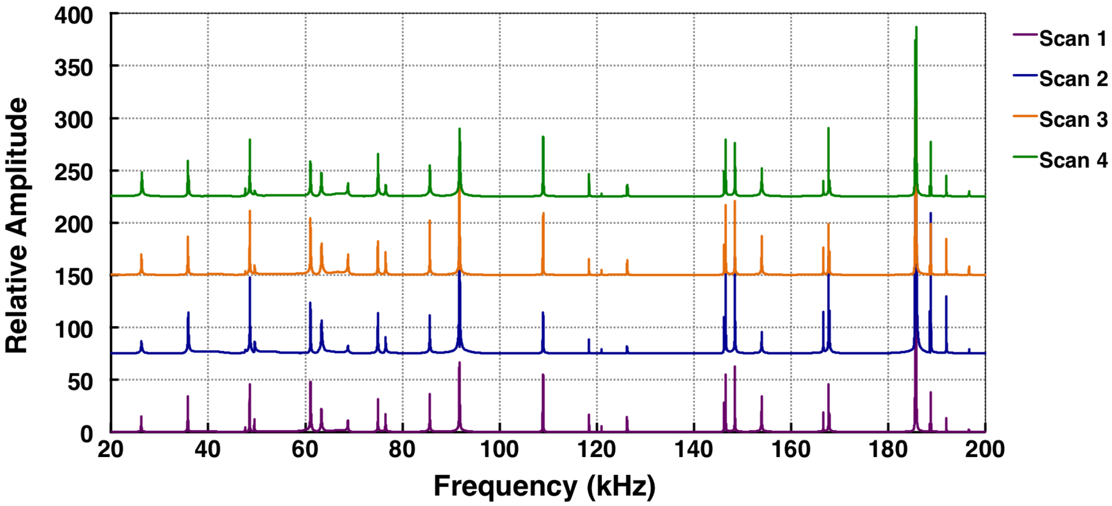

Figure 7.1: Four broadband resonance scans collected from 20-200 kHz for a single René N5(SX) creep specimen in the as-machined condition. The measured amplitudes are not repeatable with the RUS setup as configured. Amplitudes are plotted in arbitrary units with the scans offset for clarity.

The mode number and Δf_R due to each creep test and rejuvenation heat treatment performed during the multiple rejuvenation tests discussed in Chapter 5 are listed in Tables 7.3 and 7.4. The influence of creep deformation on the Δf_R is evident by constructing a box plot of all experimentally measured points from the three sets of bending mode pairs for both GTD444(CG) and René N5(SX) , as shown in Figure 7.2a. A linear regression fit to the data indicates that up to 5% creep strain there is an inverse linear relationship between Δf_R and creep strain. This is a result of specimen elongation and the corresponding increase in the wavelength and decrease in resonance frequency due to the inverse relationship between

Table 7.3: This table lists the normalized percent change in f_R (Δf_R) of the analyzed bending modes collected from multiple rejuvenation creep specimens. Scans were analyzed from before and after the indicated creep test number for each corresponding multiple rejuvenation test.

		Δf_R (%)									
Test Number	Mode Number	CT1	CT2	CT3	CT4	CT5	CT6	CT7	CT8	CT9	CT10
444-14-1	9-10	−0.64	−0.37	−0.81	−0.72	−0.94	−0.57	-	-	-	-
	11-12	−0.60	−0.62	−0.64	−0.67	−0.70	−0.69	-	-	-	-
	13-14	−0.77	−0.87	−0.72	−0.90	−0.92	−0.96	-	-	-	-
444-14-2a	9-10	−1.14	−1.58	-	-	-	-	-	-	-	-
	11-12	−1.29	−1.46	-	-	-	-	-	-	-	-
	13-14	−1.72	−1.64	-	-	-	-	-	-	-	-
444-14-2b	9-10	−1.62	−1.50	-	-	-	-	-	-	-	-
	11-12	−1.65	−1.61	-	-	-	-	-	-	-	-
	13-14	−1.91	−1.92	-	-	-	-	-	-	-	-
444-14-3	9-10	−2.65	−3.20	-	-	-	-	-	-	-	-
	11-12	−2.44	−2.59	-	-	-	-	-	-	-	-
	13-14	−3.03	−2.83	-	-	-	-	-	-	-	-
N5-FS-2	9-10	−1.97	−1.08	−1.76	−2.32	-	-	-	-	-	-
	11-12	−1.28	−1.43	−1.31	−1.47	-	-	-	-	-	-
	13-14	−1.60	−1.89	−1.65	−1.82	-	-	-	-	-	-
N5-28-2	9-10	−2.22	−1.33	−1.36	−1.71	−1.51	−1.45	-	-	-	-
	11-12	−1.22	−1.33	−1.34	−1.52	−1.42	−1.36	-	-	-	-
	13-14	−1.53	−1.69	−1.70	−1.90	−1.80	−1.78	-	-	-	-
N5-56-2	9-10	−2.03	−1.60	−1.43	−1.23	−1.78	−1.89	−1.88	−2.03	−1.78	−1.53
	11-12	−1.41	−1.33	−1.58	−1.40	−1.28	−1.42	−1.32	−1.43	−1.46	−1.51
	13-14	−1.81	−1.88	−1.98	−1.91	−1.88	−1.74	−1.73	−2.13	−1.74	−1.78
N5-28-3	9-10	−2.86	−1.87	−2.26	−3.01	−2.77	-	-	-	-	-
	11-12	−2.25	−2.15	−2.21	−2.18	−2.13	-	-	-	-	-
	13-14	−2.77	−2.78	−2.88	−2.77	−2.58	-	-	-	-	-
N5-28-5	9-10	−3.06	−3.78	-	-	-	-	-	-	-	-
	11-12	−3.10	−3.28	-	-	-	-	-	-	-	-
	13-14	−4.13	−4.14	-	-	-	-	-	-	-	-
N5-28-2-CT	9-10	−0.61	−0.77	−1.03	−1.34	−1.11	−1.07	-	-	-	-
	11-12	−0.68	−0.79	−0.68	−1.07	−0.72	−0.91	-	-	-	-
	13-14	−0.81	−1.05	−0.98	−1.35	−0.95	−1.12	-	-	-	-

Table 7.4: This table lists the normalized percent change in f_R (Δf_R) of the analyzed bending modes collected from multiple rejuvenation creep specimens. Scans were analyzed from before and after each rejuvenation heat treatment.

Test Number	Mode Number	Δf_R (%)									
		Baseline	HT1	HT2	HT3	HT4	HT5	HT6	HT7	HT8	HT9
444-14-1	9-10	0.57	−0.32	−0.08	−0.45	0.05	−0.35	−0.03	-	-	-
	11-12	0.51	−0.29	−0.13	−0.26	−0.13	−0.19	−0.17	-	-	-
	13-14	0.51	−0.34	−0.15	−0.18	−0.12	−0.13	−0.11	-	-	-
444-14-2a	9-10	0.15	−0.08	0.91	-	-	-	-	-	-	-
	11-12	0.28	−0.18	1.11	-	-	-	-	-	-	-
	13-14	0.32	−0.11	0.02	-	-	-	-	-	-	-
444-14-2b	9-10	0.21	0.02	0.43	-	-	-	-	-	-	-
	11-12	0.48	−0.09	0.53	-	-	-	-	-	-	-
	13-14	0.43	−0.23	−0.11	-	-	-	-	-	-	-
444-14-3	9-10	0.46	0.61	2.81	-	-	-	-	-	-	-
	11-12	0.62	−0.02	3.65	-	-	-	-	-	-	-
	13-14	0.59	−0.16	2.86	-	-	-	-	-	-	-
N5-FS-2	9-10	0.30	−0.47	−0.38	0.08	9.18	-	-	-	-	-
	11-12	0.30	−0.42	−0.38	−0.18	7.43	-	-	-	-	-
	13-14	0.36	−0.44	−0.28	−0.26	7.94	-	-	-	-	-
N5-28-2	9-10	0.99	−0.24	−0.57	−0.06	−0.41	−0.30	5.27	-	-	-
	11-12	0.32	−0.40	−0.29	−0.21	−0.25	−0.14	3.89	-	-	-
	13-14	0.18	−0.35	−0.26	−0.18	−0.39	−0.21	5.48	-	-	-
N5-56-2	9-10	0.67	0.25	−0.49	−0.47	−0.21	−0.09	0.09	0.17	−0.22	0.27
	11-12	0.25	−0.11	−0.17	−0.11	−0.20	−0.23	−0.21	−0.08	−0.25	0.17
	13-14	0.22	−0.09	−0.03	−0.04	−0.09	−0.04	−0.15	0.28	−0.35	0.15
N5-28-3	9-10	1.79	−0.89	−0.92	−0.11	0.14	7.94	-	-	-	-
	11-12	0.59	−0.39	−0.38	−0.18	−0.30	5.48	-	-	-	-
	13-14	0.49	−0.34	−0.29	−0.15	−0.28	6.66	-	-	-	-
N5-28-5	9-10	0.72	−0.25	1.86	-	-	-	-	-	-	-
	11-12	0.23	−0.11	1.18	-	-	-	-	-	-	-
	13-14	0.20	−0.25	1.75	-	-	-	-	-	-	-
N5-28-2-CT	9-10	−0.60	−0.93	−1.01	−0.39	−0.44	−0.66	−0.83	-	-	-
	11-12	−0.18	−0.74	−0.92	−0.86	−0.72	−0.83	−0.63	-	-	-
	13-14	−0.08	−0.89	−1.01	−0.96	−0.86	−1.06	−0.86	-	-	-

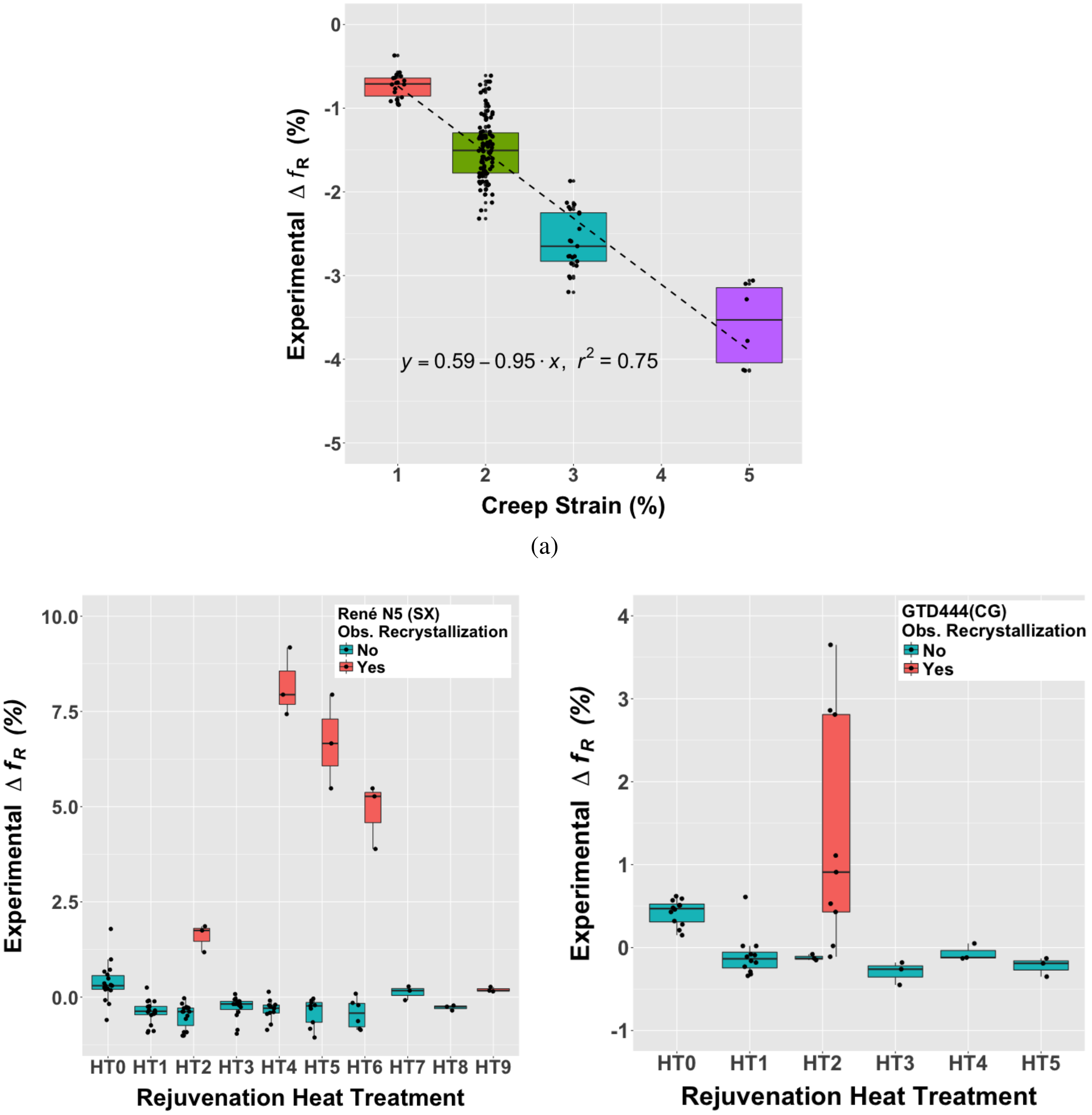

(a)

(b)

(c)

Figure 7.2: Box plots showing the experimentally measured Δf_R due to a) creep deformation, and rejuvenation heat treatments of b) René N5(SX) and c) GTD444(CG). The box plots show a rectangle that spans the interquartile range. A black horizontal line inside the rectangle shows the median and each measurement is plotted showing the minimum and maximum values. Each heat treatment is labeled with the baseline corresponding to HT0.

wavelength and resonance frequency. The bending mode pairs were analyzed collectively because they each supported the inverse linear relationship with r^2 values of between 0.6 and 0.8. The dominant influence of specimen elongation on the Δf_R makes it difficult to use RUS to determine the presence of cracks and cavities non-destructively at low creep strains, because they would also result in a decrease in the resonance frequency by reducing the specimen's effective elastic modulus.

However, RUS was successful in non-destructively detecting the presence of recrystallization. Box plots of René N5(SX) and GTD444(CG) (Figures 7.2b and 7.2c, respectively) indicate a statistically significant difference in the Δf_R due to the final rejuvenation heat treatment before failure of several multiple rejuvenation creep tests, as discussed previously in Chapter 5. It was later confirmed via metallographic examination that recrystallization was present in these specimens. The average Δf_R from the rejuvenation heat treatment that caused significant recrystallization was 4.31% ± 3.19% and 1.36% ± 1.31% for René N5(SX) and GTD444(CG), respectively. René N5(SX) showed a more significant Δf_R when compared to GTD444(CG) due to the inherent differences in grain structure between a SX and a CG material. A CG creep specimen will, on average, have several grains through thickness and contain high angle twist boundaries, resulting in a higher baseline elastic modulus. Thus, recrystallization will have a less significant influence on the elastic properties when compared to a well-aligned single crystal. Furthermore, recrystallization in a single crystal specimen was observed to consume a majority of the reduced gauge section. The same could not be said for recrystallization in GTD444(CG), which was more limited. One René N5(SX) multiple rejuvenation specimen that was interrupted before complete rupture did not display a statistically significant Δf_R but limited surface recrystallization was present. This result indicates that the RUS technique is detecting recrystallization only after a critical volume fraction of recrystallized material has been reached, assuming a random orientation of recrystallized nuclei. Thus, RUS did not detect the onset of recrystallization but rather the onset of a statistically significant change in the elastic properties resulting from catastrophic levels of recrystallization. The presence of detectable levels of recrystallization always resulted in abrupt specimen rupture during multiple rejuvenation creep testing.

The typical Δf_R from a rejuvenation heat treatment was low and negative at approximately -0.226% ± 0.456% and 0.040% ± 0.31% for René N5(SX) and GTD444(CG), respectively. The negative Δf_R was believed to be a result of the reduction of mixed oxides during the rejuvenation heat treatment, which was performed in a 5% H_2/Ar environment, causing a mass change. The baseline heat treatment, displayed at HT0 in Figures 7.2b and 7.2c, showed the greatest scatter in Δf_R between the three pairs of bending modes and from specimen to specimen. This may be a result of the relaxation of residual stress imparted on the specimens during machining.

In summary, there is strong evidence that RUS can be used to detect recrystallization, however, detecting other forms of creep damage will be difficult if not impossible at the creep strains of interest due to significant geometry change during mechanical testing. To verify and further investigate the use of RUS to detect recrystallization, specifically focusing on the influence of the volume fraction of recrystallized material, a more controlled experiment was performed involving the heat treatment of shot peened creep specimens. A finite element (FE) model was also developed by Brent Goodlet of the University of California, Santa Barbara to corroborate the experimentally observed Δf_R.

7.3 Verifying the Use of RUS to Detect Recrystallization

Shot peening was performed at GE Power on the reduced gauge section and fillets of creep specimens using two different gas pressures. Full coverage was obtained by using a custom fixture and rotating the specimen between passes as shown in Figure 7.3. One specimen was shot peened using standard conditions and will be referred to henceforth as Specimen Low-Pressure (LP), while the other specimen was shot peened at double the typical pressure and will be referred to as Specimen High-Pressure (HP). There was a negligible change in the diameter of the specimens as a result of shot peening. To induce recrystallization, heat treatments were performed at the γ' solvus temperature for several hours in a reducing atmosphere to avoid surface oxidation and minimize mass change.

RUS scans were collected from Specimen LP and Specimen HP in the as-machined (baseline), shot peened, and shot peened + solution heat treated conditions. f_R were measured for each condition, allowing for mode-specific resonance frequency shifts (Δf_R) to be determined as a result of shot peening and shot peening + solution heat treatment. After collecting RUS spectra, Specimen LP and Specimen HP were sectioned longitudinally along the [001] growth direction and prepared for metallographic examination.

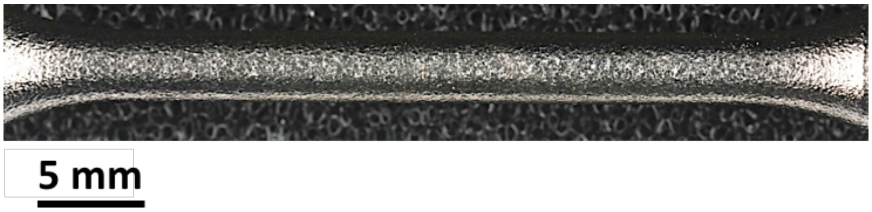

Figure 7.3: High magnification optical image of a machined specimen after shot peening.

7.3.1 Modeling Resonance using Finite Element Analysis

Finite element methods are particularly useful for modeling resonance in samples with complex geometries such as the mechanical test specimen detailed in Figure 2.1a. Using ABAQUS CAE 6.12 [190], this specimen was discretized and the governing physics and material properties applied. The virgin specimen model was comprised of approximately 200,000 linear hexahedral (C3D8R) and wedge (C3D6) elements that were assigned single crystal elastic properties [190], Table 7.1, and a global material orientation such that the long axis of the specimen was parallel to the [001] crystallographic direction. Once the modeled specimen was fully defined, the 50 first (lowest frequency) resonance modes were determined by the ABAQUS Lanczos Eigen frequency solver. The modeling was conducted on a 64-bit desktop computer with 3.4 GHz processor and 20 GB RAM. The model output provided exaggerated depictions of the resonance mode deflection character, Figure 7.4, that allowed each mode to be classified as one of four distinct mode types: longitudinal bending, torsional, extensional, or transverse bending. Along with the deflection character, the model described above outputs a list of f_R that establish the baseline response of a virgin specimen before shot peening or recrystallization. At this point in the model development process it is important to ensure that the FE modeled and RUS measured f_R agree to within approximately ±1% for each mode [191]. Mode-order and periodicity should match well enough that measured and modeled modes can be matched over a majority of the broadband, herein considered the first 50 modes, while an eventual NDE protocol would likely focus on a subset of 10 – 15 modes that are found to be the most diagnostic of the resonance-affecting mechanism of interest [191].

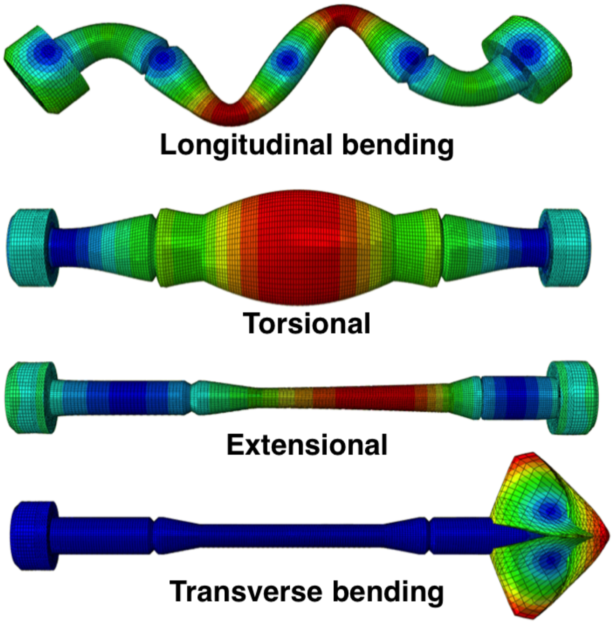

Figure 7.4: Depiction of the four distinct mode types that occur within in first 50 resonances predicted by the FE model. The shape of these modes, i.e., deflection character, is visualized by depicting the deflections in a highly exaggerated manner, while the actual deflections of a sample are minuscule. Image courtesy of Brent Goodlet.

7.3.1.1 Modeling Recrystallization

Due to the significant elastic anisotropy of René N5(SX) ($A = 2.88$), Gairola and Kröner's third-order averaging scheme [192] is used to calculate self-consistent isotropic moduli for representing polycrystalline René N5(SX). This homogenization procedure assumes that the recrystallized material will have a random grain orientation distribution consistent with Nygårds' analysis [193]. Table 7.5 summarizes the material properties used for modeling recrystallized René N5(SX). These properties are applied to elements along the gauge and fillet sections of the creep specimen, Figure 7.5, at depths of 80, 100, 178, 200, and 1500+ μm, the latter corresponding to full recrystallization of the 3.06 mm diameter gauge and fillet.

Table 7.5: Material properties utilized in the FE model to represent René N5(SX). Isotropic polycrystalline moduli are calculated from the stiffness data detailed previously [188], while the density (ρ) reported in [2] is the same for both alloys.

Property	**Value (units)**
K	191 GPa
E_{GK}	226 GPa
G_{GK}	86.8 GPa
ν_{GK}	0.303
ρ	8700 kg/m^3

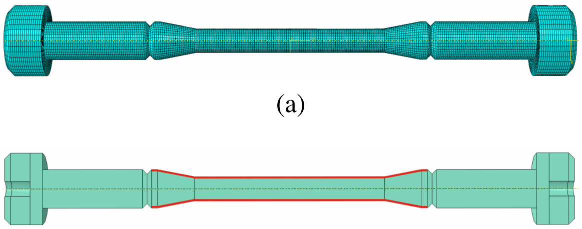
(a)

(b)

Figure 7.5: Creep specimen model depicting a) the finite element mesh and b) a cross sectional view of the sample with the red region along the surface of the gauge and fillets indicating a 200 μm layer of recrystallization. Image courtesy of Brent Goodlet.

7.4 Resonant Ultrasound Spectroscopy Measurements

Baseline RUS scans were collected of both Specimen LP and Specimen HP in the as-machined condition. Similar to the NDE performed during multiple rejuvenation testing, only the f_R are monitored with a focus on the evolution of mode-specific changes in f_R. Using the baseline scans and the model-informed mode type information, 10-15 reliably-measured resonance modes were typically chosen to track and compare as the specimens were shot peened and heat treated. The mode number, mode type, and f_R are listed in Tables 7.6 and 7.7 for the shot peened specimens investigated here.

The Δf_R after low pressure shot peening was negative across all mode numbers tracked with an average shift of -0.127$\%$ ± 0.046$\%$. After high pressure shot peening (double the pressure) an average shift of -0.251$\%$ ± 0.089$\%$ was measured. While transmission electron microscopy studies were beyond the scope of this study, the Δf_R follows well with the established theory that imparting dislocations into the material from processes such as shot peening will decrease the apparent modulus [194–196]. Following the solution heat treatment, an order of magnitude higher average positive shifts of 1.835% ± 1.704%, and 2.380% ± 2.910% were calculated for Specimen LP and Specimen HP, respectively.

Microscopy revealed that both Specimen LP and Specimen HP recrystallized following solution heat treatment, as shown in Figure 7.6. This recrystallization was responsible for the measured Δf_R following heat treatment. The depth of recrystallization was 80.0 μm ± 15.6 μm and 177.9 μm ± 27.2 μm for Specimen LP and Specimen HP, respectively. A minimum of 250 measurements of the recrystallized depth were taken, with each measurement spaced ~20 μm along the surface of each specimen. Recrystallized grains contained cuboidal γ' precipitates that nucleated and grew during controlled cooling from the full solvus temperature, as shown in Figure 7.7.

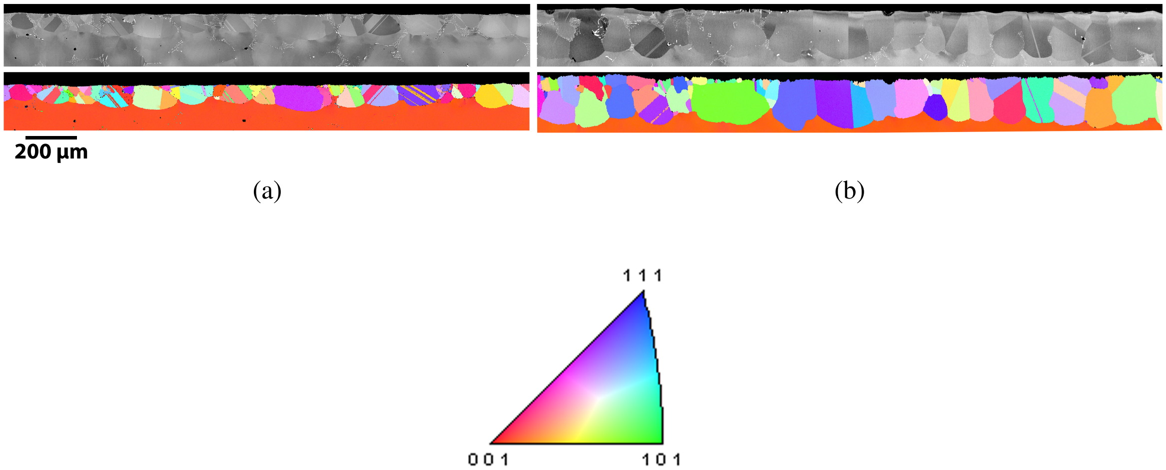

(a) (b)

Figure 7.6: Backscattered electron images (top row) of specimens subjected to a heat treatment following shot peening at a) a low and b) high pressure show the varying depth of the recrystallized surface region. Electron backscatter diffraction (bottom row) was used to collect inverse pole figure maps of the same location showing the orientation at every point with respect to the long axis of the creep specimens.

Table 7.6: Resonance frequencies (kHz) of the analyzed mode numbers for the low pressure (Specimen LP) shot peened specimen in the as-machined, shot peened, and heat treated conditions. The mode type (torsional (T), longitudinal bending (B), or extensional (E)) of each resonance number and percent change relative to the prior condition are also listed. The modeled percent change used the experimentally measured recrystallization depth of 80.0 μm.

Specimen LP							
		Resonance frequency (kHz)					
Mode Number	Mode Type	As-Machined	Low Pressure Shot Peened	% Change	Solution Heat Treated	% Change	Modeled % Change
13	B	35.82	35.79	−0.078	37.012	3.325	2.84
14	B	35.93	-	-	37.121	3.326	2.84
27	B	91.69	91.53	−0.177	94.466	3.026	2.44
28	B	91.80	91.63	−0.190	94.582	3.025	2.44
29	B	108.87	108.70	−0.158	111.726	2.619	2.15
30	B	108.99	108.81	−0.164	111.878	2.647	2.15
33	B	126.22	126.03	−0.154	129.730	2.778	2.63
34	B	126.33	126.13	−0.159	129.894	2.818	2.63
32	T	120.95	120.80	−0.128	117.721	−0.589	−1.87
38	T	148.44	148.32	−0.083	151.168	−1.801	−0.75
41	T	166.64	166.47	−0.097	166.082	−0.332	−1.33
22	E	68.77	68.74	−0.045	69.483	1.036	0.81
26	E	85.62	85.55	−0.092	87.324	1.985	1.91

Table 7.7: Resonance frequencies (kHz) of the analyzed mode numbers for the high pressure (Specimen HP) shot peened specimen in the as-machined, shot peened, and heat treated conditions. The mode type (torsional (T), longitudinal bending (B), or extensional (E)) of each resonance number and percent change relative to the prior condition are also listed. The modeled percent change used the experimentally measured recrystallization depth of 177.9 μm.

Specimen HP							
		Resonance frequency (kHz)					
Mode Number	Mode Type	As-Machined	High Pressure Shot Peened	% Change	Solution Heat Treated	% Change	Modeled % Change
13	B	35.61	35.51	−0.272	37.342	4.870	4.80
14	B	35.69	35.57	−0.329	37.429	4.887	4.80
27	B	91.26	90.99	−0.310	95.171	4.268	3.82
28	B	91.33	91.08	−0.279	95.262	4.301	3.82
29	B	108.50	108.18	−0.294	112.454	3.642	3.88
30	B	108.57	108.24	−0.301	112.564	3.684	3.88
33	B	125.79	125.42	−0.299	130.698	3.900	5.37
34	B	125.86	125.47	−0.311	130.819	3.939	5.37
32	T	121.33	120.91	−0.346	115.826	−4.539	−3.70
38	T	154.53	154.32	−0.135	152.138	−1.547	−0.76
41	T	166.50	166.20	−0.178	165.404	−0.656	−2.28
22	E	68.68	68.63	−0.072	69.588	1.320	1.57
26	E	85.37	85.25	−0.137	87.824	2.874	3.98

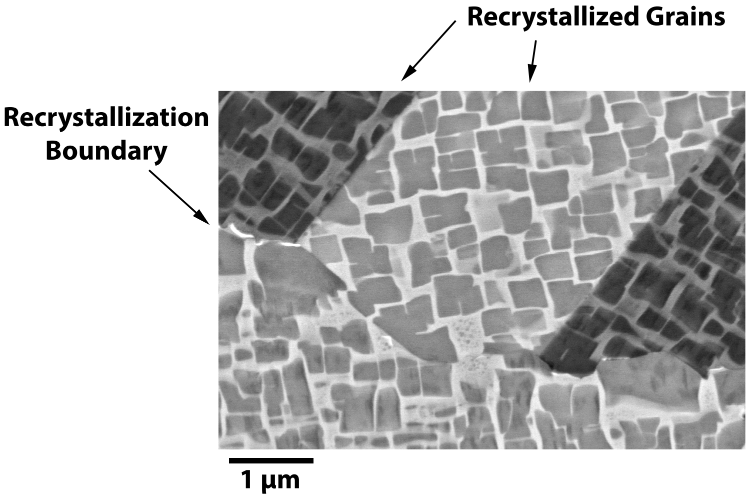

Figure 7.7: Backscattered electron micrograph showing the boundary and the precipitate morphology in the recrystallized grains.

7.5 Finite Element Model Results

The results from the cylindrical sub-volume modeling study comparing the discrete anisotropic grain representation of recrystallization to a homogenized isotropic approach are detailed in Figure 7.8. The fact that the Δf_R predicted by the two representations are similar for the first 50 resonance modes validates the isotropic homogenization procedure. Essentially, the two modeling approaches simulate the same sub-volume of material using two extreme representations. Experimentally observed Δf_R behavior would likely fall between the Δf_R predicted by the relatively coarse 128 discrete grain model and the Δf_R predicted by the isotropic model. Therefore, the disagreement between of the two model results indicates the maximum error introduced by the isotropic assumption for a recrystallization depth of 5% the cylinder radius. This error is very small compared to the magnitude of the Δf_R response resulting from recrystallization, and can therefore be neglected.

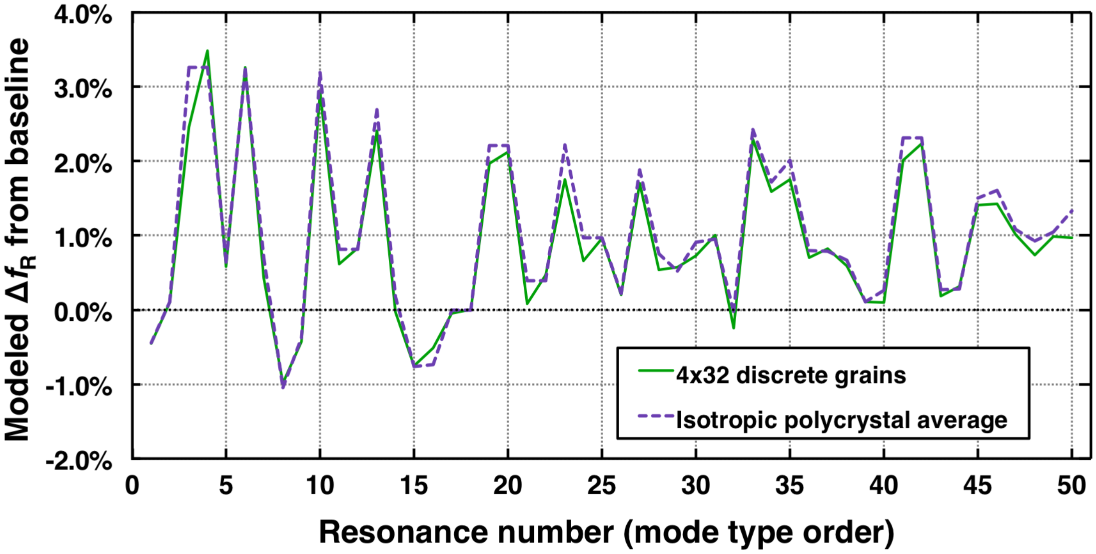

Figure 7.8: Modeled Δf_R for a single crystal cylinder with recrystallization consuming 5% of the radius using two distinct modeling approaches. The agreement between the two model results illustrates that an isotropic homogeneous layer of recrystallized material sufficiently describes the Δf_R response of even coarse aggregates of (4x32) grains, and demonstrates that the isotropic representation is sufficient. Plot courtesy of Brent Goodlet.

Of the four distinct resonance mode types predicted by the FE model of the creep specimen over the frequency range of interest, illustrated in Figure 7.4, 30 of the first 50 resonance modes are longitudinal bending. Due to the nature of bending deflections, longitudinal bending modes are more sensitive to mechanisms that affect stiffness near the surface of the specimen. Plotting the modeled Δf_R due to surface recrystallization for the first 50 resonance modes shows that, as expected, the longitudinal bending modes display a positive Δf_R that increases with the depth of the recrystallized layer, as indicated in Figure 7.9. This result agrees well with the experimental multiple rejuvenation NDE and with the expectation that the recrystallized grains on the surface will be oriented such that their directionally-dependent Young's modulus is greater than the virgin $E_{[100]}$ material that exhibits the minimum $E_{[hkl]}$. Extensional resonance modes behave similarly to longitudinal bending modes because their deflection character is also dominated by the elastic modulus of the specimen.

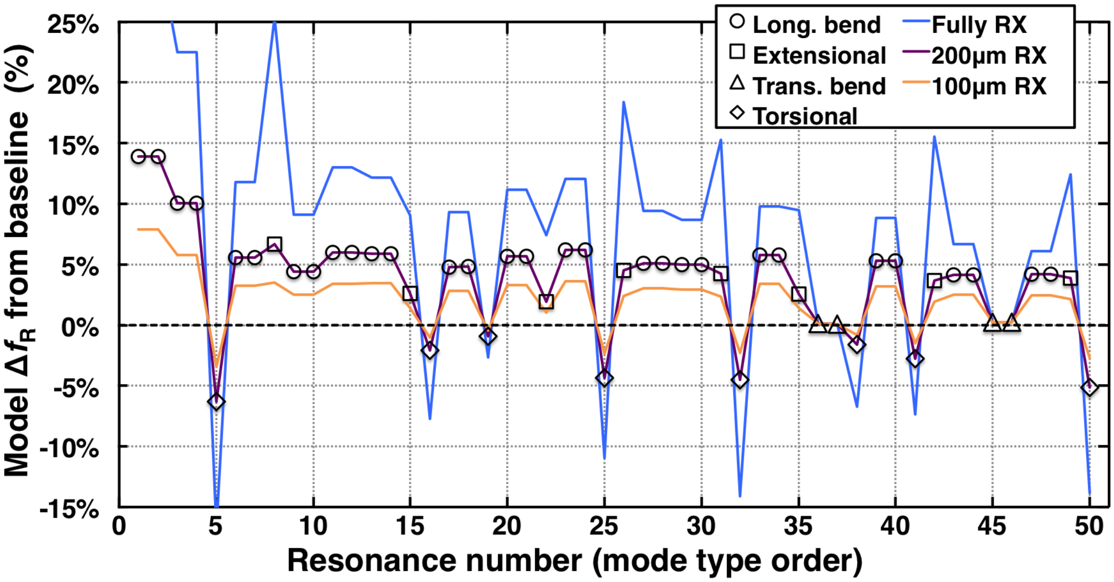

Figure 7.9: Model predicted mode-specific Δf_R for surface recrystallization of various depths along the gauge and fillet sections. The fully recrystallized model illustrates the most extreme case, and the 200 μm line has the resonance mode shape information overlaid. Because the modeled mode order is constant regardless of recrystallized depth, resonance mode shape is only included for the 200 μm line. Plot courtesy of Brent Goodlet.

The modeled transverse bending modes are not affected by the layer of recrystallized material due to fact that the deflection of these modes is concentrated at the ends of the specimen, effectively sampling the modulus of the virgin single-crystal material; see Figures 7.4 and 7.5. The resonance modes identified as torsional exhibited a negative Δf_R as a function of the recrystallized depth due to the fact that G_{GK} is less than $\mathrm{G}_{\{100\}[\perp]}$.

There is excellent agreement between the order-corrected measured Δf_R and the modeled Δf_R across the first 50 resonance modes, illustrated in Figure 7.10, with the Δf_R listed in Tables 7.6 and 7.7 for the reliably-measured resonance modes. Missing experimental data points indicate frequencies where the resonance modes could not be reliably recorded due to the low amplitude displacement character of the resonance mode in relation to transducer placement, or masking by a neighboring high-amplitude mode. Figure 7.11 indicates a linear relationship between Δf_R and recrystallization depth up to 200 μm for bending modes (resonance numbers 13,14, 27-30, 33, and 34). The linear relationship is a result of the linear dependence of the specimen modulus on volume fraction of recrystallized material (as one would expect from a rule of mixtures average), and the effectively linear relationship between volume fraction of recrystallized material and the recrystallization depth, assuming recrystallization consumes only a small fraction of the specimen radius. Models of a fully recrystallized specimen indicate that the Δf_R trend with recrystallization depth becomes logarithmic due to the specimen's circular cross section, where for each incremental increase in recrystallization depth the volume of newly recrystallized material logarithmically approaches zero.

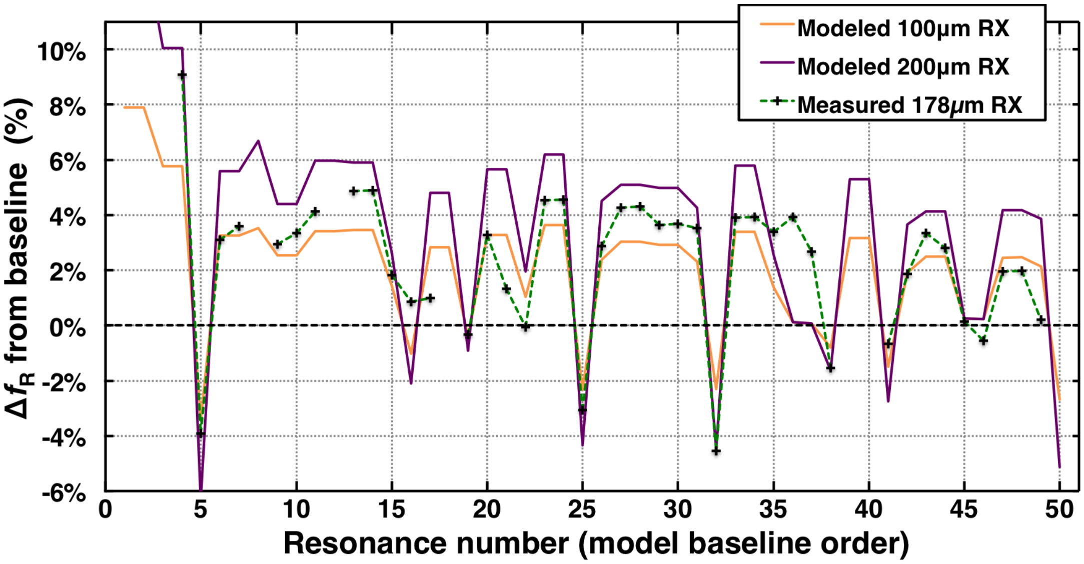

Figure 7.10: Order-corrected measurements of Δf_R from the high pressure shot peened sample plotted with FE modeled Δf_R for recrystallized layer depths of 100 and 200 μm. There is good agreement between measurements and models for a majority of modes. Breaks in the measured data indicate where resonance modes were not reliably recorded. Plot courtesy of Brent Goodlet.

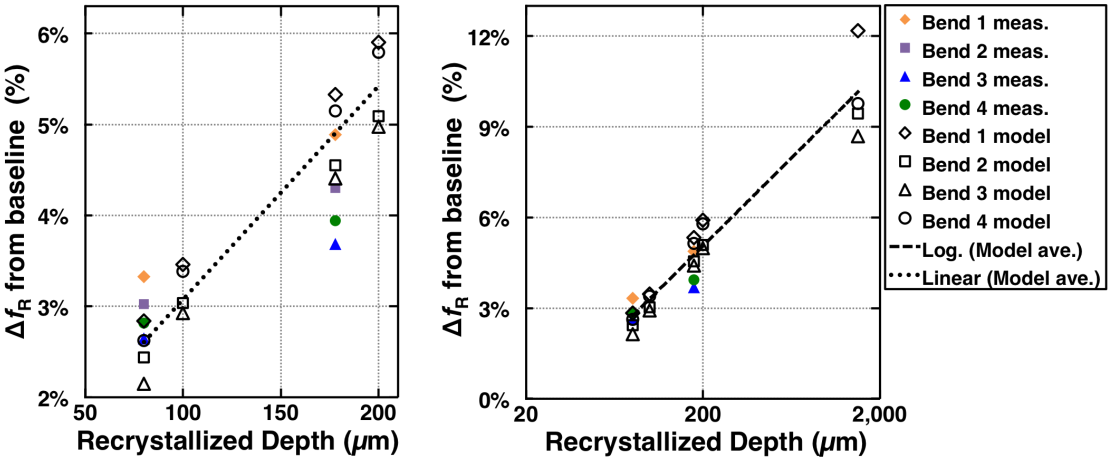

Figure 7.11: Plot of Δf_R versus recrystallized depth for select bending modes with both measured and modeled points indicated at 80 and 178 μm. When recrystallization consumes small fractions of the specimen radius, the Δf_R appears linear with recrystallization depth as the left plot indicates; however, the trend becomes logarithmic at large fractions of the specimen radius as the right plot demonstrates.

7.6 Advantages of RUS for Detecting Recrystallization

The RUS technique used in this work was able to detect the presence of recrystallized material in shot peened and subsequently heat treated laboratory scale specimens. The primary advantages of using RUS when compared to other NDE techniques are the ease of use, short scan times, objective definitions for part acceptance/rejection, full component sampling with a single measurement, and the ability to configure the piezoelectric transducers for NDE of various component geometries. While laboratory scans for developing this NDE framework were extremely conservative and required on the order of an hour to complete, optimized scan settings can reduce collection time to less than a minute per part without sacrificing diagnostic abilities.

Accurate prediction of the recrystallized depth from experimentally measured Δf_R without requiring destructive microscopic examination was demonstrated with a specimen-specific FE based f_R model. Beyond the use in this thesis to non-destructively detect recrystallization during multiple rejuvenation testing, this capability has the potential to detect various grain defects in as-cast components, helping to improve single crystal processing approaches and manufacturing yields. Also, because the RUS technique samples bulk properties, internal recrystallization can also be detected.

7.7 Conclusions

Based on the results of detailed RUS and FE modeling, the following conclusions are made with regards to the capability of detecting grain defects in elastically anisotropic Ni-base single crystals:

- RUS has been successfully implemented as part of a multiple rejuvenation test to detect the presence of recrystallization, a recovery mechanism that limits rejuvenation. The mechanistic underpinning of evaluating abnormalities in grain structure with RUS relies on significant elastic anisotropy, a requirement met by Ni-base alloys.
- A finite element model of a superalloy specimen with a thin layer of material with isotropic elastic properties showed good agreement with the experimentally measured frequency shifts after heat treatment of shot peened specimens, confirming that recrystallization caused the observed positive frequency shifts in both the shot peened and multiple rejuvenation creep specimens.
- Recrystallization can be detected nondestructively by using resonant ultrasound spectroscopy equipment similar to that utilized in this study. Shifts in resonance frequency have a linear relationship to the volume of recrystallized material for resonance frequencies with a bending mode type.
- Due to specimen elongation during creep testing, RUS was unable to detect the presence of cracks and cavities at the creep strain levels of interest for rejuvenation.

Chapter 8

Important Conclusions and Recommendations

In this work, the viability of rejuvenating Ni-based superalloys GTD444(CG) and René N5(SX) has been examined. A focus has been placed on providing a detailed analysis on the observed and potential phenomena preventing or limiting the success of a rejuvenation treatment. Rejuvenation consisted of a solution + aging heat treatment that was derived from typical post-casting heat treatments. Small-scale material removal was included to remove hold-time fatigue damage. The important conclusions from this thesis work are presented in this chapter, followed by a discussion of suggested future work and recommendations. The expected challenges of transitioning from lab-scale to industrial scale rejuvenation will also be examined.

1. As a result of multiple rejuvenation testing, the total creep rupture life of René N5(SX) tested at 982 °C and 206 MPa was extended by a factor of 2.8 over the baseline rupture life. To produce this increase in rupture life, creep strain thresholds of both 2% and 3% were used along with solutioning at 28 °C below the γ' solvus temperature for 2 h and aging at 1079 °C for 4 h. These rejuvenation conditions resulted in the maximum observed increase in total creep rupture life. In addition to the extension in creep life, the creep curve shape was recovered and the time to the creep strain threshold was maintained above 80% of the initial creep test.

    (a) Based on the multiple rejuvenation tests performed, an appropriate criterion for successful rejuvenation of creep properties was the recovery of 80% of the initial time to the creep strain threshold, with the baseline determined by the creep test during the first rejuvenation cycle. This criterion was applied to both GTD444(CG) and René N5(SX).

    (b) Successful rejuvenation required a creep strain threshold below 5%. The failure of a rejuvenation heat treatment to recover macroscopic plastic strain near 5% is most likely a combination of an increased dislocation density and enhanced plasticity near stress concentrators such as carbides and pores.

    (c) As expected, the solution temperature used during the rejuvenation heat treatment had an impact on the amount of recovery and recrystallization. Solutioning at the γ' solvus for René N5(SX) resulted in the greatest recovery of the initial creep performance but only increased the total creep rupture life by a factor of 1.8 due to the nucleation of recrystallized grains. A clear tradeoff exists between recovery and suppressing recrystallization that resulted in an optimal solution temperature of 28 °C below the γ' solvus temperature for René N5(SX) at a creep strain threshold of 2%.

2. Damage from sustained peak low-cycle fatigue (SPLCF) testing was also successfully rejuvenated by removing surface cracks via small scale material removal (polishing). A rejuvenation heat treatment was not required to extend the fatigue life, indicating that significant recovery of the dislocation substructure is not necessary. SPLCF life was extended by a factor of 2, and was limited by the 400-600 μm of material removed during each rejuvenation cycle.

    (a) While removing 400-600 μm of material was achievable on a lab scale, implementation in industry will be challenging. Additionally, the total number of rejuvenation cycles will be limited by the blade wall thickness instead of specimen thickness. A better approach would be to use a high strength coating to suppress oxidation-induced surface crack growth, preventing the surface crack growth from transitioning into the substrate before the first rejuvenation cycle. Recoating could then be used to remove the SPLCF cracks.

3. Transverse grain boundaries limited life during multiple rejuvenation creep testing of both GTD444(CG) and René N5(SX). Due to the tortuosity of the grain boundaries in GTD444(CG), some boundaries are initially oriented transverse to the growth di-

rection. The enhanced plasticity near these grain boundaries may be the primary reason why the initially single crystal René N5(SX) specimens were more amenable to rejuvenation than GTD444(CG). For both alloys, recrystallization during the rejuvenation heat treatment was responsible for early failure during the subsequent creep test.

(a) At creep conditions more comparable to service, failure in GTD444(CG) was still controlled by high angle grain boundaries but primarily by grain boundary oxidation rather than enhanced plasticity. Such oxidation-controlled failure cannot be repaired using hot isostatic pressing (HIP) or a rejuvenation heat treatment, further limiting the rejuvenation potential of GTD444(CG). Carbide decomposition and precipitation of the η phase in GTD444(CG) did not have a detectable influence on the creep performance, but are expected to serve as crack initiation sites during fatigue loading.

(b) The precipitation of topologically closed packed (TCP) phases was observed in a β-NiAl coated René N5(SX) specimen after a multiple rejuvenation test. TCP phases deplete the γ matrix of solid solution strengtheners and decrease creep resistance. However, the formation of TCP phases can be suppressed by changing the composition of the superalloy or coating and consequently, is not considered rejuvenation limiting.

(c) Rejuvenation of fatigue cracks initiating from internal porosity was not investigated in this work. Such damage is expected to limit rejuvenation when turbine life is controlled by low-cycle and high-cycle fatigue. HIP may be required to heal internal cracks and reduce the initial pore size but may also cause recrystallization. Additionally, the use of liquid metal cooling (LMC) has been shown in literature to reduce the maximum pore size by 70%, increasing the fatigue life.

4. Resonant ultrasound spectroscopy (RUS), a non-destructive evaluation technique, was successfully used to detect the presence of recrystallization during multiple rejuvenation testing.
   (a) A finite element model of a superalloy specimen with a thin layer of material with isotropic elastic properties (approximating a layer of recrystallized grains) showed good agreement with the experimentally measured frequency shifts after heat treatment of shot peened creep specimens, confirming that recrystallization caused the frequency shifts. Shifts in resonance frequency of bending modes have a linear relationship to the volume of recrystallized material.
   (b) The detection of abnormalities in grain structure with RUS relies on significant elastic anisotropy, a requirement met by Ni-base alloys. Thus RUS can be used more generally to detect to the prevalence of defects induced during single crystal growth or subsequent processing. Common defects involve the presence of misoriented (non-single crystal) material that change the bulk elastic properties.
   (c) The RUS technique did not detect the onset of recrystallization but detected

recyrstallization once a critical volume fraction of recrystallized material had been reached, assuming a random orientation of recrystallized nuclei. The presence of detectable levels of recrystallization always resulted in abrupt specimen rupture during multiple rejuvenation creep testing.

(d) Due to specimen elongation during creep testing, RUS was unable to detect the presence of cracks and cavities at the creep strain levels of interest for rejuvenation.

Substantial opportunities exist for further investigation of the rejuvenation of Ni-base superalloys. Creep tests performed in this work were limited to the high temperature low stress regime where initial dislocation activity is confined to the matrix γ phase. Creep testing at a low temperature and high stress condition would determine if rejuvenation could recover significant primary creep strains caused by shearing of the γ' phase by $a\langle 112\rangle$ ribbons. Testing at multiple creep testing conditions would also further illustrate the applicability of rejuvenating full turbine blades, where the stress and temperature experienced during service is location dependent.

Multiple rejuvenation tests performed with creep strain thresholds of 1% and 4% are suggested to further develop the René N5(SX) rejuvenation map. Additionally, recoating René N5(SX) specimens between rejuvenation cycles rather then exposing the coating to the rejuvenation heat treatment may further increase the extension in total creep rupture life by delaying the precipitation of TCPs.

8.1 Guidelines for Achieving Successful Rejuvenation

To be successful, a rejuvenation procedure must be designed to repair damage caused by the life limiting mechanism. Rejuvenation must also be performed prior to the onset of irreparable damage but late enough to be cost-effective. When creep limits life, a solution + aging rejuvenation heat treatment was successful in recovering damage in single crystal René N5(SX) at low creep strains, where irreparable damage, such as creep cavities, is not present. In GTD444(CG) specimens, enhanced plasticity near transverse grain boundaries prevented rejuvenation to a satisfactory level of creep performance at the creep strain thresholds and heat treatment conditions examined. When component life is limited by fatigue, HIP may be required to repair internal cracks. Surface cracks can be destructively removed but such procedures may be difficult and costly to implement on engine components.

The development of new alloy compositions, the use of advanced processing techniques, and the application of coatings to maximize resistance against irreparable forms of damage appears to be a viable approach to enable successful rejuvenation. Additionally, rejuvenation should be used in conjunction with a part tracking system, which would identify specific turbine blades that are expected to have above average baseline mechanical properties. If using a “starts and hours” based inspection criterion, these components should have less damage and consequently be good candidates for rejuvenation. Part tracking should continue through each maintenance and rejuvenation cycle, relying on a non-destructive evaluation system such as RUS to detect irreparable damage caused by service or the rejuvenation treatment.

While a number of questions regarding the rejuvenation of advanced directionally solidified alloys have been addressed in this work, using rejuvenation in a production environment on these alloys represents a significant challenge. There will be a difference in microstructure between lab and industrial-scale components and a difference between service and mechanical testing conditions, requiring detailed characterization and identification of the life-limiting form of damage. Ultimately, the use of rejuvenation will depend on a number of factors that must be considered for each specific case. These include but are not limited to: the life-limiting form of damage, initial component production cost and life, the cost of rejuvenation and expected life extension, and the presence of irreparable damage.

Bibliography

[1] R. E. Sonntag, C. Borgnakke, Introduction to engineering thermodynamics, Wiley New York, 2001.

[2] R. C. Reed, The superalloys: fundamentals and applications, Cambridge University Press, 2006.

[3] N. A. Cumpsty, Jet Propulsion: A simple guide to the aerodynamic and thermodynamic design and performance of jet engines, volume 2, Cambridge University Press, 2003.

[4] S. Balsone, Buckets, and nozzles, The Gas Turbine Handbook, Section 4 (2004).

[5] P. C. Evans, M. Annunziata, Industrial internet: Pushing the boundaries of minds and machines, General Electric (2012) 21.

[6] W. Donachie, S. J. Donachie, Superalloys Technical Guide 2nd Edition, ASM International, 2002.

[7] A. Elliott, T. Pollock, S. Tin, W. King, S.-C. Huang, M. Gigliotti, Directional solidification of large superalloy castings with radiation and liquid-metal cooling: a comparative assessment, Metall. Mater. Trans. A 35 (2004) 3221–3231.

[8] Rolls-Royce plc, The Jet Engine, 4th edn, Technical Report, Derby, UK: The Technical Publications Department, Rolls-Royce plc, 1992.

[9] B. Kear, B. Piearcey, Tensile and creep properties of single crystals of the nickel-base superalloy Mar-M 200 (Nickel-base single crystal superalloy tensile and creep properties, comparing single and multiple slip orientations), AIME, Transactions 239 (1967) 1209–1215.

[10] T. M. Pollock, S. Tin, Nickel-based superalloys for advanced turbine engines: chemistry, microstructure and properties, J. Propul. Power 22 (2006) 361–374.

[11] U. R. Kattner, The thermodynamic modeling of multicomponent phase equilibria, JOM 49 (1997) 14–19.

[12] H. Okamoto, Al-Ni (Aluminum-Nickel)ckel), J. Phase Equilib. 14 (1993) 257–259.

[13] S. Tin, T. Pollock, W. King, Carbon additions and grain defect formation in high refractory nickel-base single crystal superalloys, in: Proc. 9th Symposium on Superalloys, volume 1001, Superalloys 2000, p. 48109.

[14] T. Grosdidier, A. Hazotte, A. Simon, Precipitation and dissolution processes in γ/γ' single crystal nickel-based superalloys, Mater. Sci. Eng. A 256 (1998) 183–196.

[15] G. K. Bouse, M. F. Henry, J. C. Schaeffer, et al., Nickel base superalloys and turbine components fabricated therefrom, 2005. US Patent 6,908,518.

[16] E. W. Ross, C. S. Wukusick, W. T. King, Nickel-based superalloys for producing single crystal articles having improved tolerance to low angle grain boundaries, 1995. US Patent 5,399,313.

[17] C. S. Wukusick, L. Buchakjian Jr, Nickel-base superalloys, 1991. Patent Number GB 2235697.

[18] K. Kawagishi, A.-C. Yeh, T. Yokokawa, T. Kobayashi, Y. Koizumi, H. Harada, Development of an oxidation-resistant high-strength sixth-generation single-crystal superalloy TMS-238, in: Proc. 12th Symposium on Superalloys, Superalloys 2012, pp. 9–13.

[19] T. Pollock, W. Murphy, The breakdown of single-crystal solidification in high refractory nickel-base alloys, Metall. Mater. Trans. A 27 (1996) 1081–1094.

[20] D. A. Porter, K. E. Easterling, Phase Transformations in Metals and Alloys, 2nd ed., Chapman & Hall, 1992.

[21] M. Fahrmann, W. Hermann, E. Fahrmann, A. Boegli, T. Pollock, H. Sockel, Determination of matrix and precipitate elastic constants in (γ–γ') Ni-base model alloys, and their relevance to rafting, Mater. Sci. Eng. A 260 (1999) 212–221.

[22] H. Mughrabi, Microstructural aspects of high temperature deformation of monocrystalline nickel base superalloys: some open problems, Mater. Sci. Technol. 25 (2009) 191–204.

[23] B. Dyson, M. McLean, Particle-coarsening, σ_0 and tertiary creep, Acta Metall. 31 (1983) 17–27.

[24] T. Pollock, A. Argon, Creep resistance of CMSX-3 nickel base superalloy single crystals, Acta Metall. Mater. 40 (1992) 1–30.

[25] G. R. Leverant, B. H. Kear, The mechanism of creep in gamma prime precipitation-hardened nickel-base alloys at intermediate temperatures, Metall. Mater. Trans. B 1 (1970) 491–498.

[26] P. Caron, T. Khan, Improvement of creep strength in a nickel-base single-crystal superalloy by heat treatment, Mater. Sci. Eng. 61 (1983) 173–184.

[27] T. Pollock, R. Field, Dislocations and high-temperature plastic deformation of superalloy single crystals, Dislocat. Solids 11 (2002) 547–618.

[28] H. Mughrabi, H. Feng, H. Biermann, On the micromechanics of the deformation of monocrystalline nickel-base superalloys, in: IUTAM Symposium on Micromechanics of Plasticity and Damage of Multiphase Materials, Springer, 1996, pp. 115–122.

[29] T. Pollock, A. Argon, Directional coarsening in nickel-base single crystals with high volume fractions of coherent precipitates, Acta Metall. Mater. 42 (1994) 1859–1874.

[30] F. R. Nabarro, Rafting in superalloys, Metall. Mater. Trans. A 27 (1996) 513–530.

[31] M. Fahrmann, E. Fahrmann, O. Paris, P. Fratzl, T. Pollock, An experimental study of the role of plasticity in the rafting kinetics of a single crystal Ni-base superalloy, in: Proc. 8th Symposium on Superalloys, TMS, Warrendale, PA, USA, Superalloys 1996, pp. 191–200.

[32] M. Kamaraj, Rafting in single crystal nickel-base superalloys - an overview, Sadhana 28 (2003) 115–128.

[33] M. Rist, R. Reed, Inverse method for parameter optimisation in superalloy tertiary creep equations, Mater. Sci. Technol. 18 (2002) 179–186.

[34] B. Dyson, T. Gibbons, Tertiary creep in nickel-base superalloys: analysis of experimental data and theoretical synthesis, Acta Metall. 35 (1987) 2355–2369.

[35] A. Argon, W. Moffatt, Climb of extended edge dislocations, Acta Metall. 29 (1981) 293–299.

[36] R. Srinivasan, G. Eggeler, M. Mills, γ'-cutting as rate-controlling recovery process during high-temperature and low-stress creep of superalloy single crystals, Acta Mater. 48 (2000) 4867–4878.

[37] T. M. Pollock, A. S. Argon, Directional Coarsening in Nickel-Base Single Crystals with High Volume Fractions of Coherent Precipitates, Acta Metall. Mater. 42 (1994) 1859–1874.

[38] S. Ai, V. Lupinc, M. Maldini, Creep fracture mechanisms in single crystal superalloys, Scr. Metall. Mater. (1992) 579–584.

[39] M. Loveday, B. Dyson, Prestrain-induced particle microcracking and creep cavitation in IN597, Acta Metall. 31 (1983) 397–405.

[40] H. Tipler, Y. Lindblom, J. Davidson, Damage accumulation and fracture in creep of Ni-base alloys, in: High Temperature Alloys for Gas Turbines, Liege, Belgium, Sept. 1978, 1978, pp. 359–407.

[41] A. Cocks, M. Ashby, On creep fracture by void growth, Prog. Mater. Sci. 27 (1982) 189–244.

[42] M. Ashby, C. Gandhi, D. Taplin, Overview No. 3 fracture-mechanism maps and their construction for fcc metals and alloys, Acta Metall. 27 (1979) 699–729.

[43] A. I. H. Committee, ASM handbook: Materials selection and design, volume 20, CRC Press, 1997.

[44] T. Gabb, G. Welsch, The high temperature deformation in cyclic loading of a single crystal nickel-base superalloy, Acta Metall. 37 (1989) 2507–2516.

[45] R. Dalal, C. Thomas, L. Dardi, The effect of crystallographic orientation on the physical and mechanical properties of an investment cast single crystal nickel-base superalloy, in: Proc. Fifth Symposium on Superalloys, volume 84, ASM, Materials Park, OH, Superalloys 1984, pp. 185–197.

[46] P. Lukáš, L. Kunz, Cyclic slip localisation and fatigue crack initiation in fcc single crystals, Mater. Sci. Eng. A 314 (2001) 75–80.

[47] P. Lukáš, L. Kunz, Role of persistent slip bands in fatigue, Philos. Mag. 84 (2004) 317–330.

[48] V. Brien, B. Décamps, Low cycle fatigue of a nickel based superalloy at high temperature: deformation microstructures, Mater. Sci. Eng. A 316 (2001) 18–31.

[49] P. Wright, M. Jain, D. Cameron, High cycle fatigue in a single crystal superalloy: time dependence at elevated temperature, in: Proc. 10th Symposium on Superalloys, ASM, Materials Park, OH, Superalloys 2004, pp. 657–666.

[50] A. Suzuki, M. Gigliotti, B. Hazel, D. Konitzer, T. Pollock, Crack progression during sustained-peak low-cycle fatigue in single-crystal Ni-base superalloy René N5, Metall. Mater. Trans. A 41 (2010) 947–956.

[51] A. Evans, M. He, A. Suzuki, M. Gigliotti, B. Hazel, T. Pollock, A mechanism governing oxidation-assisted low-cycle fatigue of superalloys, Acta Mater. 57 (2009) 2969–2983.

[52] V. K. Tolpygo, D. Clarke, On the rumpling mechanism in nickel-aluminide coatings: Part I: an experimental assessment, Acta Mater. 52 (2004) 5115–5127.

[53] J. Nychka, D. Clarke, Quantification of aluminum outward diffusion during oxidation of FeCrAl alloys, Oxid. Met. 63 (2005) 325–352.

[54] T. M. Pollock, B. Laux, C. L. Brundidge, A. Suzuki, M. Y. He, Oxide-assisted degradation of ni-base single crystals during cyclic loading: the role of coatings, J. Am. Ceram. Soc. 94 (2011) 136–145.

[55] N. Isobe, S. Sakurai, Compressive strain hold effect on high temperature low-cycle fatigue crack growth in superalloys, Mater. Sci. Res. Int. 9 (2003) 29–33.

[56] T. Totemeier, J. King, Isothermal fatigue of an aluminide-coated single-crystal superalloy: Part I, Metall. Mater. Trans. A 27 (1996) 353–361.

[57] T. Totemeier, W. Gale, J. King, Isothermal fatigue of an aluminide-coated single-crystal superalloy: Part II. effects of brittle precracking, Metall. Mater. Trans. A 27 (1996) 363–369.

[58] R. Kowalewski, H. Mughrabi, Influence of a plasma-sprayed NiCrAlY coating on the low-cycle fatigue behaviour of a directionally solidified nickel-base superalloy, Mat. Sci. Eng. A 247 (1998) 295–299.

[59] L. H. Rettberg, B. Laux, M. Y. He, D. Hovis, A. H. Heuer, T. M. Pollock, Growth stresses in thermally grown oxides on nickel-based single-crystal alloys, Metall. Mater. Trans. A (2016) 1–11.

[60] R. Hoeft, E. Gebhardt, Heavy-duty gas turbine operating and maintance considerations, Technical Report, GE Energy Services, 2000.

[61] A. Baldan, Rejuvenation procedures to recover creep properties of nickel-base superalloys by heat treatment and hot isostatic pressing techniques, J. Mater. Sci. 26 (1991) 3409–3421.

[62] A. Rollett, F. Humphreys, G. S. Rohrer, M. Hatherly, Recrystallization and related annealing phenomena, Elsevier, 2004.

[63] F. Prinz, A. Argon, W. Moffatt, Recovery of dislocation structures in plastically deformed copper and nickel single crystals, Acta Metall. 30 (1982) 821–830.

[64] D. McLean, The physics of high temperature creep in metals, Reports on Progress in Physics 29 (1966) 1.

[65] R. Doherty, D. Hughes, F. Humphreys, J. Jonas, D. J. Jensen, M. Kassner, W. King, T. McNelley, H. McQueen, A. Rollett, Current issues in recrystallization: a review, Mater. Sci. Eng. A 238 (1997) 219–274.

[66] R. Cahn, Recrystallization of single crystals after plastic bending, J. Inst. Met. 76 (1949) 121.

[67] R. Doherty, The deformed state and nucleation of recrystallization, Met. Sci. 8 (1974) 132–142.

[68] R. Doherty, Recrystallization of metallic materials, Ed. By Frank Haessner. Dr. Riederer Verlag GmbH, Stuttgart (1978).

[69] P. Davies, J. Dennison, H. Evans, Recovery of properties of a nickel-base high-temperature alloy after creep at 750 °C, J. Inst. Metals 94 (1966) 270–275.

[70] P. Davies, J. Dennison, H. Evans, The kinetics of the recovery of creep properties during annealing of Nimonic 80A after creep at 750 °C, J. Inst. Metals 95 (1967) 231–234.

[71] P. Davies, J. Dennison, D. Sidey, Recovery of mechanical properties of Nimonic 105 by heat-treatment after high-temperature creep, J. Inst. Metals 101 (1973) 153–161.

[72] P. Davies, J. Dennison, The use of heat-treatment to recover the creep properties of Nimonic 115 after high-temperature creep, Met. Sci. 9 (1975) 319–323.

[73] R. Hart, H. Gayter, Recovery of mechanical properties in nickel alloys by reheat-treatment, J. Inst. Metals 96 (1968) 338–344.

[74] J. Dennison, P. Holmes, B. Wilshire, The creep and fracture behaviour of the cast, nickel-based superalloy, IN100, Mater. Sci. Eng. 33 (1978) 35–47.

[75] B. Wilshire, J. Dennison, I. Elliott, An assessment of hot isostatic pressing and reheat treatment for the regeneration of creep properties of superalloys, in: Proc. Fourth Symposium on Superalloys, ASM, Materials Park, OH, Superalloys 1980.

[76] R. Stevens, P. Flewitt, Intermediate regenerative heat treatments for extending the creep life of the superalloy IN-738, Mater. Sci. Eng. 50 (1981) 271–284.

[77] M. Mclean, H. Tipler, Assessment of damage accumulation and property regeneration by hot isostatic pressing and heat treatment of laboratory-tested and service exposed IN 738LC, in: Proc. Fifth Symposium on Superalloys, ASM, Materials Park, OH, Superalloys 1984, pp. 73–82.

[78] M. D. Ross, G. T. Bennett, D. C. Stewart, Rejuvenation of Turbine Blade Material by Thermal Treatment., Technical Report, DTIC Document, 1979.

[79] J. Wortmann, Improving reliability and lifetime of rejuvenated turbine blades, Mater. Sci. Technol. 1 (1985) 644–650.

[80] T. Maccagno, A. Koul, J.-P. Immarigeon, L. Cutler, R. Allem, G. L'espérance, Microstructure, creep properties, and rejuvenation of service-exposed alloy 713C turbine blades, Metall. Trans. A 21 (1990) 3115–3125.

[81] E. Lvova, A comparison of aging kinetics of new and rejuvenated conventionally cast GTD-111 gas turbine blades, J. Mater. Eng. Perform. 16 (2007) 254–264.

[82] W. McCall, Turbine blade life can be extended by reconditioning, Combustion 42 (1971) 27.

[83] M. Lamberigts, C. Lecomte-Mertens, P. Vierset, Structural damage and rejuvenation of used turbine blades, in: Application of Advanced Material for Turbomachinery and Rocket Propulsion, 1986.

[84] S. I. Wright, M. M. Nowell, D. P. Field, A review of strain analysis using electron backscatter diffraction, Microsc. Microanal. 17 (2011) 316–329.

[85] T. Maitland, S. Sitzman, Electron backscatter diffraction (EBSD) technique and materials characterization examples, Springer Berlin, 2007.

[86] S. I. Wright, A review of automated orientation imaging microscopy (OIM), J. Comput. Assist. Microsc. 5 (1993) 207–221.

[87] B. L. Adams, S. I. Wright, K. Kunze, Orientation imaging: the emergence of a new microscopy, Metall. Trans. A 24 (1993) 819–831.

[88] J. C. Aldrin, L. Jauriqui, L. Hunter, Models for process compensated resonant testing (PCRT) of silicon nitride balls, in: 39th Annu. Rev. Prog. Quant. Nondestruct. Eval., 2013, pp. 1393–1400.

[89] L. H. Rettberg, M. Tsunekane, T. M. Pollock, Rejuvenation of nickel-based superalloys GTD444 (DS) and René N5 (SX), in: Proc. 12th Symposium on Superalloys, ASM, Materials Park, OH, Superalloys 2012, pp. 341–349.

[90] L. Rettberg, T. Pollock, Localized recrystallization during creep in nickel-based superalloys GTD444 and René N5, Acta Mater. 73 (2014) 287–297.

[91] D. Pearson, F. Lemkey, B. Kear, Stress coarsening of γ' and its influence on creep properties of a single crystal superalloy, in: Proc. Fourth Symposium on Superalloys, ASM, Metals Park, OH, Superalloys 1980, p. 513.

[92] M. Nathal, R. MacKay, R. Miner, Influence of precipitate morphology on intermediate temperature creep properties of a nickel-base superalloy single crystal, Metall. Trans. A 20 (1989) 133–141.

[93] R. A. MacKay, L. J. Ebert, The development of γ-γ' lamellar structures in a nickel-base superalloy during elevated temperature mechanical testing, Metall. Trans. A 16 (1985) 1969–1982.

[94] W. D. Pridemore, Stress-rupture characterization in nickel-based superalloy gas turbine engine components, J. Fail. Anal. and Preven. 8 (2008) 281–288.

[95] L. Liu, T. Jin, N. Zhao, X. Sun, H. Guan, Z. Hu, Formation of carbides and their effects on stress rupture of a ni-base single crystal superalloy, Mater. Sci. Eng. A 361 (2003) 191–197.

[96] R. Reed, D. Cox, C. Rae, Damage accumulation during creep deformation of a single crystal superalloy at 1150 °C, Mater. Sci. Eng. A 448 (2007) 88–96.

[97] Y. Kong, Q. Chen, D. Knowles, Effects of minor additions on microstructure and creep performance of RR2086 SX superalloys, J. Mater. Sci. 39 (2004) 6993–7001.

[98] R. Doherty, Role of interfaces in kinetics of internal shape changes, Met. Sci. 16 (1982) 1–14.

[99] A. Suzuki, M. Gigliotti, B. T. Hazel, D. G. Konitzer, T. M. Pollock, Crack progression during sustained-peak low-cycle fatigue in single-crystal ni-base superalloy René N5, Metall. Mater. Trans. A 41 (2010) 947–956.

[100] A. Porter, B. Ralph, Recrystallization of a nickel-base superalloy: kinetics and microstructural development, Mater. Sci. Eng. 59 (1983) 69–78.

[101] S. Chen, G. Gottstein, Strain softening, grain boundary migration and dynamic recrystallization of Ni during high temperature low cycle fatigue, Acta Metall. 36 (1988) 3093–3101.

[102] R. Doherty, D. Hughes, F. Humphreys, J. Jonas, D. J. Jensen, M. Kassner, W. King, T. McNelley, H. McQueen, A. Rollett, Current issues in recrystallization: a review, Mater. Sci. Eng. A 238 (1997) 219–274.

[103] F. Humphreys, Recrystallization mechanisms in two-phase alloys, Met. Sci. 13 (1979) 136–145.

[104] M. Ashby, The deformation of plastically non-homogeneous materials, Philos. Mag. 21 (1970) 399–424.

[105] C. J. Humphreys, M. Hatherly, Recrystallization and Related Annealing Phenomena, Elsevier, 2004.

[106] W. Read, W. Shockley, Dislocation models of crystal grain boundaries, Phys. Rev. 78 (1950) 275.

[107] M. D. Sangid, H. Sehitoglu, H. J. Maier, T. Niendorf, Grain boundary characterization and energetics of superalloys, Mater. Sci. Eng. A 527 (2010) 7115–7125.

[108] R. Srinivasan, G. Eggeler, M. J. Mills, γ'-cutting as rate-controlling recovery process during high-temperature and low-stress creep of superalloy single crystals, Acta Mater. 48 (2000) 4867–4878.

[109] J. O. Andersson, T. Helander, L. Höglund, P. F. Shi, B. Sundman, Thermo-Calc and DICTRA, Computational tools for materials science. Calphad 26 (2002) 273–312.

[110] J. Bee, A. Jones, P. Howell, The interaction of recrystallizing interfaces with intragranular precipitate dispersions in a nickel-base superalloy, J. Mater. Sci. 16 (1981) 1471–1476.

[111] K. Smidoda, C. Gottschalk, H. Gleiter, Grain boundary diffusion in migrating boundaries, Met. Sci. 13 (1979) 3–4.

[112] J. Nystrom, T. Pollock, W. Murphy, A. Garg, Discontinuous cellular precipitation in a high-refractory nickel-base superalloy, Metall. Mater. Trans. A 28 (1997) 2443–2452.

[113] H. Hirst, The recrystallization of dilute lead alloys after severe deformation, J. Inst. Metals 66 (1940) 39.

[114] R. Gifkins, The effect of stress on the recrystallization of lead during creep, J. Inst. Metals 86 (1957) 15–16.

[115] P. Karduck, G. Gottstein, H. Mecking, Deformation structure and nucleation of dynamic recrystallization in copper single crystals, Acta Metall. 31 (1983) 1525–1536.

[116] G. Gottstein, U. Kocks, Dynamic recrystallization and dynamic recovery in <111> single crystals of nickel and copper, Acta Metall. 31 (1983) 175–188.

[117] R. Bürgel, P. D. Portella, J. Preuhs, Recrystallization in single crystals of nickel base superalloys, Superalloys 2000 (2000) 229–238.

[118] D. Cox, B. Roebuck, C. Rae, R. Reed, Recrystallisation of single crystal superalloy CMSX-4, Mater. Sci. Technol. 19 (2003) 440–446.

[119] L. Wang, G. Xie, J. Zhange, L. H. Lou, On the role of carbides during the recrystallization of a directionally solidified nickel-base superalloy, Acta Mater. 55 (2006) 457–460.

[120] C. Zambaldi, F. Roters, D. Raabe, U. Glatzel, Modeling and experiments on the indentation deformation and recrystallization of a single-crystal nickel-base superalloys, Mater. Sci. Eng. A (2007) 433–440.

[121] A. Porter, B. Ralph, The recrystallization of nickel-base superalloys, J. Mater. Sci. 16 (1981) 707–713.

[122] S. Bond, J. Martin, Surface recrystallization in a single crystal nickel-based superalloy, J. Mater. Sci. 19 (1984) 3867–3872.

[123] J. J. Moverare, S. Johansson, R. C. Reed, Deformation and damage mechanisms during thermal–mechanical fatigue of a single-crystal superalloy, Acta Mater. 57 (2009) 2266–2276.

[124] Y. Li, C. Tao, W. Zhang, Dynamic recrystallization behavior of a directionally solidified superalloy, Adv. Eng. Mater. 9 (2007) 867–871.

[125] C.-Y. Jo, H.-M. Kim, Effect of recrystallisation on microstructural evolution and mechanical properties of single crystal nickel based superalloy CMSX-2 Part 2-Creep behaviour of surface recrystallised single crystal, Mater. Sci. Technol. 19 (2003) 1671–1676.

[126] A. Cocks, M. Ashby, Intergranular fracture during power-law creep under multiaxial stresses, Met. Sci. 14 (1980) 8–9.

[127] A. Cocks, M. Ashby, On creep fracture by void growth, Prog. Mater. Sci. 27 (1982) 189–244.

[128] H. J. Frost, M. F. Ashby, Deformation Mechanism Maps: The Plasticity and Creep of Metals and Ceramics, Pergamon press, 1982.

[129] M. Ott, H. Mughrabi, Dependence of the high-temperature low-cycle fatigue behaviour of the monocrystalline nickel-base superalloys CMSX-4 and CMSX-6 on the γ/γ'-morphology, Mater. Sci. Eng. A 272 (1999) 24–30.

[130] F. R. N. Nabarro, F. De Villiers, Physics of creep and creep-resistant alloys, CRC press, 1995.

[131] R. Bürgel, P. Portella, J. Preuhs, Recrystallization in single crystals of nickel base superalloys, in: Proc. 12th Symposium on Superalloys, ASM, Materials Park, OH, Superalloys 2000, pp. 341–349.

[132] P. Callahan, J. Simmons, M. De Graef, A quantitative description of the morphological aspects of materials structures suitable for quantitative comparisons of 3d microstructures, Modell. Simul. in Mater. Sci. Eng. 21 (2012) 015003.

[133] J. MacSleyne, J. Simmons, M. De Graef, On the use of moment invariants for the automated analysis of 3d particle shapes, Modell. Simul. in Mater. Sci. Eng. 16 (2008) 045008.

[134] J. MacSleyne, J. Simmons, M. De Graef, On the use of 2-d moment invariants for the automated classification of particle shapes, Acta Mater. 56 (2008) 427–437.

[135] J. Maynard, Resonant ultrasound spectroscopy, Phys. Today 49 (1996) 26–31.

[136] C. Rae, R. Reed, Primary creep in single crystal superalloys: origins, mechanisms and effects, Acta Mater. 55 (2007) 1067–1081.

[137] R. A. MacKay, R. D. Maier, The influence of orientation on the stress rupture properties of nickel-base superalloy single crystals, Metall. Trans. A 13 (1982) 1747–1754.

[138] M. Nathal, Effect of initial gamma prime size on the elevated temperature creep properties of single crystal nickel base superalloys, Metall. Trans. A 18 (1987) 1961–1970.

[139] D. B. Miracle, R. Darolia, NiAl and its alloys, Intermetallic Compounds: Principles and Practice 2 (2000) 53–72.

[140] M. Pomeroy, Coatings for gas turbine materials and long term stability issues, Mater. Des. 26 (2005) 223–231.

[141] M. Zagula-Yavorska, M. Wierzbińska, K. Gancarczyk, J. Sieniawski, Degradation of nonmodified and rhodium modified aluminide coating deposited on CMSX 4 superalloy, J. Microsc. (2016).

[142] J. Nystrom, T. Pollock, W. Murphy, A. Garg, Discontinuous cellular precipitation in a high-refractory nickel-base superalloy, Metall. Mater. Trans. A 28 (1997) 2443–2452.

[143] R. Miner, T. Gabb, J. Gayda, K. Hemker, Orientation and temperature dependence of some mechanical properties of the single-crystal nickel-base superalloy René N4: Part III. tension-compression anisotropy, Metall. Trans. A 17 (1986) 507–512.

[144] D. Pope, S. S. Ezz, Mechanical properties of Ni_3AI and nickel-base alloys with high volume fraction of γ', Int. Met. Rev. 29 (1984) 136–167.

[145] N. Matan, D. Cox, P. Carter, M. Rist, C. Rae, R. Reed, Creep of CMSX-4 superalloy single crystals: effects of misorientation and temperature, Acta Mater. 47 (1999) 1549–1563.

[146] V. Sass, M. Feller-Kniepmeier, Orientation dependence of dislocation structures and deformation mechanisms in creep deformed CMSX-4 single crystals, Mater. Sci. Eng. A 245 (1998) 19–28.

[147] A. Giamei, Deformation and Fracture of Advanced Anisotropic Superalloys, Air Force Office of Scientific Research, Technical Report, AFOSR-TR-80-0033, 1979.

[148] G. Xie, L. Wang, J. Zhang, L. Lou, Influence of recrystallization on the high-temperature properties of a directionally solidified Ni-base superalloy, Metall. Mater. Trans. A 39 (2008) 206–210.

[149] J. Meng, T. Jin, X. Sun, Z. Hu, Effect of surface recrystallization on the creep rupture properties of a nickel-base single crystal superalloy, Mat. Sci. Eng. A 527 (2010) 6119–6122.

[150] B. Zhang, X. Lu, D. Liu, C. Tao, Influence of recrystallization on high-temperature stress rupture property and fracture behavior of single crystal superalloy, Mat. Sci. Eng. A 551 (2012) 149–153.

[151] T. Khan, P. Caron, Y. Nakagawa, Mechanical behavior and processing of DS and single crystal superalloys, JOM 38 (1986) 16–19.

[152] J. Stinville, K. Gallup, T. Pollock, Transverse creep of nickel-base superalloy bicrystals, Metall. Mater. Trans. A 46 (2015) 2516–2529.

[153] K. Harris, G. Erickson, S. Sikkenga, W. Brentnall, J. Aurrecoechea, K. Kubarych, Development of the rhenium containing superalloys CMSX-4® and CM 186LC® for single crystal blade and directionally solidified vane applications in advanced turbine engines, in: Proc. 7th Symposium on Superalloys, volume 297, TMS Warrendale, PA, USA, Superalloys 1992.

[154] K. Kubo, R. D. Pehlke, Mathematical modeling of porosity formation in solidification, Metall. Trans. B 16 (1985) 359–366.

[155] D. Poirier, K. Yeum, A. Maples, A thermodynamic prediction for microporosity formation in aluminum-rich Al-Cu alloys, Metall. Trans. A 18 (1987) 1979–1987.

[156] G. K. Sigworth, C. Wang, Mechanisms of porosity formation during solidification: a theoretical analysis, Metall. Trans. B 24 (1993) 349–364.

[157] L. G. Fritzemeier, Hot isostatic pressing of single crystal superalloy articles, 1996. US Patent 5,573,609.

[158] C. Brundidge, D. Van Drasek, B. Wang, T. Pollock, Structure refinement by a liquid metal cooling solidification process for single-crystal nickel-base superalloys, Metall. Mater. Trans. A 43 (2012) 965–976.

[159] C. L. Brundidge, T. M. Pollock, Processing to fatigue properties: benefits of high gradient casting for single crystal airfoils, in: Proc. 12th Symposium on Superalloys, TMS, Warrendale, PA, USA, Superalloys 2012, pp. 379–385.

[160] S. Steuer, P. Villechaise, T. Pollock, J. Cormier, Benefits of high gradient solidification for creep and low cycle fatigue of AM1 single crystal superalloy, Mater. Sci. Eng. A 645 (2015) 109–115.

[161] S. Tin, T. Pollock, W. Murphy, Stabilization of thermosolutal convective instabilities in Ni-based single-crystal superalloys: Carbon additions and freckle formation, Metall. Mater. Trans. A 32 (2001) 1743–1753.

[162] S. Tin, T. Pollock, Stabilization of thermosolutal convective instabilities in Ni-based single-crystal superalloys: Carbide precipitation and rayleigh numbers, Metall. Mater. Trans. A 34 (2003) 1953–1967.

[163] P. S. Karamched, A. J. Wilkinson, High resolution electron back-scatter diffraction analysis of thermally and mechanically induced strains near carbide inclusions in a superalloy, Acta Mater. 59 (2011) 263–272.

[164] H. Collins, Relative stability of carbide and intermetallic phases in nickel-base superalloys (1968).

[165] Q. Chen, N. Jones, D. Knowles, The microstructures of base/modified RR2072 SX superalloys and their effects on creep properties at elevated temperatures, Acta Mater. 50 (2002) 1095–1112.

[166] G. Lvov, V. Levit, M. Kaufman, Mechanism of primary MC carbide decomposition in Ni-base superalloys, Metall. Mater. Trans. A 35 (2004) 1669–1679.

[167] G. Bouse, Eta(η) and platelet phases in investment cast superalloys, Superalloys 1996 (1996) 163–172.

[168] B. G. Choi, I. S. Kim, D. H. Kim, C. Y. Jo, Temperature dependence of MC decomposition behavior in Ni-base superalloy GTD 111, Mater. Sci. Eng. A 478 (2008) 329–335.

[169] S. Seo, I. Kim, J. Lee, C. Jo, H. Miyahara, K. Ogi, Eta phase and boride formation in directionally solidified ni-base superalloy in792+ hf, Metall. Mater. Trans. A 38 (2007) 883–893.

[170] J. P. Shingledecker, G. M. Pharr, The role of eta phase formation on the creep strength and ductility of INCONEL alloy 740 at 1023 K (750 °C), Metall. Mater. Trans. A 43 (2012) 1902–1910.

[171] C. T. Sims, N. S. Stoloff, W. C. Hagel, Superalloys II (1987).

[172] L. Remy, J. Laniesse, H. Aubert, Precipitation behaviour and creep rupture of 706 type alloys, Mater. Sci. Eng. 38 (1979) 227–239.

[173] C. Cui, Y. Gu, D. Ping, H. Harada, T. Fukuda, The evolution of η phase in Ni–Co base superalloys, Mater. Sci. Eng. A 485 (2008) 651–656.

[174] L. Mataveli Suave, J. Cormier, P. Villechaise, D. Bertheau, G. Benoit, G. Cailletaud, L. Marcin, Anisotropy in creep properties of DS200 + Hf alloy, Mater. High Temp. (2016) 1–11.

[175] A. Yeh, C. Rae, S. Tin, High temperature creep of Ru-bearing Ni-base single crystal superalloys, Superalloys 2004 (2004) 677–686.

[176] S. Walston, A. Cetel, R. MacKay, K. OHara, D. Duhl, R. Dreshfield, Joint development of a fourth generation single crystal superalloy (2004).

[177] A. Ofori, C. Humphreys, S. Tin, C. Jones, A TEM study of the effect of platinum group metals in advanced single crystal nickel-base superalloys, in: Proc. 10th Symposium on Superalloys, TMS, Warrendale, PA, USA, Superalloys 2004, pp. 787–793.

[178] R. Drouard, J. Washburn, E. R. Parker, Recovery in single crystals of zinc, Trans. Metall. Soc. AIME (1953) 1226.

[179] O. Haase, E. Schmid, Über den gleitwiderstand von metallkristallen, Zeitschrift für Physik 33 (1925) 413–428.

[180] J. Michalak, H. Paxton, Some recovery characteristics of zone-melted iron, Trans. Metall. Soc. AIME 221 (1961) 850–857.

[181] A. Migliori, J. Sarrao, W. M. Visscher, T. Bell, M. Lei, Z. Fisk, R. Leisure, Resonant ultrasound spectroscopic techniques for measurement of the elastic moduli of solids, Phys. B Condens. Matter 183 (1993) 1–24.

[182] A. Migliori, J. Sarrao, Resonant Ultrasound Spectroscopy: Applications to Physics, Materials Measurements, and Nondestructive Evaluation, Wiley-Interscience, New York, 1997.

[183] R. G. Leisure, F. A. Willis, Resonant ultrasound spectroscopy, J. Phys. Condens. Matter 9 (1997) 6001–6029.

[184] P. Heyliger, A. Jilani, H. Ledbetter, R. G. Leisure, C.-L. Wang, Elastic constants of isotropic cylinders using resonant ultrasound, J. Acoust. Soc. Am. 94 (1993) 1482–1487.

[185] B. J. Zadler, J. H. L. Le Rousseau, J. A. Scales, M. L. Smith, Resonant ultrasound spectroscopy: theory and application, Geophys. J. Int. 156 (2004) 154–169.

[186] C. Zener, Contributions to the Theory of Beta-Phase Alloys, Phys. Rev. 71 (1947) 846–851.

[187] A. Bower, Applied Mechanics of Solids, CRC Press, Boca Ratton, 2010.

[188] D. Siebörger, H. Knake, U. Glatzel, Temperature dependence of the elastic moduli of the nickel-base superalloy CMSX-4 and its isolated phases, Mater. Sci. Eng. A 298 (2001) 26–33.

[189] J. D. N. Cheeke, Fundamentals and applications of ultrasonic waves, CRC press, 2012.

[190] Abaqus/CAE Version 6.12-1 User Manual, Dassault Systèmes Simulia Corp. Providence, RI., 2012.

[191] B. Goodlet, C. Torbet, L. Jauriqui, C. Aldrin, T. Pollock, Forward modeling of resonant ultrasound spectroscopy for nondestructive evaluation of mechanical damage, Acta Mater. (Submitted) (2016).

[192] B. Gairola, E. Kröner, A simple formula for calculating the bounds and the self-consistent value of the shear modulus of a polycrystalline aggregate of cubic crystals, Int. J. Eng. Sci. 19 (1981) 865–869.

[193] M. Nygårds, Number of grains necessary to homogenize elastic materials with cubic symmetry, Mech. Mater. 35 (2003) 1049–1057.

[194] A. Granato, K. Lücke, Theory of mechanical damping due to dislocations, J. Appl. Phys. 27 (1956) 583.

[195] A. De Kock, W. Crans, M. Druyvesteyn, Elastic anisotropy of polycrystalline copper wires as caused by different plastic deformations, Physica 31 (1965) 866–876.

[196] A. Granato, A. Hikata, K. Lücke, Recovery of damping and modulus changes following plastic deformation, Acta Metall. 6 (1958) 470–480.